Palacký University Olomouc
Faculty of Science
Joint Laboratory of Optics

MASTER'S THESIS

Simulations for a neutrino detector prototype Water Cherenkov Test Experiment

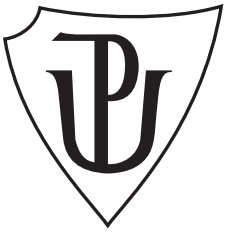


Author:	**František Hrubý**
Study programme:	N0533A110002 Applied Physics
Field of study:	Applied Physics
Study form:	Full time
Supervisor:	Mgr. Jiří Kvita, Ph.D.
Submission date:	August 2025

Univerzita Palackého v Olomouci
Přírodovědecká fakulta
Společná Laboratoř Optiky

DIPLOMOVÁ PRÁCE

Simulace pro neutrinový experiment Water Cherenkov Test Experiment



Vypracoval: :	**František Hrubý**
Studijní program:	N0533A110002 Aplikovaná Fyzika
Studijní obor:	Aplikovaná fyzika
Forma studia:	Prezenční
Vedoucí diplomové práce:	Mgr. Jiří Kvita, Ph.D.
Termín odevzdání práce:	Srpen 2025

Bibliographical identification

Autor's first name and surname	František Hrubý
Title	Simulations for a neutrino detector prototype Water Cherenkov Test Experiment
Type of thesis	Master
Department	Joint Laboratory of Optics
Supervisor	Mgr. Jiří Kvita, Ph.D.
The year of presentation	2025
Abstract	The Water Cherenkov Test Experiment is a prototype neutrino detector testing technologies and algorithms for the upcoming Hyper-Kamiokande neutrino experiments and its near Intermediate Water Cherenkov Detector. By measuring the Cherenkov rings of ionizing particles, it will enable the training of reconstruction models to increase the accuracy of neutrino measurements. This work contributes to this experiment in the areas of simulation, analysis, and detector assembly, specifically work on commissioning the detector, simulating various time-of-flight detector designs using custom simulated models, and simulating cosmic muons in water Cherenkov detectors using the official simulation tool WCSim, and analysis of data measured in 2025 by the time-of-flight detector in order to approximate the position of particles entering the detector. These contributions supported the objectives of the experiment.
Keywords	neutrino experiments; Cherenkov radiation; simulations; data analysis.
Number of pages	91
Number of appendices	0
Language	English

Bibliografická identifikace

Jméno a příjmení autora	František Hrubý
Název práce	Simulace pro neutrinový experiment Water Cherenkov Test Experiment
Typ práce	Diplomová
Pracoviště	Společná laboratoř optiky
Vedoucí práce	Mgr. Jiří Kvita, Ph.D.
Rok obhajoby práce	2025
Abstrakt	Water Cherenkov Test Experiment je prototyp neutrinového detektoru testující technologie a algoritmy pro nadcházející neutrinové experimenty Hyper-Kamiokande a jeho blízký detektor Intermediate Water Cherenkov Detector. Měřením Čerenkovských kroužků ionizujících částic umožní trénovat rekonstrukční modely pro zvýšení přesnosti identifikace neutrin. Tato práce obsahuje přínos k tomuto experimentu v oblasti simulací, analýzy a sestavování detektoru, konkrétně práci na uvedení detektoru do provozu, simulací různých návrhů time-of-flight detektoru pomocí vlastních simulačních modelů, simulací kosmických mionů ve vodních Čerenkovských detektorech pomocí oficiálního simulačního nástroje WCSim a analýzy dat změřených v roce 2025 time-of-flight detektorem za účelem rekonstrukce pozice částic vstupujících do detektoru. Tyto příspěvky podpořily cíle experimentu.
Klíčová slova	neutrinové experimenty; Čerenkovské záření; simulace; analýza dat.
Počet stran	91
Počet příloh	0
Jazyk	anglický

Declaration

I hereby declare that I have written this thesis independently under the supervision of Mgr. Jiří Kvita, Ph.D., and that I have used the sources that I cite and list in the bibliography. Large language models were used to check grammar and text flow.

In Olomouc, August 8, 2025

.....

František Hrubý

Prohlášení

Prohlašuji, že jsem předloženou diplomovou práci vypracoval samostatně pod vedením Mgr. Jiřího Kvity, Ph.D. a že jsem použil zdrojů, které cituji a uvádím v seznamu použitých pramenů. Bylo využito velkých jazykových modelů pro kontrolu gramatiky a toku textu.

V Olomouci dne 8. srpna 2025

.....

František Hrubý

Acknowledgement

I would like to express my sincere gratitude to my supervisor Mgr. Jiří Kvita, Ph.D. for his leadership, suggestions and frequent consultations, without which this thesis would not be possible.

I am also grateful to Prof. Akira Konaka for deep discussions and many suggestions concerning the analysis of the time-of-flight detector, and his feedback to my work when presenting the interim results during collaboration meetings.

Many thanks also belong to Bruno Ferrazzi and Arturo Fiorentini for teaching me about the experiment's detectors and instrumentation during the February 2025 experiment commissioning, and assistance with coding. I also thank other members of the WCTE collaboration, without which the experiment would not be successful.

CERN provided the experiment area, particle source and many resources to the experiment, which is the main topic of this thesis.

I am grateful to the projects IGA_PrF_2025_004 of Palacký University, and the MŠMT OP JAK FORTE reg. č. CZ.02.01.01/00/22_008/0004632 for supporting my work.

Contents

Introduction **10**

1 Neutrinos in the Standard model **11**
1.1 The Standard Model of particle physics 11
1.2 Neutrinos in the Standard Model and search for Beyond Standard Model physics 13
1.3 Interactions of neutrinos with matter 14

2 About the Water Cherenkov Test Experiment **19**
2.1 Goals of the WCTE experiment 19
2.2 WCTE detector design 19
2.2.1 Beam monitor setup 20
2.2.2 Main detector 24
2.2.3 PID in the main detector 24
2.2.4 Detector calibration 26
2.2.5 Water system 26
2.3 WCTE physics plan 28
2.3.1 Ultra pure water phase 28
2.3.2 Gadolinium enriched water phase 29

3 Assembly of the WCTE experiment **30**
3.1 Autumn 2024 assembly 30
3.1.1 mPMT modules preparation 30
3.1.2 Water system construction 30
3.2 February 2025 assembly 31
3.2.1 Beam monitors assembly 31
3.2.2 Detector and readout testing 32
3.2.3 Segmented time of flight detector testing via cosmic rays 33
3.2.4 WCTE shifts 37

4 Simulations for the WCTE experiment **38**
4.1 Time of flight detector simulation and particle position reconstruction . 38
4.1.1 Method of simulating the detector response 38
4.1.2 Round scintillator tile TOF detector simulation and position reconstruction 40
4.1.3 Squared tile detector design 49
4.1.4 Segmented time of flight detector design 52
4.2 Simulation of cosmic rays inside the main detector using the official WCSim simulation package 57

4.2.1 About the WCSim simulation package, cosmic ray simulation (and data structure) 57
4.2.2 Sea level cosmic muon models 61
4.2.3 Sea level cosmic muon fluxes and energies 63
4.2.4 Analysis of the cosmic muon simulated data from WCSim . . . 64

5 Analysis of the WCTE experiment 2025 data **73**
5.1 Particle position reconstruction using the time data from 2025 run . . . 73

Conclusion **87**

References **88**

Introduction

Neutrino physics constitute a significant part of planned experiments that aim to explore new frontiers of physics. All results that were acquired by neutrino measurements so far point to the Standard model not being complete. Thanks to the contributions of the Super-Kamiokande [1] experiment and Sudbury Neutrino Observatory [2], it is now widely known that neutrinos have a small but non-zero rest mass, as indicated by the neutrino oscillations. While these measurements were a success, more pieces of the neutrino puzzle are still missing, such as measuring the exact value of CP violation in the neutrino sector, that might explain part of the matter-antimatter antisymmetry, the mixing of neutrino mass eigenstates and the mass hierarchies, and measuring the neutrino rest mass. Further discoveries require new experiments with greater precisions, like the planned Hyper-Kamiokande [3] and DUNE [4] experiments, which plan to solve these mysteries.

As upcoming experiments will use not only modern detector technologies, but also analysis algorithms, such as the rapidly developing machine learning, there is a high demand for testing those novel methods. The Water Cherenkov Test Experiment (WCTE) is one such proving ground. Closely connected to the Hyper-Kamiokande experiment, it plans to test detectors and particle reconstruction algorithms that will be used in both its far detector, and the near detector called the Intermediate Water Cherenkov Detector (IWCD).

This thesis presents some of the work that was done on the WCTE experiment. First, it documents the assembly and commissioning of the experiment, including work on the detector water system, detector testing and installation and data taking shifts. Second, it covers simulations of the experiment, where a custom toy model of the time-of-flight detector was used to approximate the signal response, and a contribution to the official simulation package for water Cherenkov detectors WCSim on the topic of cosmic muon simulations was made. Lastly, it includes analysis of the data collected by the experiment, with a focus on the particle position reconstruction in the time-of-flight detector. This analysis directly contributes to calibration measurements of the detector and therefore helps to further validate the reconstruction technologies that will be used in future neutrino experiments.

Chapter 1

Neutrinos in the Standard model

The final purpose of the WCTE experiment is related to upcoming neutrino experiments, and as such it is deeply connected to the Standard Model of particle physics as well as to the search for physics beyond it. Many experiments have already measured neutrino interactions, and their results indicate that the Standard Model is incomplete [5, 6]. There are still many problems that remain unexplained, like the problem of neutrino mass hierarchy, and measuring the CP symmetry breaking of neutrino/antineutrino interactions [7]. As such, this experiment plays an important role in making further advances in the field of neutrino physics.

1.1 The Standard Model of particle physics

The Standard Model of particle physics is as of now the most successful model of particle physics and explains the behavior of particles on subatomic level. In this model, nucleons are further divided into smaller particles, called quarks [8]. The quarks are held together inside nucleons by the strong interaction. These bonds that hold the nucleon together contain most of the mass of the nucleus [9].

In addition to quarks, the Standard Model includes leptons - point like particles that interact either by electromagnetic or weak interaction, but not the strong force. The most famous member of this group is the electron, which is the only stable charged lepton [6]. Other than the electron, there is also the muon and the tau lepton, which are unstable particles that decay into lighter leptons. Besides producing charged leptons during such decays also produce neutral leptons. These leptons are called neutrinos. There are three types of neutrinos, which correspond to each of the leptons. There is the electron neutrino, the muon neutrino and the tau neutrino [8].

There are three groups or "families" in the Standard Model. The quarks are also sorted into these families, where in the first family there are the up and down quarks. These are the most prevalent quarks in nature, as they constitute all protons and neutrons. Interesting thing about quarks is that they have a fractional charge, i.e. they have either charge $2/3$ of e or $-1/3$ of e. By sorting them via the charge value, quarks of type "up" and quarks of type "down" are distinguished [8].

Other than the up and down quark, there also exist other, more exotic quarks, that are distinguished by their respective quantum numbers. In the second quark family, there is the strange quark, that has a quantum number called strangeness $S = 1$, and the charm quark, with the charm quantum number $C = 1$. Discovering these quarks explained some rare particle decays, and why some decays were suppressed compared to others [8].

The last quark family is made up of super heavy quarks. The bottom (beauty) quark is a quark with the negative fractional charge and the beauty (or bottomness) quantum number $B = 1$. The top quark has the positive fractional charge, topness (or truth) quantum number $T = 1$ and is so heavy and unstable, that it decays almost immediately into either bottom quark or into bosons [8].

Antiparticles, which are counterparts to classic particles with opposite quantum numbers, such as charge, lepton numbers, baryon numbers and so on, are also a part of the standard model [8]. The first antiparticle discovered was the antielectron, also called positron, which was predicted by Dirac and confirmed from measurements of cosmic rays [10, 11]. Since then, all other elementary antiparticles corresponding to their respective particles were discovered [6].

The Standard Model also describes field interactions, i.e. the electromagnetic force, the weak force and the strong force. These forces are intermediated by particles called bosons. Each interaction has its own bosons. For example, the electromagnetic interaction happens through a photon. The weak interaction has three bosons: a positive W^+ boson, a negative W^- boson, and a neutral Z^0 boson. Lastly, the strong interaction is mediated by eight gluons [8]. Gravity is the last interaction, and its theoretical boson is called a graviton, but this particle has not been yet observed, and its description will need a unification of the theory of general relativity with the Standard Model [12].

An overview of the Standard Model – including the three generations of quarks and leptons, together with the gauge bosons – is summarized in Figure 1.1.

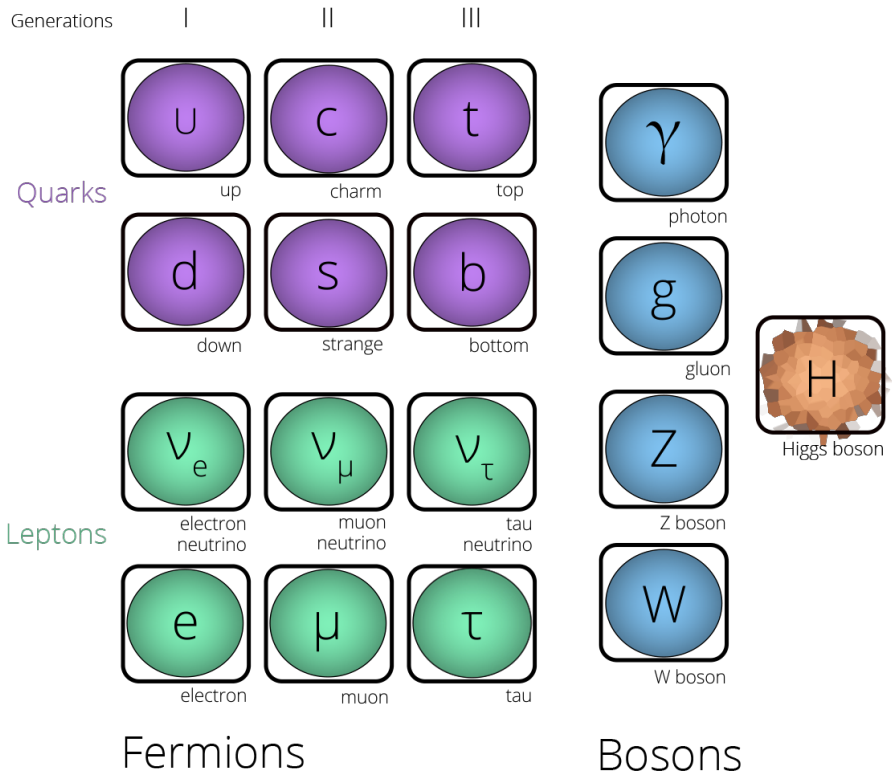


Figure 1.1: A diagram illustrating the fundamental particles of the Standard Model of particle physics, including the elementary fermions that make up baryons and mesons, as well as the gauge bosons responsible for mediating the three of the four basic interactions. Taken from [13].

The confirmation that there are indeed only three generations in the Standard Model has been brought by researching the decay of the Z boson. As a weak interaction boson, it can decay into a neutrino and antineutrino pair. It turns out that the neutrino decay width is strongly correlated to the hadron production cross section. The theoretical curves for different number of neutrino generations have been compared to experimental data of hadrons production in Z decays. The result of this comparison was that the experimental data fit best to the curve corresponding to 3 light neutrino generations [6, 14]. This can be seen in Figure 1.2.

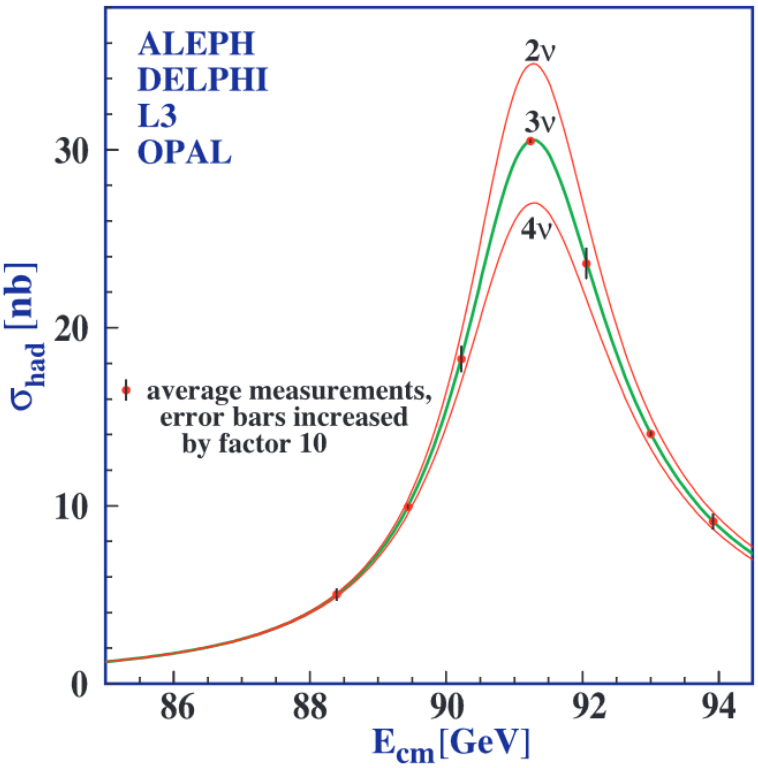


Figure 1.2: Hadron production cross section in e^+e^- annihilation, which corresponds to the Z boson rest mass. The curves show predictions for two, three and four quark families, corresponding to Z boson decay to two, three or four light neutrinos, respectively. The combined data from DELPH [15], ALEPH [16], L3 [17] and OPAL [18] experiments confirm that the best fit corresponds to three lepton and quark families. Taken from [6].

1.2 Neutrinos in the Standard Model and search for Beyond Standard Model physics

One of the few limitations of the Standard Model is that it predicts no rest mass for neutrinos. That goes against experimental measurements which confirm that neutrinos have very small but non-zero rest masses. The main evidence is that neutrinos undergo a process called oscillation when traveling through space [5, 6]. This can only occur if the neutrinos have a rest mass. The reason for that is because each flavor state is in reality a quantum superposition of 3 distinct mass eigenstates, which propagate

across space at different momenta [6]. This results in the oscillation of the probability of observing a certain neutrino flavor at different points in space.

The relation between the flavor and mass states of neutrinos can be described by three mixing angles and differences between the three neutrino mass states. The equation describing the mixing of mass eigenstates is the so called PMNS matrix and has the following form [6, 19, 20]:

$$\begin{pmatrix} \nu_e \\ \nu_\mu \\ \nu_\tau \end{pmatrix} = \begin{pmatrix} c_{12}c_{13} & s_{12}c_{13} & s_{13}e^{-i\delta} \\ -s_{12}c_{23} - c_{12}s_{23}s_{13}e^{i\delta} & c_{12}c_{23} - s_{12}s_{23}s_{13}e^{i\delta} & s_{23}c_{13} \\ s_{12}s_{23} - c_{12}c_{23}s_{13}e^{i\delta} & -c_{12}s_{23} - s_{12}c_{23}s_{13}e^{i\delta} & c_{23}c_{13} \end{pmatrix} \cdot \begin{pmatrix} e^{i\alpha_1} & 0 & 0 \\ 0 & e^{i\alpha_2} & 0 \\ 0 & 0 & 1 \end{pmatrix} \cdot \begin{pmatrix} \nu_1 \\ \nu_2 \\ \nu_3 \end{pmatrix} . \quad (1.1)$$

In this equation, c_{ij} and s_{ij} are the cosine and sine of the corresponding mixing angles θ_{ij}, i.e. θ_{12}, θ_{23}, θ_{13}, and δ is the CP violating phase [20, 21]. There are also phases α_1 and α_2 which are so called Majorana phases which do not enter oscillation probabilities and therefore are only important for some Majorana processes [20]. On the other hand, the CP violating phase, or as it is sometimes called, Dirac phase, is very important for the neutrino mixing, since it is the essence of the differences between oscillations of neutrinos and antineutrinos [20].

From measurements of Solar neutrinos which start as electron neutrinos from nuclear processes inside the Sun, and atmospheric neutrinos, which are mostly muon neutrinos from pion and kaon decays, the differences between their respective oscillations was measured [6, 7]. A convention was adopted, that solar neutrinos mixing angles and mass differences correspond to [22]

$$\theta_{sol} = \theta_{12} \ , \quad (1.2)$$

$$\Delta m^2_{sol} = \Delta m^2_{12} \ , \quad (1.3)$$

which are the mixing angle and squared mass difference between the first and second mass states. The oscillation of atmospheric neutrinos then must correspond to either mixing of ν_1 and ν_3 or ν_2 and ν_3. When it is considered, that the measurements of $\Delta m^2_{sol} \ll \Delta m^2_{atm} \simeq \Delta m^2_{13} \simeq \Delta m^2_{23}$, the masses can be ordered into two possible hierarchies.

The first possible hierarchy is called the normal hierarchy, in which the masses of the neutrino mass states are $m_1 < m_2 < m_3$. The opposite is true for the second, inverted hierarchy, where $m_3 < m_1 < m_2$ [6]. The visualization of both hierarchies can be seen in Figure 1.3. To determine whether the normal or inverted hierarchy is realized in nature, a measurement of the sign of the last mass difference Δm^2_{13}, or equivalently Δm^2_{23}, needs to be done, with a positive sign corresponding to the normal hierarchy and a negative sign to the inverted one. The absolute value has already been measured, as were the mixing angles. This is one of the main purposes of many ongoing or upcoming neutrino experiments, like DUNE [4], Super-Kamiokande [1] and T2K [23], Hyper-Kamiokande [3] and others.

1.3 Interactions of neutrinos with matter

According to the Standard Model, neutrinos are particles that interact only through the weak interaction and gravity [6]. Because of that, their interactions have very small

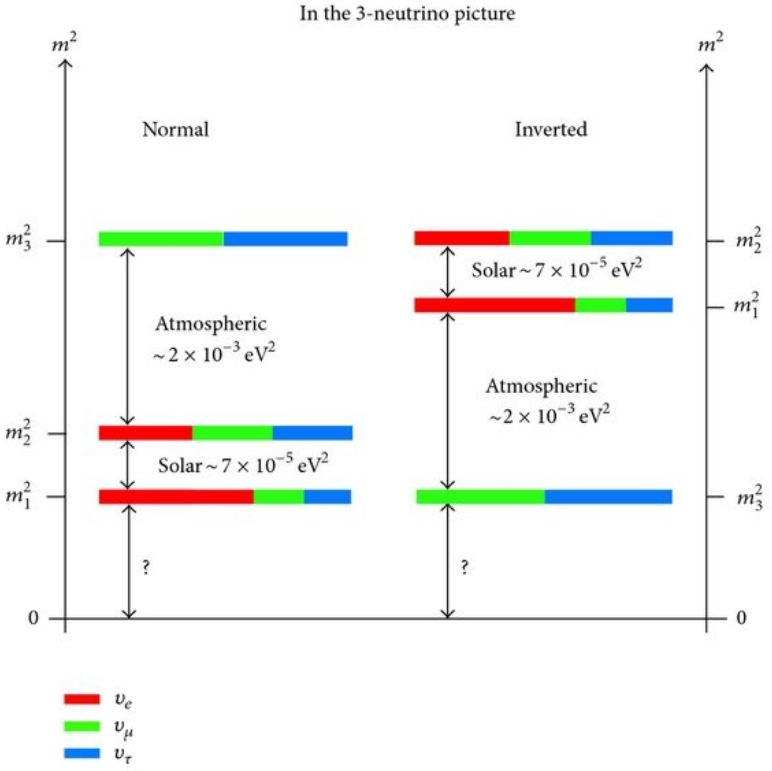


Figure 1.3: A depiction of mass hierarchies of neutrino mass states. Taken from [22].

cross sections, needing large detector volumes for their detection [24]. It is not possible to detect them directly, their detection is only possible by detecting secondary particles created when they go through a weak interaction, either with a lepton or an atomic nucleus.

At low energies (below 100 MeV), the main detection channel is using the inverse beta decay process and neutrino capture process. The inverse beta decay is the main way to detect antineutrinos, also sometimes called antineutrino-proton scattering, as the antineutrino interacts with a proton, creating a positron and a neutron in the process [25, 26]:

$$\overline{\nu}_\ell + p \rightarrow e^+ + n \ . \tag{1.4}$$

As a positron and neutron are the final states of this interaction, detection of this process requires either a magnetic field for distinction of positrons from electrons, the detector needs to be capable of measuring $e^- + e^+ \rightarrow \gamma + \gamma$ annihilation, or a way to detect neutrons has to be added to the detector, as has been done in the Super-Kamiokande experiment to detect the diffuse supernova neutrino background (DSNB) [27].

The neutrino capture process occurs on heavy, usually radioactive nuclei, and it is therefore sometimes called stimulated or enhanced beta decay [26]. it is similar to the traditional β^- decay, but instead of being the decay product, it enters the reaction

$$\nu_\ell + N(Z,A) \rightarrow e^- + N(Z+1,A) \ , \tag{1.5}$$

where it changes a neutron into a proton inside a nucleus, emitting an electron in the process.

At intermediate energies from 0.1 to 20 GeV, the main methods of detection are through elastic and quasi-elastic scattering, inelastic scattering, or a resonance production [26]. The total cross section of neutrino interactions is displayed in Figure 1.4 as function of neutrino energy.

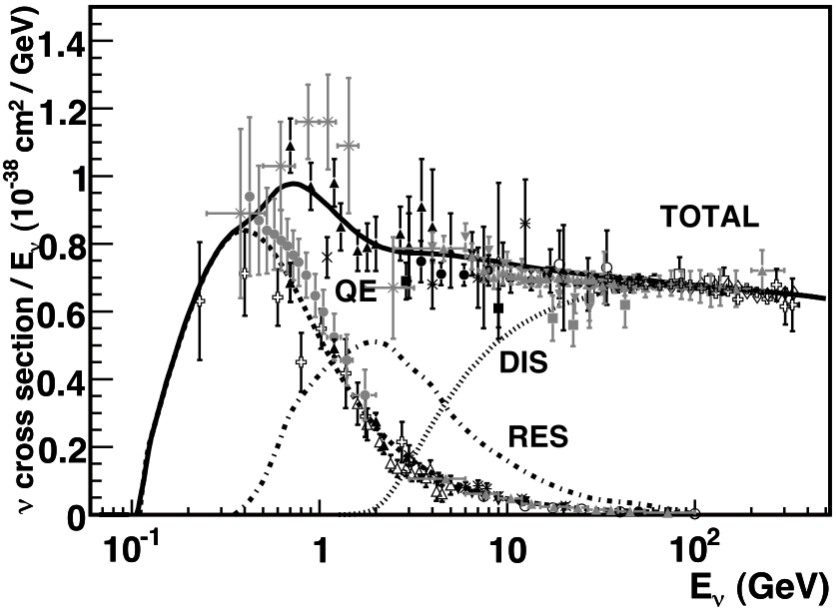


Figure 1.4: The total cross section of neutrino interactions in the 0.1 GeV to 20 GeV region, including the separate processes - quasielastic scattering, resonance pion production and deep inelastic scattering. Points correspond to measured data, lines are the theoretical predictions of the interaction cross sections provided by the NUANCE generator [28]. Taken from [26].

The main interaction below 1 GeV of the neutrino kinetic energy, that is used to detect neutrinos, is quasi-elastic scattering on an atomic nucleus. Quasi-elastic (QE) scattering is a charged current interaction, during which neutrino or antineutrino exchanges a W boson with a nucleon, turning itself into its corresponding lepton. As the QE scattering is always a charged current interaction, it is sometimes shortened to CCQE interaction in literature. The interaction is as follows [29]:

$$\nu_\ell + n \to \ell^- + p \ , \qquad \overline{\nu}_\ell + p \to \ell^+ + n \ . \tag{1.6}$$

The cross section of this interaction around the 1 GeV range is on the order of 10^{-38} cm^2 = 100 pb [26]. The Feynman diagram for this type of interaction is shown in Figure 1.5.

The pion production in neutrino processes becomes significant above 1 GeV of the neutrino energy and is possible mainly through two interactions [30]. The first interaction is called resonant pion production, with the majority of pion production coming from it. During it, a resonant state is created [26, 30]

$$\nu_\ell + N \to \ell^- + N^* \to \ell^- + N' + \pi^0 \ , \tag{1.7}$$

where N^* is an excited nucleus, which decays via a strong interaction, producing a meson. While a majority of pions are created via this process, it also is the background

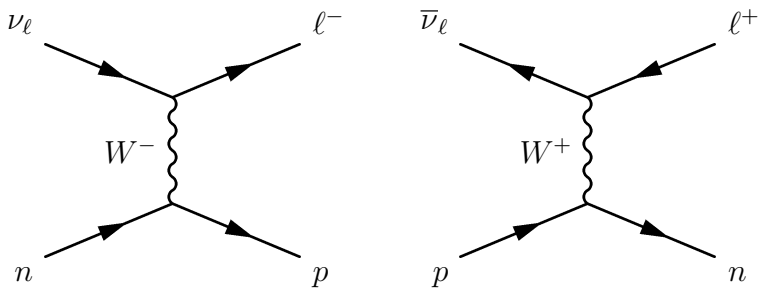


Figure 1.5: Feynman diagram of neutrino quasi-elastic scattering on an atomic nucleus.

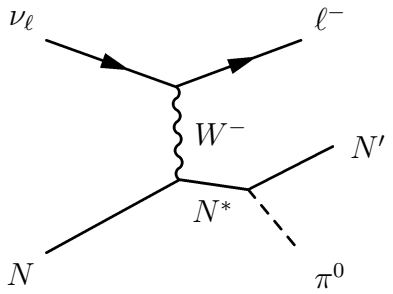


Figure 1.6: Feynman diagram of resonant pion production from neutrinos on nucleus.

process to the CCQE interactions, since a lepton is produced [31]. The diagram of this interaction is shown in Figure 1.6.

Besides resonant pion production, another process of pion production exists called coherent scattering. As opposed to the resonant production, the coherent scattering occurs, when a neutrino interacts with a whole atomic nucleus (a different process from incoherent scattering, where a particle interacts with just one of the constituents of the nucleus - like a proton or neutron), transferring a negligible amount of energy to it and creating a pion final state. These interactions are made up of both charged current and neutral current interactions. As opposed to charged current interactions, where the final state is a lepton corresponding to the interaction neutrino and thus is mediated by a W boson, neutral current (NC) interactions produces a neutrino final state, and therefore the interaction is mediated by a Z^0 boson. Coherent scattering has lower cross sections when compared to resonant production or CCQE scattering, but typically produces a very forward-scattered pion [26, 30, 32]. The interactions are

$$\nu_\ell + A \to \nu_\ell + A + \pi^0 \ , \qquad \overline{\nu}_l + A \to \overline{\nu}_l + A + \pi^0 \ , \tag{1.8}$$

$$\nu_\ell + A \to \ell^- + A + \pi^+ \ , \qquad \overline{\nu}_l + A \to \ell^+ + A + \pi^- \ . \tag{1.9}$$

Other than quasi-elastic scattering, an elastic scattering interaction is also possible. Elastic scattering is a NC interaction, in which a neutrino forwards its energy to a proton or neutron. The resulting nucleon energy in the final state is usually around 100 MeV, but it can produce up to 300 MeV protons and neutrons [33]. This process can be written as following:

$$\nu_\ell(k) + N(p) \to \nu_\ell(k') + N(p') \ . \tag{1.10}$$

Another possible particle that has a non-zero chance of production in neutrino

interactions is a kaon. These can be produced at energies higher than 0.78 GeV [34], but have very low production probability.

At energies higher than 1 GeV, neutrinos can interact through deep inelastic scattering, with both NC and CC current channels available and the final products being a lepton and a hadronic shower [26, 35]:

$$\nu_\ell + N \to \ell^- + X \ , \qquad \nu_\ell + N \to \nu_\ell + X \ , \tag{1.11}$$

$$\overline{\nu}_\ell + N \to \ell^+ + X \ , \qquad \overline{\nu}_\ell + N \to \overline{\nu}_\ell + X \ . \tag{1.12}$$

All together, neutrinos can produce a variety of leptons (electrons, muons and even tau leptons) by quasi-elastic scattering, protons and neutrons from elastic scattering, pions via resonant production and coherent scattering, with kaon production being also possible, and hadronic showers at high enough energies. Due to that, the WCTE experiment measures these particles and their cross sections in water, so that the results can be used in other upcoming neutrino experiments, many of which plan to explore new physics beyond the Standard Model.

Chapter 2

About the Water Cherenkov Test Experiment

The Water Cherenkov Test Experiment (WCTE) is an ongoing project that has completed its data taking phase at CERN [36–38]. The purpose of this experiment is to measure cross sections of interactions of low momentum ionizing particles with water, namely of electrons, muons, pions, protons, photons and neutrons [39]. It also serves to test detector technologies that will be used in the upcoming Hyper Kamiokande (HyperK) experiment and its near detector Intermediate Water Cherenkov Detector (IWCD), that are being built and will start data taking in the beginning of year 2028 [40, 41]. Another goal of WCTE is to test particle reconstruction algorithms, mainly algorithm fitQun and machine learning, ones that will also be used in future water Cherenkov experiments [42, 43].

2.1 Goals of the WCTE experiment

The upcoming HyperK and IWCD detectors will be constructed along the neutrino beamline of the J-PARC accelerator in Tokai, Japan, and will produce a neutrino beam at energies peaking around 600 MeV [3]. These neutrinos will then interact in a volume of water, producing $e^{\pm}$, $\mu^{\pm}$, p^{+} and $\pi^{\pm,0}$, with some $K^{\pm}$ production also being possible at higher energies [26]. For that reason, the WCTE experiment is measuring these particles at energies ranging from 200 MeV to 1100 MeV [38].

The experiment was located on the T9 beamline of PS at CERN, which produces the necessary particles from proton collisions with a target [36]. The detector has several parts, that will be described in more detail in Section 2.2. As of writing this thesis, the experiment has finished data taking and has been decommissioned. Now, it is moving into the analysis phase, with the disassembled detectors being moved to Japan for the HyperK and IWCD assembly, to their respective institutions to be repaired or used in other measurements, or they were donated to CERN [37].

2.2 WCTE detector design

The WCTE experiment consists of two parts. The first is used for particle identification, and consists of scintillator detectors and aerogel Cherenkov threshold counters that monitor the secondary beam composition. The second part is called the main detector, a steel tank with a height of 4 meters and 4 meters in diameter with photomultipliers

attached to an inside construction, which detect the Cherenkov light produced by charged particles in water [36, 38].

2.2.1 Beam monitor setup

The WCTE experiment went through several test runs in years 2022 and 2023 for the beam monitors, and the whole experiment setup had its first complete run in year 2024. Throughout the years, the beam monitor part of the experiment underwent several iterations.

The beam monitors are composed of several detectors set on the beamline, assembled in such a way as to enable particle identification, to be able to veto the particles that diverge from the nominal beam direction, and a dipole magnet used for filtering out all of the charged particles from the beamline, which is useful for studying neutral particles like γ photons [37]. Because any background light creates a lot of noise when it gets into the detectors, all of them need to be lightproof, which is done by enclosing the photo-sensitive parts inside a black box, and carefully taping up any problematic areas in a black tape. It is also very important not to put any more material than necessary into the beamline, since the particles will then lose energy, or can even scintillate and interact, which would complicate the analysis and particle identification (PID).

The final setup of the beam monitors used in the 2025 run is depicted in Figure 2.1. It has several different types of detectors. The first detector types are so-called "trigger" detectors, marked as T0, T1, T2, T3 and T4 in the experiment sketch. These detectors are each made of a scintillator tile, surrounded by several photomultipliers (PMTs). When a particle goes through the scintillator, it generates a flash of light. The photons are then detected by the PMTs, converting to a voltage signal which is then read-out. The detectors are called trigger detectors, because when they detect any signal higher than a certain value, the whole detector setup records the event. For that reason, they need to function reliably for extended periods of time, and because the particle flux of the beamline is very high, especially on higher energies, they also need to be fast. Because of that, T0 and T1 both have 4 PMTs, T4 has only 2 larger PMTs. T2 and T3 are much smaller, and only have 1 PMT. The sketch of T0 and T1 is shown in Figure 2.2.

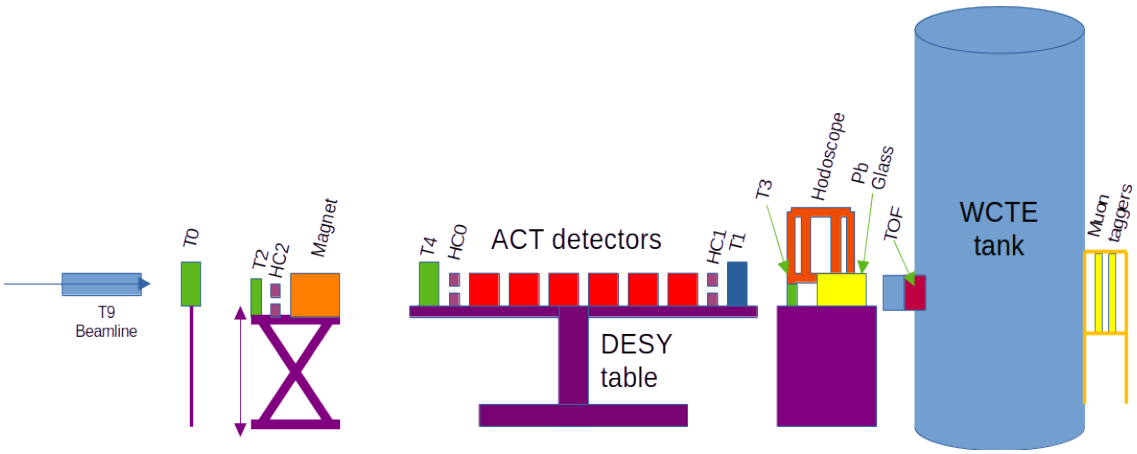


Figure 2.1: A sketch of the WCTE experiment setup used in year 2025.



Figure 2.2: A transverse sketch of trigger detectors T0 and T1.

Next detector type is the hole counter, denoted as HC in the schematic. The principle behind these detectors is the same as with the trigger detectors, being a scintillator board with a single PMT attached. The main difference is that these detectors have a hole in the middle. Thanks to that, particles that pass through the hole do not leave any signal in the detector, allowing the detection of only those events, that diverge too much from the nominal beam direction because of scattering on the other detectors. Consequently, during the analysis, these events are desirable to be excluded, which leads to a cleaner event selection. There are in total three hole counters, with two (HC-0 and HC-1) being larger than HC-2, which is only used in special runs. The schematic of this detector type is shown in Figure 2.3

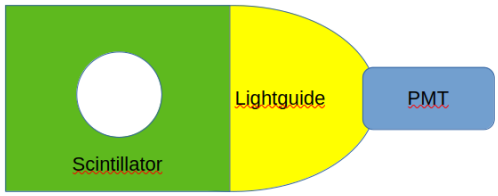


Figure 2.3: Schematic of the hole counter detectors.

One of the most important parts in the particle identification setup are the aerogel Cherenkov threshold counters, or ACT boxes. These detectors work on the principle of Cherenkov light production. Cherenkov light is light produced when a charged particle traverses a medium with a speed higher than the speed of light in that material [44]. The higher the speed of the particle, the higher is the radius of the resulting Cherenkov cone. The following relation holds:

$$\cos\theta = \frac{1}{n\beta} \ , \tag{2.1}$$

where θ is the angle between the direction of the produced photon and the direction of the primary particle, $\beta = v/c$ is the particle speed represented as a fraction of the speed of light, and n is the refractive index of the medium. From this relation, the threshold speed at which the Cherenkov light starts to be produced can be derived as

$$\beta_{thr} = \frac{1}{n} \ . \tag{2.2}$$

As a result, by choosing a suitable medium (with appropriate refraction index), only particles with higher or equal speed to the threshold speed can be detected. When this is combined with different particles having different mass, which results in slower

and faster particles at the same beam momentum, by choosing a suitable refraction index, only particles of certain mass or lower can be detected. Since electrons are very light (and very relativistic), they will almost always produce light in the Cherenkov detectors, but more massive particles, like muons or pions, will only start producing light at higher than threshold energies in the same detector.

To take advantage of that, a set of six different ACT boxes is used, sorted into two groups. The first group is set so that it only detects electrons, and as such they have a lower refractive index. The second group is designed to detect the rest of particles, i.e. they have higher n [37]. By comparing the signal in the two groups with other detectors and applying proper cuts, a choice can be done to select events of interest and identify particles, which is important for comparing and training particle reconstruction models in the main detector.

The detectors themselves are in essence relatively simple in construction. The main part of the detector is an aerogel [45] block, usually 4 to 6 cm thick. This serves as the active medium, in which the Cherenkov light is produced. Aerogel is a special material with very low refractive index. As it is mostly silicon gel filled with air bubbles, it is very light with low density, and since it is solid it does not need any special containment, like other gas Cherenkov threshold detectors need, which is advantageous for the purposes of this experiment. The aerogels used in the detectors range from refractive index 1.006 to 1.15, depending on what beam momenta are used. After the Cherenkov light passes through the aerogel, it is reflected to photomultipliers by a reflective foil. The design is shown in Figure 2.4.

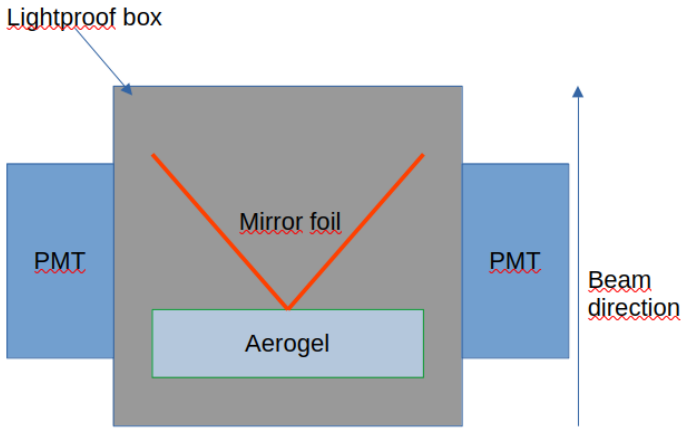


Figure 2.4: Sketch of a top-down view of the aerogel Cherenkov threshold counter.

Inside the inlet pipe of the main detector is the time-of-flight detector (TOF in the experiment schematics). The time-of-flight detector is a scintillation detector, but of a different design that the trigger and HC detectors. The scintillators used in this detector are 8 segmented scintillator blocks with different dimensions, arranged in a way as to fit inside the inlet pipe of the main detector [37]. On each end of a scintillator segment is a silicon photomultiplier (SiPM). The schematic of this detector in shown in Figure 2.5. This light detection technology has very fast detection, but longer relaxation time, so it is very useful for precise time measurements. This allows for a very accurate measurement of the time of flight of different particles by comparing the data with that from the other detectors, primarily the trigger detectors. By applying cuts on different times of flight, different particles to analyze can be chosen. Electrons

will be the fastest particles, then, muons and pions will be detected. Other particles like kaons, protons, deuterium and so on are much heavier and as such will arrive much later. Time of flight cuts can be applied very easily for lower energies. For higher energies, the muon, pion and electron time of flight peaks will merge and can be no longer differentiated by time of flight only, and need to be compared with data from other detectors like the ACTs in order to ensure efficient PID.

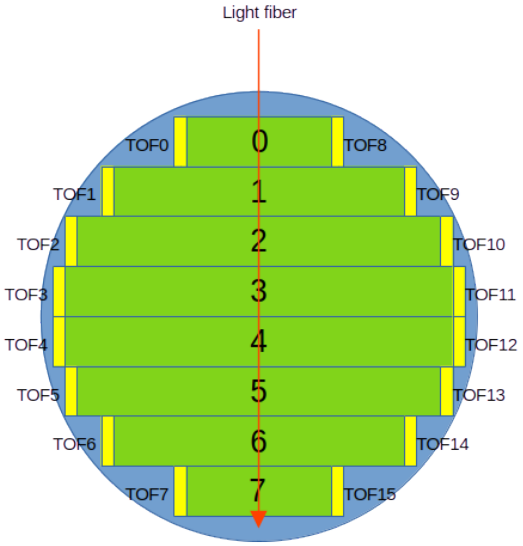


Figure 2.5: The final time of flight detector design. Numbers 0 through 7 show the eight scintillator segments. Each SiPM is tagged by its corresponding number ranging from 0 to 15. A light fiber is also fed into the detector for detector testing purposes.

Behind the main detector there are two muon tagger detectors (MUT). These are larger scintillation detectors very similar to the hole counters but without the cavity in the middle. As they are behind the steel walls of the main detector, which will stop most particles, the only particles which will reach reach the MUT detectors are muons, as they are minimum ionizing particles (MIPs). That allows them to pass without too much energy loss by ionization. As a result, the signal from these detectors can be used to choose purely muon events for analysis.

Adjacent to the beamline is the hodoscope. Hodoscope is an array of scintillator detectors used during special runs, during which a magnet (orange in the experiment setup schematics) is lowered into the beamline. This diverts all the charged particles out of the beamline, allowing only neutral particles to reach the main detector. From which hodoscope is hit by an electron, the energy of gamma photons, that interact inside the main detector, can be inferred.

The last detector in the beam monitoring setup is the lead glass calorimeter. The detector is set up on a rail system, which makes it possible to be put in or out of the beamline. This device is useful for testing measurements, checking energies of the particles on the beamline. As it is a calorimeter, the measurements are destructive, with electrons and photons leaving most of their energy inside, by creating an electromagnetic shower. As such, it stops these particles from entering the main detector entirely. Because of that, it is not used in main experiment runs. Muons can still pass through the detector, as they are minimum ionizing particles, but they are still measured by the Cherenkov light produced in the lead glass. Heavier hadrons also stop in this detector, producing Cherenkov light or a hadronic shower. The scintillation and

Cherenkov light produced in the calorimeter is then measured by a single PMT at the back of the detector.

2.2.2 Main detector

The main detector is a steel tank 4 meters in diameter and 4 meters in height, filled with ultra pure water. Inside the tank, there is a steel construction, that holds multi-PMT (mPMT) modules. A photo of the module can be seen in Figure 2.6. There are in total 97 mPMT modules, each containing 19 PMTs [40]. The mPMTs are divided between the detector's top end cap (TEC), the walls of the detector (also called barrel mPMTs) and the bottom end cap (BEC). Among the 97 mPMT modules there are four modules, that will be used in the far detector of Hyper-Kamiokande, the rest of the modules are of a different type that will be used in the IWCD detector, the near detector of the Hyper-K experiment. As the steel construction can reflect Cherenkov light, creating undesired noise and late detections, all the modules are surrounded by a blacksheet, that reduces this light pollution. On the TEC of the detector there is also a central delivery system (CDS). This system can be used to put detector calibration sources inside the main detector.



Figure 2.6: A photo of an mPMT module before installation inside the main detector taken during the detector assembly in August 2024.

2.2.3 PID in the main detector

The individual PMTs inside the mPMT modules detect the Cherenkov light produced by the particles from the beamline and any cosmic muons that enter the detector. As mentioned in section 1, the particles of most interest are electrons, muons, pions and photons, but also kaons and protons at higher energies. Charged particles produce

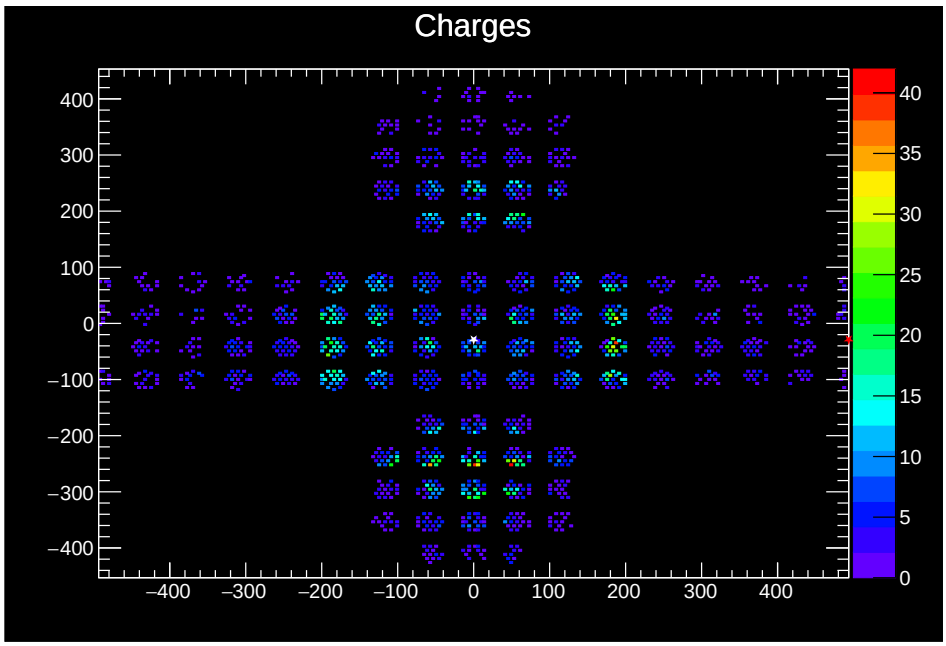


Figure 2.7: A water Cherenkov ring corresponding to an 800 MeV/c electron entering the barrel, as simulated by WCSim.

different Cherenkov light cones in water. The comparison of the hit PMTs with the data from the beam monitoring setup enables identifying which particle produced which Cherenkov cone, allowing primary particle reconstruction algorithms training on clean samples, and subsequent control of the results.

Electrons inside the detector usually produce only one Cherenkov light ring. This ring is blurred as a result of the electrons producing electromagnetic showers in water through bremsstrahlung, creating secondary electrons and gamma photons, which produce additional Cherenkov light cones. A diagram of what this might look like can be seen in Figure 2.7.

Signal from muons is much clearer than from electrons. That is because at the momentum that is used in the experiment, muons are approximately minimally ionizing particles. This means they do not produce electromagnetic showers, so no secondary particles which would blur the Cherenkov light ring are produced, resulting in a sharper ring. This can be seen in Figure 2.8. Muons are unstable particles with a decay time of [6]

$$\tau_\mu = (2.1969811 \pm 0.0000022) \times 10^{-6} \text{ s} . \tag{2.3}$$

If a muon decays inside the main water volume, it produces a so-called Michel electron, which then produces its own light cone. Because of that, some muon events can have more than one Cherenkov light cone produced, which also has to be taken into account during primary particle reconstruction for upcoming neutrino experiments.

Pion signals can be some of the hardest to recognize, as pions can interact hadronicaly with water molecules, usually creating a shower of secondary particles. Charged pion can also decay into a muon, which can create additional Cherenkov ring. If it does not interact at all, it behaves similarly to a muon, creating a single clear Cherenkov ring that is hard to differentiate from a muon one. Due to this, pion events can appear as single-ring events, or multi-ring events with a varying number of Cherenkov rings exhibiting different degrees of blurring. An example of a pion ring can be seen in Figure 2.9. Neutral pions are also a possible product of neutrino interactions. As these

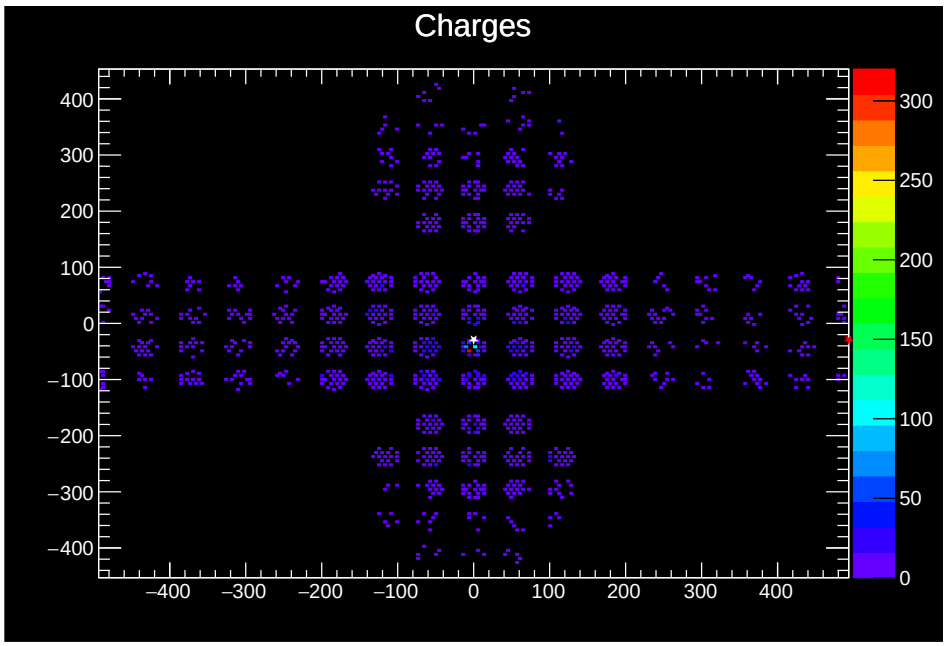


Figure 2.8: A water Cherenkov ring corresponding to a 800 MeV/c negative muon entering the barrel, as simulated by WCSim.

particles quickly decay into two γ photons, they create two blurry Cherenkov rings, where each is similar to an electron ring. This can be seen in Figure 2.10.

2.2.4 Detector calibration

For correct particle detection, the individual PMTs need to be calibrated. Calibration can be done in several ways. The first way to calibrate the PMTs is to use light emitting diodes (LEDs), which are implanted into individual mPMT modules. These LEDs can be flashed when needed, and enable us to study timing of the detectors, and light scattering and reflections inside the detector. Other calibrations of the detector are possible thanks to the central delivery system (CDS), which has been installed into the top end cap of the detector. This system allows for the insertion of different radiation sources inside the tank itself. There are several sources used for further calibration. The first is the diffuser ball, sometimes also called laser ball, which diffuses light from a pulsed laser to the PMTs and so allows us to measure relative efficiency and relative timing between the photosensors. Next calibration source is a radioactive nickel-californium (NiCf) source which produces 9 MeV γ photons, and is used in studying single photo-electron detector response. There is also the americium-beryllium source (AmBe) used for neutron detection studies. Part of the calibration system are also eight photogrammetry cameras used to see inside the detector [36].

2.2.5 Water system

As any impurities in the water influence the detection capabilities of the mPMTs, there is a need to ensure that the water stays very pure, without too much of metal ions or bacteria. For that purpose there exists a whole water filtering and monitoring system. The water system pumps the water out of the detector, while replacing it with filtered water. The pumped out water is pushed into a water filtering setup where, through a series of filters and a UV lamp, the water is purified and is put back to the detector.

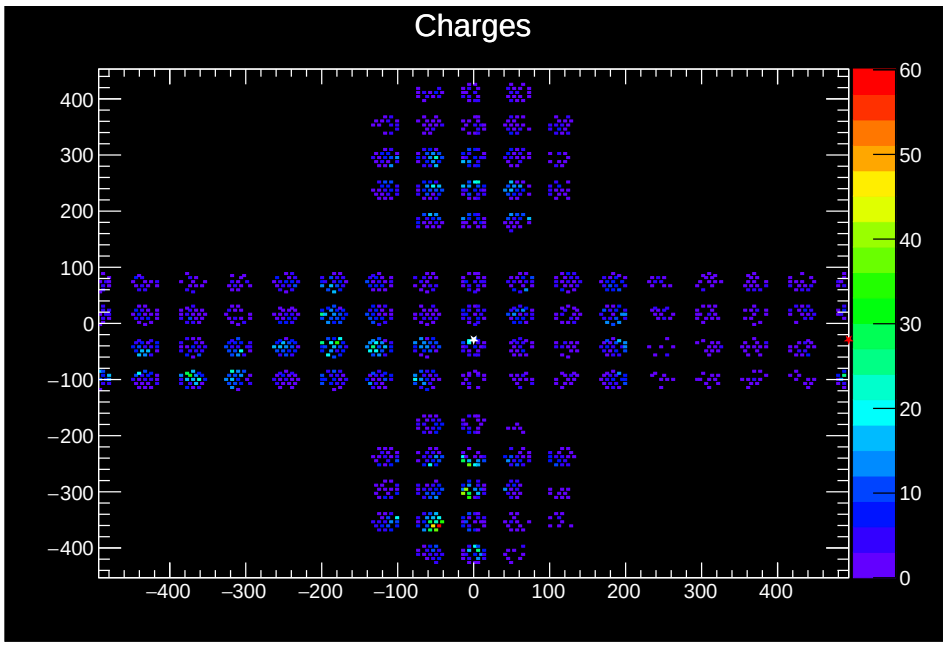


Figure 2.9: A water Cherenkov ring corresponding to a 800 MeV/c negative pion entering the barrel, as simulated by WCSim.

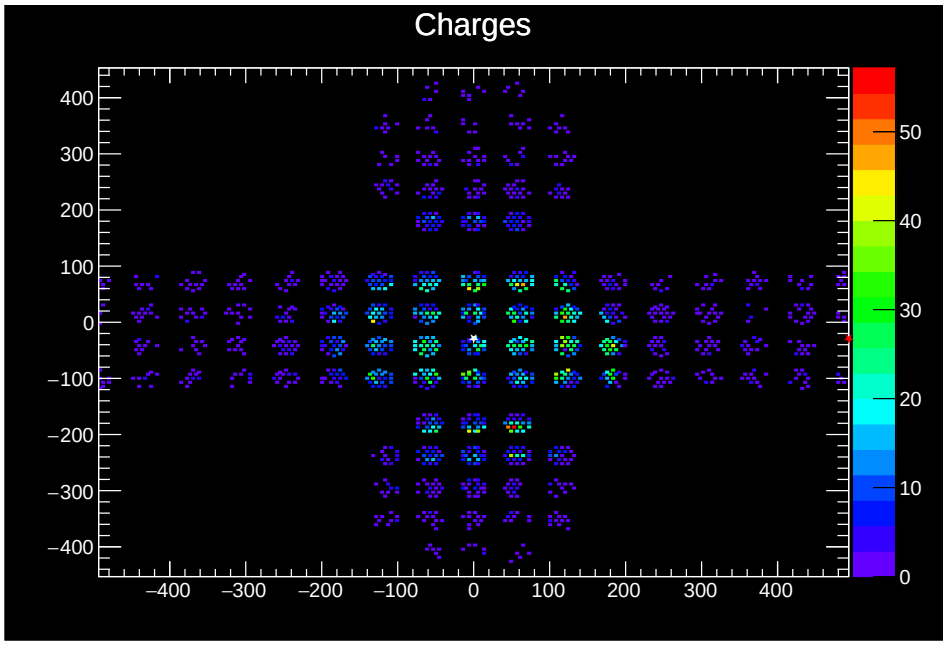


Figure 2.10: A water Cherenkov ring corresponding to a 800 MeV/c π^0 entering the barrel, as simulated by WCSim.

The second part of the water system is the water monitoring system. This system takes water samples straight out of the main detector, and monitors the water quality by measuring parameters like salinity and conductivity, ensuring that they stay inside given bounds, while also measuring light diffraction in water. Part of this system is also an osmosis tank for further water filtration [36, 37].

As the system is under pressure, in case of a leak, the water inside could be pumped out in few minutes. This is prevented by a setup monitoring pressure, flow and water height level inside the detector, while also having water detectors in strategic positions,

where the water would most likely leak. When a system parameter deviation is detected, the pump that circulates the water is shut off, and an alarm sounds, notifying personnel on site.

In later runs, the water inside the system was enriched by gadolinium. For that purpose, a gadolinium mixing tank and a gadolinium removal tank are also prepared in the staging area of the water system. Because gadolinium is considered toxic, a Gd removal setup also had to be assembled and was also put in the water system area.

2.3 WCTE physics plan

WCTE is an experiment with a rich physics programme. On one hand, this experiment is used to test technologies for the IWCD and HyperK detectors, but it also has plans to do measurements of particle cross sections, which can also be useful for other experiments.

To measure all important interactions, a measurement of a beam of particles for different beam monitor setups and also different main detector configurations has to be done. For that reason, WCTE has two main phases, with each phase also having several data taking runs with distinct configurations. The two main phases are the ultra pure water phase and the gadolinium-enriched water phase.

2.3.1 Ultra pure water phase

Ultra pure water phase of the experiment is meant for measuring the response of water Cherenkov detectors to charged particles. The first goal of this run is to measure the pion response in water [37, 38]. This would then enable discriminating between non-interacting pion and muon events in other water Cherenkov detectors, while at the same time measuring their cross sections in water. Understanding this will have a significant impact on measuring the charged current single pion interactions, i.e. neutrino interactions that produce a single charged pion as described in Chapter 1.

Second goal for the run is to measure the electron, muon and pion particle identification capabilities in water, i.e. to measure the Cherenkov rings of all different particles in a wide range of energies, and test the reconstruction algorithms on this data set for future neutrino interactions in Hyper-K and IWCD. Part of this is also testing the ability to reconstruct the primary particle energy from the detector response, and vertex positions of interactions [37, 38].

Next purpose was to measure scatterings of electrons and muons on atomic nuclei. For this, a beam with the momentum of around 800 MeV/c is used, with a longer data taking required to gather enough data, as muon-nucleus scatterings make up around 1 % of muon interactions [37].

Another setup is also used during a pure water phase, which is the tagged photon run. During this detector configuration, all beam detectors are lowered out of the beamline, and the permanent dipole magnet is put inside the beamline. This causes the charged particles to be diverted away from the beamline, with the only particles continuing to the main detector being neutral particles, mainly photons created through positron bremsstrahlung on the T2 detector [36].

This configuration enables the measurement of interaction products in water. This is needed for measuring the difference between the photon EM showers and the electron EM showers inside the detector. Using this data, it should be possible to reject events that are created by high energy photons entering the detector [36].

Next, several high energy configurations were planned to study proton response in water, as protons are also produced in neutrino interactions, as can be seen in Reaction (1.6). It is also useful for dark matter search in water Cherenkov detectors [46].

Lastly, kaon measurements were also done, since kaons are produced e.g. in a tau lepton decay, and are theorized to be a product of proton decay. This data can then be used to search for proton decays and atmospheric tau neutrinos [46].

2.3.2 Gadolinium enriched water phase

This phase is designed to measure neutron events inside the water tank. These neutrons will interact with the gadolinium nuclei, producing a delayed gamma ray that will then be detected by the mPMTs, allowing the tagging of these interactions in water.

Being able to measure neutrons is important for finding the neutrino and antineutrino separation, since they each produce a different final state as seen in the Process 1.6, where neutrino produces a proton, and antineutrino produces a neutron in quasi-elastic scattering. This is also important to differentiate from secondary neutrons produced by protons, stopped muons or $\pi^{\pm}$ [46].

Another important interaction that gadolinium doping enables to explore is the measurement of the two-body current mechanism. This process is not well explored and is a background for CCQE processes. In this process, a neutrino interacts with two nucleons in a nucleus, emitting them out of the nucleus - from this it is called a two particle two holes (2p-2h) interaction [47].

Next essential part it enables to do is looking at photonuclear interactions by neutron measurement, where the gamma photons (produced e.g. via positron bremsstrahlung) interact with a nucleus, breaking it up to protons and neutrons. This can create another background process to neutrino interactions [46].

Last physics goal of the gadolinium run was to check a Lithium-9 isotope production from π^- [46]. This interaction, where a stable nucleus produces an unstable ^{9}Li isotope, happens via a π^- capture. The produced lithium then decays into ^{8}Be, emitting a neutron and an electron in the process. This mimics the inverse beta decay, and being able to differentiate from this process is key to increased precision of DSNB - diffuse supernova neutrino background measurements [48].

Chapter 3

Assembly of the WCTE experiment

As a member of the WCTE collaboration, I had the opportunity to participate in the assembly and commissioning of the experiment. Once in August 2024, to help with the commissioning of the experiment, and in February 2025 again to prepare the experiment for the 2025 run after the winter break.

3.1 Autumn 2024 assembly

In August 2024, the main detector was being assembled. besides a contribution during this period to mPMT module preparation, my main work was in preparing the water circulation system for the run.

3.1.1 mPMT modules preparation

The mPMT modules have been prepared externally, and were shipped to CERN to be attached to the interior construction of the detector. To increase detection efficiency, the mPMTs had to be cleaned from any dust, as it could disperse or absorb the light that would otherwise enter the PMTs. For that reason the surface was cleaned by a cleaning alcohol. The attachment of the mPMTs to the support structure was done by the CERN crane crew, as the mPMTs are heavy - around 50 kg for IWCD mPMTs and up to 80 kg for the FD mPMTs. The mPMT preparation was done by specialists.

3.1.2 Water system construction

As mentioned, the main part of my stay at CERN was focused on assembling the water system of the detector, mainly the top end cap part. To circulate water through the detector, the water system has to have inputs to pump the water inside the detector, and outputs to drain the water if its level gets too high.

The piping in the detector had to have been assembled according to the CAD model (shown in Figure 3.1) prepared by the water system specialists. After assembling the structure, it was dry fitted to the detector construction in the assembly area of the experiment hall in order to remeasure the dimensions of the pipes and to find out whether they fit the actual detector. During this process it was found out that several pipes were too long, causing the clamps holding the piping to slide off the structure. These pipes were shortened and, after final checks, glued together.

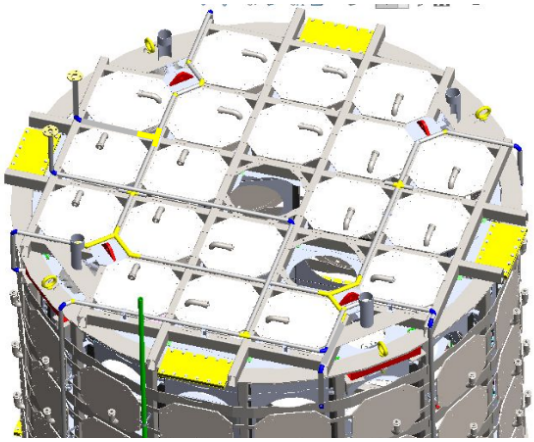


Figure 3.1: CAD model of the Top cap piping in the WCTE experiment. Created for an internal collaboration meeting.

3.2 February 2025 assembly

Over Christmas 2024, the CERN East Area was closed, so the experiment was put on hold. Due to that, after the East Hall was open to use, remeasurement of all the detectors was needed to check for any possible changes that could have happened while the detectors were not working. I volunteered to come to CERN during this time to help with this process.

3.2.1 Beam monitors assembly

First part that had to be done before assembling the beam monitors setup was to check all the detectors that use PMTs on the oscilloscope, and check for any light leaks in the detectors. After looking at the 2024 data, it was also decided that some detectors that were used in the setup did not have sufficient accuracy, so they needed to be replaced by different technologies. These new detectors that arrived also had to be tested after the transit to check for any damage that might have happened during transport. In preparation for the next run, there was also a lot of cable management that had to be done in order to plug in the new detectors, including the signal and high voltage (HV) cables.

The work on site began by cleaning up the area inside the experiment hall. The cables had to be rearranged to be closer to the detectors for easier movement and orientation around the main readout computer. The experiment area was cleaned up before the new detectors arrived to CERN, after which the detectors arrived, the detector testing started. Each detector was tested in similar way. First, the signal output of the detector was plugged into an oscilloscope. After that, high voltage was connected to the detector and a check was done for dark detections and any light leaks of the PMT, that might have been caused by tape that fell off. If found, the light leak was covered by additional black vinyl tape. Fortunately, there were no major light leaks.

Other than the detector themselves, the amplifiers that were going to be used also had to be tested. The testing was done similarly to the detectors by reading the input and output in an oscilloscope. If any amplifiers were found to have connection problems or did not amplify the signal to a similar level as the rest, they were replaced.

One major problem was detected when measuring the aerogel Cherenkov detectors.

Their detector walls are made of thin black mylar, with a thickness on the order of micrometers, to minimize ionization losses as the particles pass through the material. It seems that during the winter intermission, the material might have deteriorated, as there were noticeable light leaks from the background light. For that reason, additional thin black vinyl tape was applied to the entry and exit windows to reduce this light leak.

Additionally, there were also new holders for the ACT photomultiplier tubes. As there are only 12 PMTs that need to be removed each time the aerogel configuration is changed, the cases need to be simple to remove, and still have good light blocking capabilities, not allowing any light to get inside the box. The cases that were used during the 2024 run had a design issue that sometimes caused the signal and high voltage wires to bundle at the back of the PMT, not allowing the PMT to fit inside the case, and complicated the switching procedure. The new design got rid of this problem by widening the hole that connects the end cap and the rest of the case. To use these new cases, the end caps connections to the new cases had to be soldered.

Another objective was to test the new time of flight detector, as it used a technology never before used for the experiment. The whole detector was operated by a LoLX board, that needed to be connected to the beam area computer. Through this board the voltages on the amplifiers were set, and also the signal from SiPMs could be read out.

After completing the dark detection testing, detector responses to light had to be tested. For that purpose a near-UV LED laser was used, which was connected to the detectors by light fibers. The LED laser was operated by connecting it to a function generator, that produced a TTL square wave (0 to 3.3 V) at 10 kHz. The laser itself was also connected to a computer in the beam area, from which the laser was started and stopped. The measurement was performed by splitting the trigger signal that activated the laser, and connecting it to the oscilloscope. The oscilloscope was then triggered by this signal, and the response from the detectors was measured. The signals of the PMTs connected to the same detector should be ideally the same. This was not observed in one of the PMTs on the T0 detector, as the signal it produced was too small. For that reason it had to be replaced.

An exception to the described procedure was LED testing of the TOF detector. Due to not having the light fiber connected properly, the light from the fiber did not enter the scintillators, and therefore did not register any signal. Due to that this detector had to be tested in a different way. The method of testing the TOF detector is described in Subsection 3.2.3.

3.2.2 Detector and readout testing

The detector data readout was tested together with the LED laser testing of the detectors. The whole readout was done by the same computer in the beam area that controlled the laser.

The readout testing was done by triggering the data taking software with the same signal, that started the LED laser. The LED laser was then connected to T0, T1, HC0, HC1, ACT0 and ACT3 boxes, since these detectors had light fiber input. These detectors had HV on and signal cables connected. Since the trigger had a rate of 10 kHz, the data taking software only had to be turned on for a short time to get a reasonable amount of data to analyze.

After taking data, it was analyzed by a script written by another member of the

collaboration. During this analysis, there was a problem with the readout detecting additional trigger peaks from T0 and T1 detectors. This was thought to have been caused by the readout card, so called Constant Fraction Discriminators (CFD), which detect the time hit of the detector signal. By increasing the time sensitivity of the CFDs this second peak occurrence decreased, but it did not remove it completely. In the end, it was found out that other than one of the CFDs, all other modules had the same problem. Due to that, the important trigger detectors were reconnected to the CFD module that was not malfunctioning, which reduced this problem to reasonable levels for analysis.

3.2.3 Segmented time of flight detector testing via cosmic rays

During the assembly in February 2025, the new time-of-flight detector design had to be tested, since it hasn't been used in the beam configuration before. First attempt to test the detector was via the light fiber inserted into the detector, which was cut in places corresponding to each scintillator block. It turned out that the cut was not deep enough for light to leak out of the fiber, so another way to test the response of the detector had to be found.

To test if the SiPMs in the detector work, measurement using cosmic muons was done. The setup for testing this consisted of the thin T3 detector, which was used to choose the scintillator tile to be measured, the TOF detector itself, and the hole counter on the bottom. The setup can be seen in Figure 3.2 The testing principle was as follows: Measurement was triggered on the coincidence of the T3 and HC detectors, and either the detectors attached to the same detector strip were read out, expecting a coincidence in detection, or two different strips were read out, which should result in only one of detectors measuring a signal.

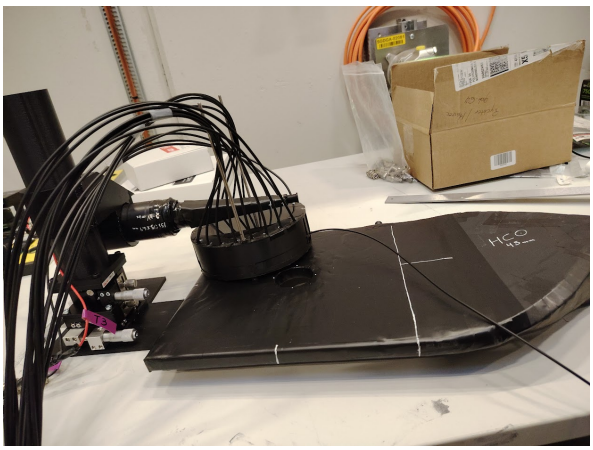


Figure 3.2: Testing setup that was used for testing the TOF detector via cosmic rays, the T3 detector is on top, the tested TOF detector is in the middle, placed on the HC detector.

At first, an oscilloscope was used to do primary testing. Two of the oscilloscope channels were used for the triggering detectors - T3 and HC, and the two remaining for two of the channels from the TOF detector. This testing ended successfully, measuring clear peaks in the SiPMs in coincidence with the HC and T3 detectors. The results of testing same scintillators were as expected, where both SiPMs triggered at the same time. This can be seen in Figure 3.3, where the yellow and blue signals represent the T3 and HC detectors respectively, and the violet and green signals correspond to the

signal from the SiPMs. In the case of testing scintillators connected to neighboring scintillator strips, the results were also the same as expected, where only one of the detectors always fired, and no light contamination from the hit scintillator was detected. The oscilloscope measurement for this setup can be seen in Figure 3.4

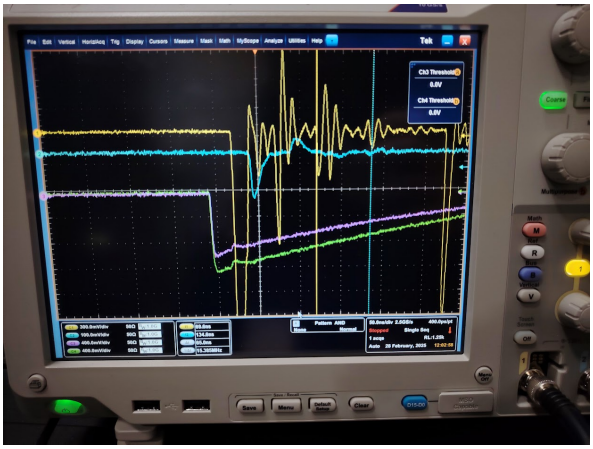


Figure 3.3: Photo of the TOF detector testing using cosmic muons and an oscilloscope. Yellow signal is the T3 detector, blue is the HC detector, purple and green are two opposite SiPMs on the same scintillator. A clear coincidence can be seen on all the detectors, when accounting for signal delay from different PMTs and cable lengths used, confirming a cosmic muon detection, and the working state of the TOF detector.

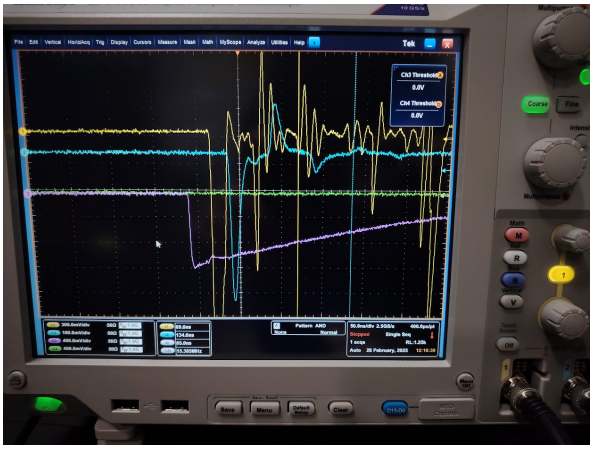


Figure 3.4: Photo of the TOF detector testing using cosmic muons and oscilloscope. Yellow signal is the T3 detector, blue is the HC detector, purple and green are two SiPMs placed on neighboring scintillators, Only one of the SiPMs is firing at a time, showing no light exchange between scintillator stripes.

After ensuring the working state of the detector using the oscilloscope, a more stringent testing using the data readout was done. To use the actual readout, the data taking modules had to be set to only trigger the data taking on HC and T3 coincidence. To do that, a coincidence module was used, with T3 and HC plugged in. Then, several runs were measured, each taking several hours to get enough events to analyze, as a cosmic muon flux of one particle per minute per centimeter can be expected. Each run was done for a different T3 position, moving it above a different scintillator each time.

The first run was started with the T3 detector positioned above the scintillator numbered as 7 in Figure 2.5, and proceeded towards the scintillator 0. After the run

finished, the number of hits in each detector strip on the strip number was plotted. The plot can be seen in Figure 3.5, showing that a clear majority of the events were detected in the chosen scintillator. The detections in other scintillators is due to cosmic muons arriving from higher azimuthal angles.

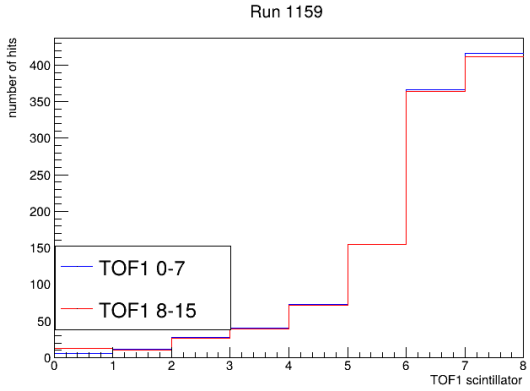


Figure 3.5: Measurement of TOF detector cosmic ray testing showing number of hits in opposite photodetectors as a function of scintillator number. Data was taken in run 1159, where the T3 detector was in position above the scintillator 7 in the TOF detector.

The measurements were repeated with different T3 positions. What was expected was to detect the most detections in the scintillator stripe above which the T3 detector was positioned. This was true for the following run, where the T3 detector was positioned above scintillator 6, which can be seen in histogram shown in Figure 3.6. Here it is clear, that the scintillator 6 is getting the most hits as expected, with decreasing number of hits in neighboring scintillators.

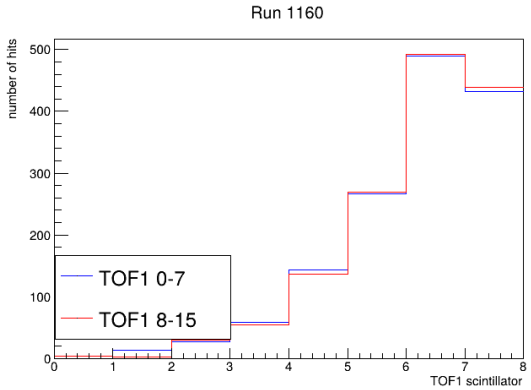


Figure 3.6: Measurement of TOF detector cosmic ray testing showing number of hits in opposite photodetectors as a function of scintillator number. Data was taken in run 1160, where the T3 detector was in position above the scintillator 6 in the TOF detector.

Afterwards, the next measurement with T3 above scintillator 5, see histogram in Figure 3.7, was plotted. This histogram shows that the previous scintillator is getting more hits than the one that T3 is positioned above. From this it was reasoned, that the waveguide, that connects the T3 scintillator to its PMT, is getting enough Cherenkov light, that it triggers the PMT, causing the noticed irregularities. This was further exacerbated by the waveguide widening, the closer it was to the PMT, which resulted

in a larger effective area for detection, and therefore increasing the number of detections even in smaller scintillator stripes. Due to this, the setup was changed for further runs, putting the T3 detector above the TOF from the side from in between the outgoing data cables, trying to minimize the surface area of the wave guide above different scintillators. This resulted in removing this effect, with muons going through the expected scintillators more, than in the previous case, as can be seen in Figure 3.8.

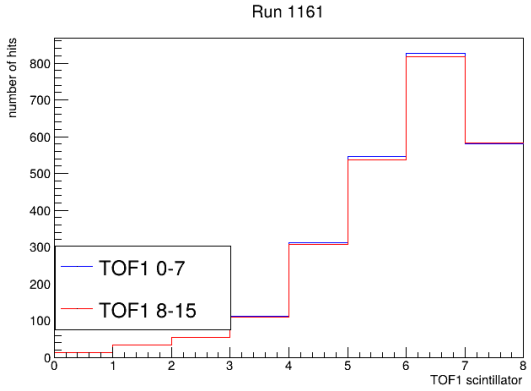


Figure 3.7: Measurement of TOF detector cosmic ray testing showing number of hits in opposite photodetectors as a function of scintillator number. Data was taken in run 1161, where the T3 detector was in position above the scintillator 5 in the TOF detector, with the waveguide of the T3 detector placed above scintillators 6 and 7.

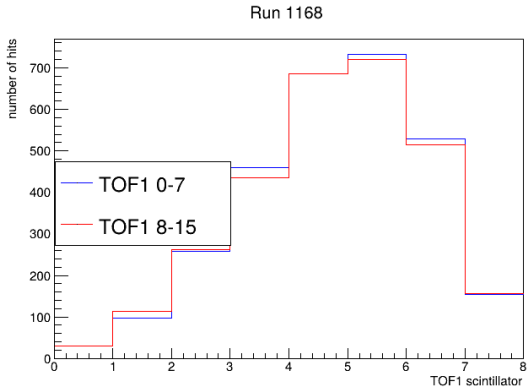


Figure 3.8: Measurement of TOF detector cosmic ray testing showing number of hits in opposite photodetectors as a function of scintillator number. Data was taken in run 1168, where the T3 detector was in position above the scintillator 5 in the TOF detector, with the T3 detector entering above the scintillator from the side.

The testing of the rest of the strips was subsequently completed without any further issues. After changing the configuration, the results of the measurements were as expected, with the largest number of hits being always under the T3 detector.

It was also planned to try a calibration run, through placing the T3 detector above a longer scintillator into several different positions and measuring the timing difference between the opposite SiPMs, but unfortunately due to a technical error in the connection to the data taking computer, and upcoming start of the data taking run, there was no more time to realize it.

Overall, the testing was a success, ensuring the proper function of all the SiPMs in the TOF detector, which made it ready for the data taking run.

3.2.4 WCTE shifts

Besides the assembly work, I also helped to fulfill our institute's obligations to the experiment by participating in data taking shifts. I took part twice in total, once in November 2024 and then during my participation in the experiment assembly in March 2025.

Both times, the duties consisted of doing periodical water system checks, where a patrol had to be performed, to look for any water that spilled out of the system and was not flagged by the different safety systems. It was also the shifters responsibility to start and stop data taking runs, changing beam energies and detector configurations, while also logging any setting changes and abnormalities that occurred during the shift.

Changing the beam energies was done using an internal CERN software, that set the beamline magnets intensities and collimator slit sizes to choose the desired beam energies and configuration.

To change the detector elements in the T9 beamline, a beam stopper had to be inserted into the beamline through the beamline setting software, so that it was safe to enter the beam area. There were two main configuration changes that had to be usually done. The first one was to change the ACT boxes for a different refraction index, to correspond to different beam energies. The second change was to raise or lower the lead glass in/out of the beamline.

Chapter 4

Simulations for the WCTE experiment

Other than participating in the detector assembly and in the data taking shifts. I also worked on two separate simulation and analysis tasks, expecting them to be useful during the data analysis, or for calibration of the detectors. The first task was simulating detector response in the time of flight (TOF) detector for different detector designs using a custom simulation code. The second task was developing a simulation of cosmic rays entering the main detector in the official package for water Cherenkov simulations WCSim.

4.1 Time of flight detector simulation and particle position reconstruction

The first simulation I designed for the experiment was a toy model of the different time-of-flight detector designs that either were planned to be used or are being used in the beam monitoring setup. In total there were 3 main detector designs that were simulated, and in the end only two of them ended up being used. The main purpose of my toy model was to simulate a response in the photomultipliers of the detector, and then use that response to reconstruct the primary particle position. I then tried to apply the same reconstruction to the real data. The complete simulation code can be accessed at [49].

The primary purpose of this simulation was to have a simple way to show a beam profile for online monitoring of the data taken during a run. This needed a lightweight and fast way to reconstruct particle positions, that could have been running in the background of the experiment to monitor for any anomalies. In the end, plans for online monitoring were scrapped, and the focus of this simulation switched to studying the feasibility of using charge data from the detectors (i.e. integrals of the waveforms) to reconstruct primary particle positions in scenarios where time-based reconstruction was not feasible.

4.1.1 Method of simulating the detector response

The simulation was using a toy model of the different detector designs. I created the simulation using the ROOT [50, 51] analysis package, with the code written in C++.

The first method I considered when reconstructing the particle positions was that

the signal in the detector would be proportional, due to attenuation effects, to a falling exponential function

$$Q_i \propto e^{-|\boldsymbol{r}_i - \boldsymbol{r}_{\text{beam}}|/\lambda} \ , \tag{4.1}$$

where Q_i is the charge (signal) in a detector, $|\boldsymbol{r}_i - \boldsymbol{r}_{beam}|$ is the distance from the particle interaction point in the scintillator to the detector and λ is the attenuation length. Using this relation I estimated the primary particle position by summing up the SiPM position vectors weighed by the detector charge

$$\boldsymbol{r}_{\text{particle}} = \frac{\sum_i Q_i \boldsymbol{r}_i}{\sum_i Q_i} \ , \tag{4.2}$$

where $\boldsymbol{r}_i$ are the photosensor coordinates. This was a good first approximation, but upon closer examination it tended to underestimate the particle positions, shifting them closer to the center than they should have been. Therefore, I had to find a more accurate way to reconstruct the positions.

After receiving feedback from collaboration members, that the number of photons reaching the detector should be inversely proportional to the distance from the detector, I modified the simulation of the detector response as follows: I assumed that the signal strength is directly proportional to the number of photons hitting the detector, i.e.

$$Q_i \propto N_i \ , \tag{4.3}$$

where Q_i is the charge in the i-th detector, and N_i is the number of photons reaching the detector i. When a particle passes through a medium, it acts as a point light source. Assuming, that photons are emitted uniformly in all directions, the photon flux is given by the inverse square law

$$\Phi_{\text{photon}} = \frac{P}{4\pi r^2} \ , \tag{4.4}$$

where P is the emitted power and r is the distance from the source. The number of photons reaching a detector with an effective area S is

$$N_i \propto \frac{1}{4\pi r^2} \cdot \cos(\theta) S \ , \tag{4.5}$$

where θ is the angle between the detector surface and the photon direction. With the approximation that all detector effective areas are the same and the detectors are perpendicular to the source, the signal in the detector will be dependent only on the squared distance of the detector from the source, and the charge in the detector will be

$$Q_i^{\text{det}} \propto \frac{1}{|\boldsymbol{r}_i^{\text{det}} - \boldsymbol{r}^{\text{particle}}|^2} \ . \tag{4.6}$$

This dependence was then used to get an approximation, without taking into account light attenuation of the material.

While light propagates through the scintillator, some photons are also lost due to interactions with the medium. The number of photons traveling through the environment can be described by

$$N_{\text{photon}}(\boldsymbol{r}) = N_0 \cdot e^{-\frac{|\boldsymbol{r}|}{\lambda}} \ , \tag{4.7}$$

where λ is called the attenuation length and is a property of the material. The total signal in the detector is given by the product of equations (4.6) and (4.7), resulting in the final relation:

$$Q_i^{\text{det}} \propto \frac{1}{|\boldsymbol{r}_i^{\text{det}} - \boldsymbol{r}^{\text{particle}}|^2} \cdot e^{-\frac{|\boldsymbol{r}_i^{\text{det}} - \boldsymbol{r}^{\text{particle}}|}{\lambda}} \ . \tag{4.8}$$

For particle reconstruction, only a comparison of the charge values between detectors is needed, so the constant factors in the equation are neglected.

The scintillator used in the experiment was the Eljen-228 organic scintillator, which is based on polyvinyltoluene [52]. Since this scintillator has a very long light attenuation length of $\lambda = 120$ cm, and the detectors themselves are compact, the expected influence of the exponential term on the final charge value can be considered negligible and was therefore often neglected.

To simulate the detector response, a point inside the detector is created as a particle hit, and using equation (4.8) a detector response in terms of the charge in all of the detectors is generated. To reconstruct the primary particle position, the previous equation would have to be inverted, but applying this directly is not straightforward. Instead, numerical methods are used to estimate the most probable position. The chosen method was to minimize the χ^2 of the detector response, and using the result to determine the best-fit particle position. The χ^2 of the detector response is

$$\chi^2 = \sum_i \left(\frac{Q_i^{\text{meas}}(x,y) - Q_i^{\text{theoretical}}(x,y)}{\sigma_i} \right)^2 = \chi^2(x,y) \ , \tag{4.9}$$

where Q_i^{meas} is the simulated data and $Q_i^{\text{theoretical}}$ is predicted by equation (4.8). Parameters x and y representing the particle position are treated as variables. The symbol σ represents the detector charge uncertainty, and considering that all detectors are identical, their uncertainty must also be the same. As such, it can be set that $\sigma = 1$ for all the detectors. Then, a minimizing algorithm is used to find the position, for which $\chi^2 \to 0$, which will be the reconstructed particle position.

After testing a single particle position, a more complex shape was tested to study how a Gaussian profile would be distorted. Finally, a grid of points was simulated and analyzed to see how the reconstruction performs for different primary particle positions. If the grid reconstruction returned good results, I tried to apply it to measured data from the experiment, where possible.

4.1.2 Round scintillator tile TOF detector simulation and position reconstruction

The first design to be simulated was a design used during the 2024 run. This design consisted of a round scintillator tile, on which silicon photomultipliers were arranged. Initially, it was planned to use only 8 SiPMs, which was later increased to 16. A sketch of this detector can be seen in Figure 4.1. This detector uses the organic scintillator EJ-228, which has a very long attenuation length of approximately 130 cm. This is advantageous, as the radius of the scintillator is only 3 cm for the upstream detector and 4 cm for the downstream detector.

Since the first design planned to use 8 SiPMs, the first toy models were based on 8 detectors. This was later updated in the simulation to include 16 SiPMs.

To test the viability of the simulation, I first placed a point inside the scintillator at a random position, Then I generated the signal in all the SiPMs using Equation (4.1), using on purpose a different $\lambda = 1$ than the attenuation length of the material, and scintillator radius $r = 1$ cm. I also put the scaling factor of the Equation (4.1) $A = 1$, functioning as the maximum signal strength. After generating the detector response I did position reconstruction using Equation (4.2), so far without dividing the sum by the total charge collected by the detectors. From this, I got reconstruction shown in

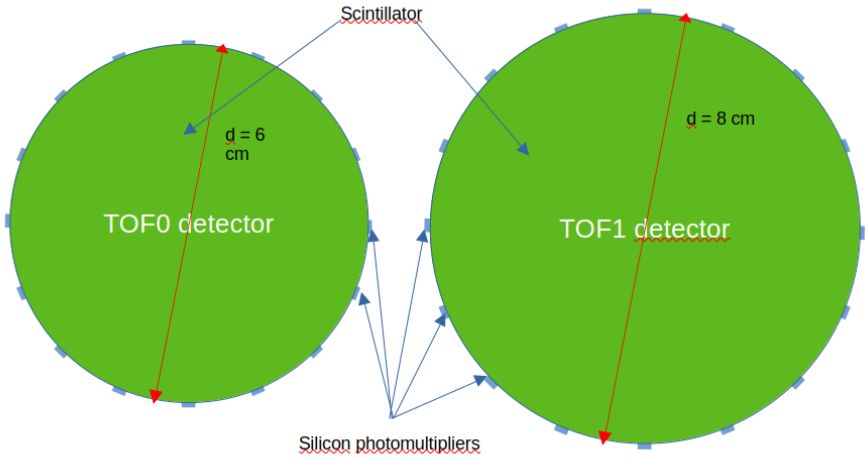


Figure 4.1: A sketch of the 2024 TOF design. There were two time of time detectors, TOF0 was smaller and upstream in the beamline, TOF1 was inserted into the barrel inlet pipe, both were surrounded by a construction that contained readout electronics.

Figure 4.2. The left graph shows the primary particle position, and the right one the position after the reconstruction. In this graph, it can be seen that for the used values, the reconstructed point shifts slightly too far out, but the direction of the particle fits. After that I added the division by total charge, which resulted in Figure 4.3. Here, the opposite can be noticed, as the position is too close to the middle of the detector. To get a more realistic reconstruction, the λ parameter of the simulated charge had to be changed.

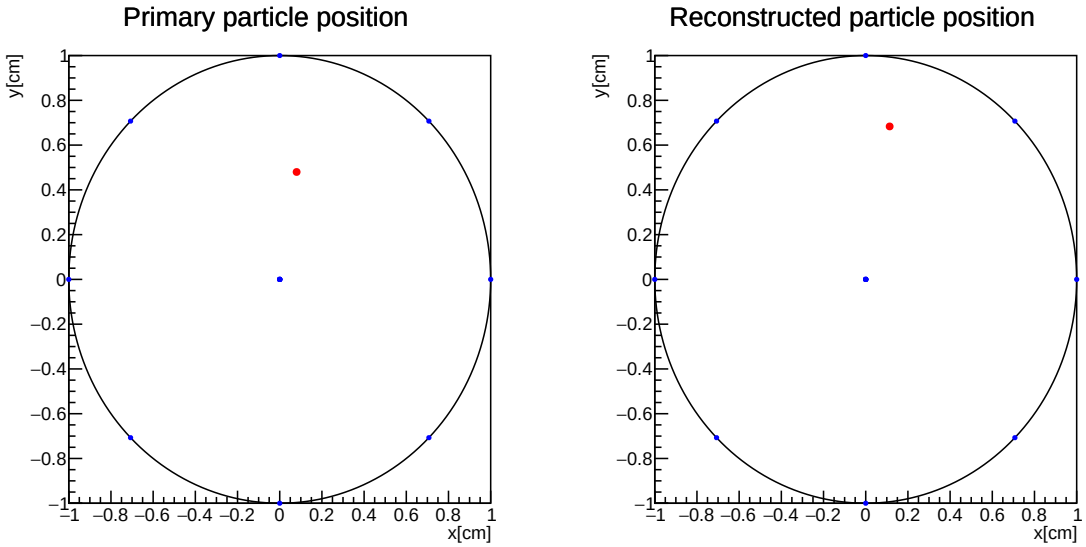


Figure 4.2: Particle position reconstruction from weighted charge sum, without dividing by total charge.

At first, I continued with the first approach, without dividing by total charge. In the next step I generated a more complex shape, and created a detector response using different λ values. This was done in order to check how this method of reconstruction

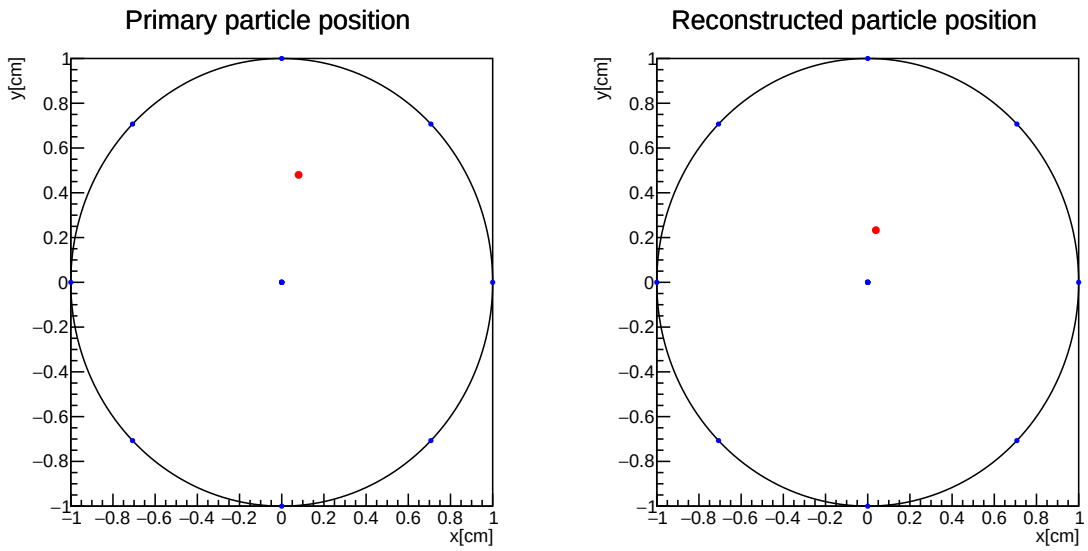


Figure 4.3: Particle position reconstruction from weighted charge sum divided by total charge.

distorts more complex shapes. I tested this using four different λ values ranging from 1/2 to 2. The shape reconstruction can be seen in Figure 4.4, where it can be noticed, that depending on the λ value the shape stays approximately the same, which suggests that this method of reconstruction has good shape preserving properties and therefore should keep any structure that might be measured in the beam profile, only changing the magnification of the shape, with possible distortions of the shape at the edge of the detector. The values of $\lambda = 2$ and $\lambda = 1/2$ were the most similar to the primary positions.

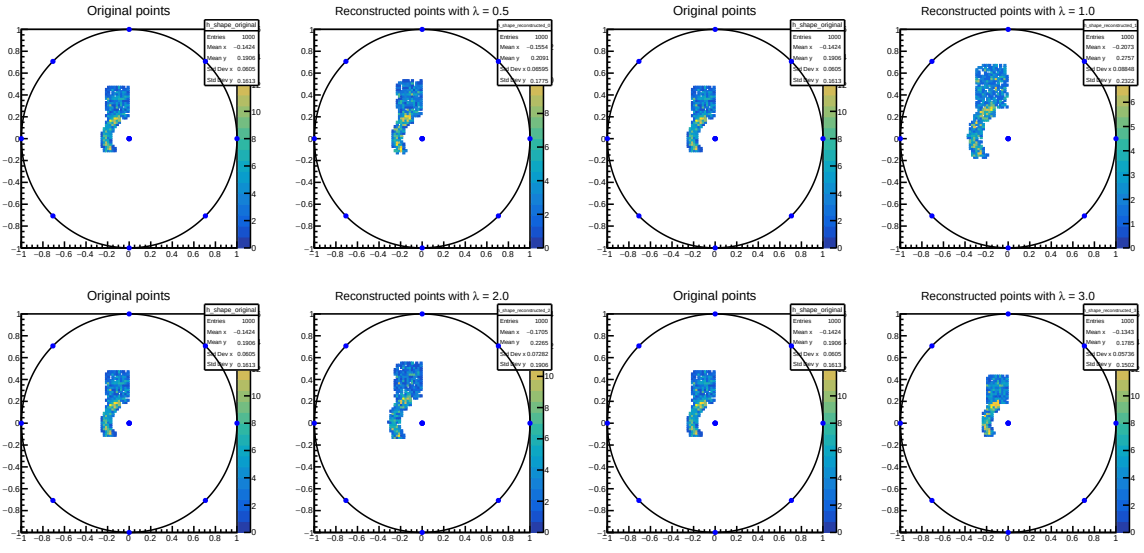


Figure 4.4: Complex shape reconstruction using unweighed charge sum with different values of λ.

To check the most suitable λ value, I generated a 2D gaussian shape from 1000 points near the middle of the detector and tried to plot a graph of how the mean range changes for different lambda values. I looped over 500 λ values, starting at 0.1 and

increasing the step by 0.1 each iteration. This resulted in the graph shown in Figure 4.5, from which it can be deduced that the original shape is best preserved for values of λ around 0.25 and 2.5.

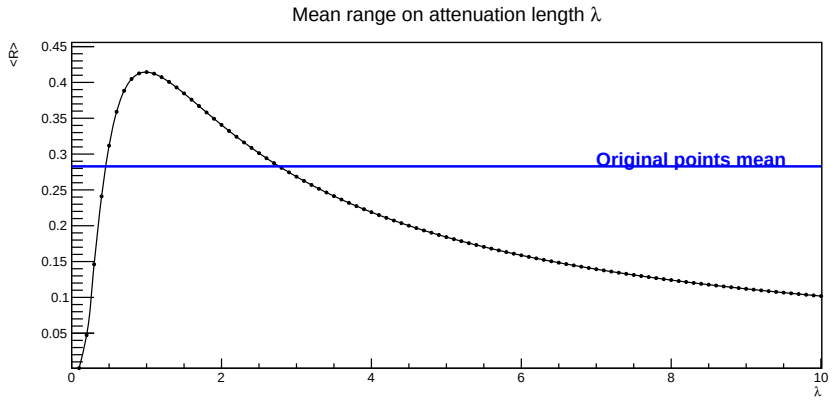


Figure 4.5: Values of a mean range of a Gaussian profile of the beam for different values of λ.

After this I changed the approach to reconstruction testing to use a grid of particles. The grid was generated by separating the diameter of the detector into a grid. By applying the reconstruction to different particles in the grid, it can be seen how particles at different positions in the scintillator move during reconstruction. When looking for the best lambda with the grid, a similar result was achieved as with the Gaussian mean value. I generated several different histograms with λ from 0.5 to 5. An example with $\lambda = 2.0$ and $\lambda = 4$ can be seen in Figures 4.6 and 4.7. For each lambda value I plotted a mean distance from the original point. This can be seen in Figure 4.8, where it can be seen that a value of λ around 0.5 or 2.5 would be the best fit.

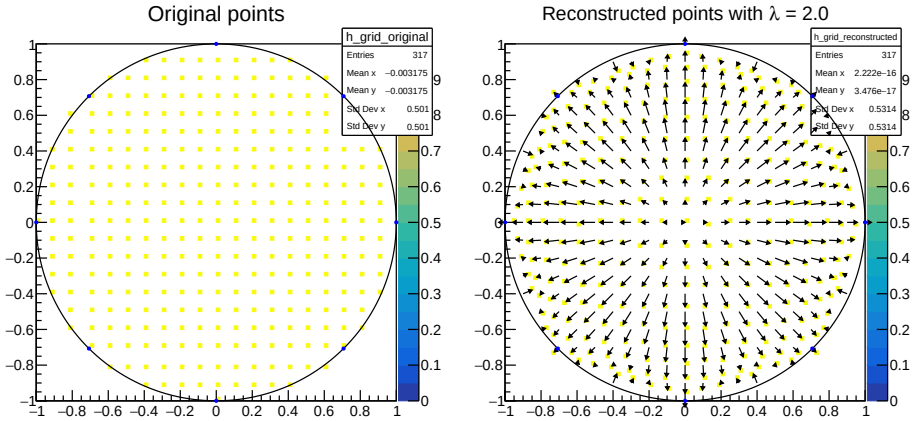


Figure 4.6: Comparison of the original grid of points on the left with the reconstructed positions of the points with $\lambda = 2.0$ on the right. The arrows show how the reconstruction moved the vertex from its starting position.

When this reconstruction method was presented during a collaboration meeting, by applying the weighted charge reconstruction, a feedback from the collaboration members was given, saying that the signal generation should also contain a dependence on the square of the distance between the particle and the detector. This resulted in updating the signal generation method to use the equation (4.8), and as the primary

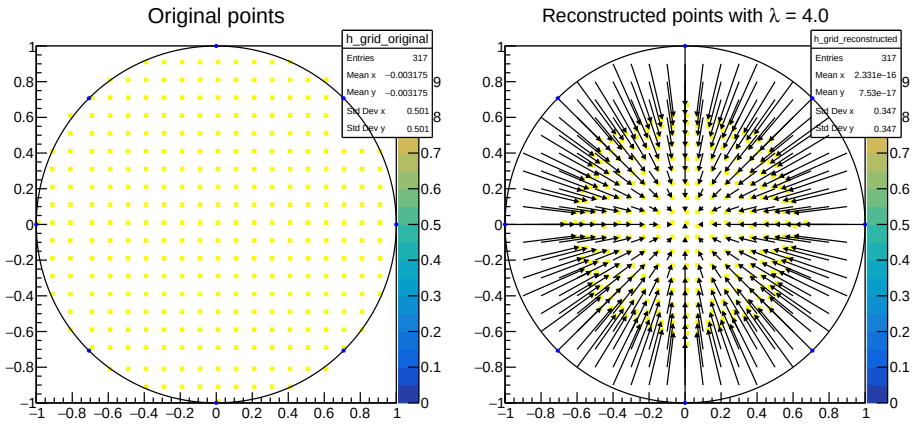


Figure 4.7: Comparison of the original grid of points on the left with the reconstructed positions of the points with $\lambda = 4.0$ on the right. The arrows show how the reconstruction moved the vertex from its starting position.

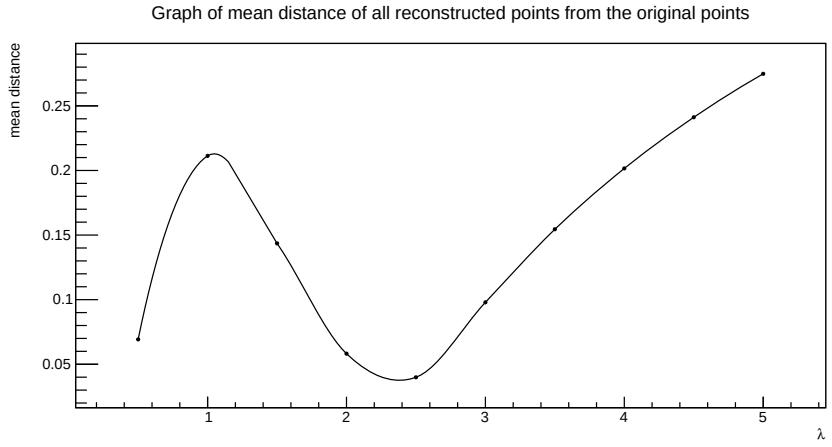


Figure 4.8: Graph of mean distances of grid points from the original points for different attenuation length values.

position cannot be obtained analytically, a numerical method was used instead. By using Equation (4.9) together with a minimizing algorithm, a reconstruction the primary particle positions is possible. At this time, the idea to have an online monitoring system, in which some simple method of reconstruction could be used to check for beam profile, was being discontinued, so this simulation and analysis was shifted to a more serious method to consider the viability of using the charge data for position reconstruction and beam profile measurement in scintillator detectors. The design was also updated to use 16 SiPMs.

At first, I just considered the first term in Equation (4.8), since the scintillator used in the detectors has a very long attenuation length of 130 cm, the exponential was considered to be much smaller than the $1/r^2$ term and so was discarded. I plotted the normalized charge in the SiPMs, that would be generated with this reasoning in Figure 4.9. As can be seen, the function of each detector is an injective function. This results in simplifying the reconstruction, and allows for more precise results. As I started looking at a concrete detector, I set real scintillator dimensions of the TOF-0 detector in my simulation to have a 3 cm radius.

To minimize the χ^2 I used the minimization algorithm Minuit2 in the ROOT library.

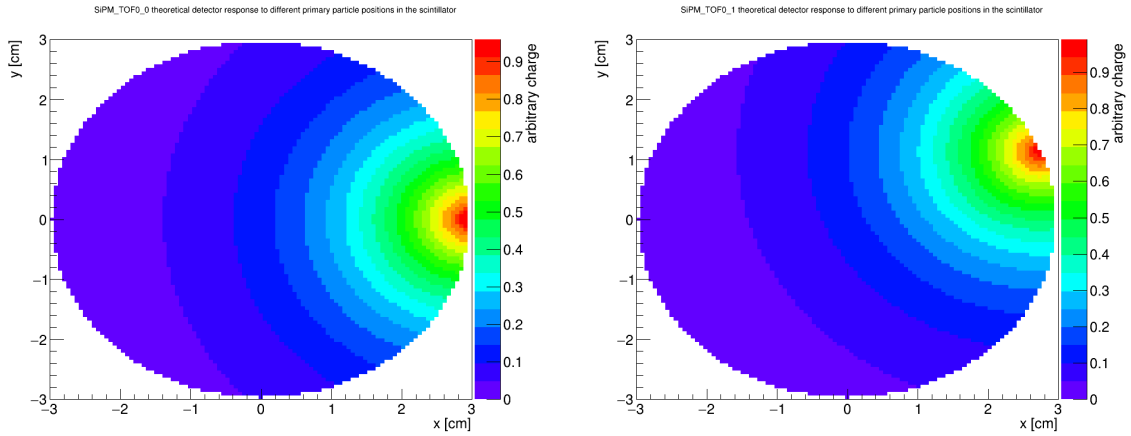


Figure 4.9: Simulated response of individual SiPMs to an ionizing particle passing through a scintillator at different positions. SiPM 0 response is shown on the left, SiPM 1 response is on the right. Other SiPMs have a similar response, with the maximum value at the detector position.

To use the minimization package, a function to be minimized needs to be defined, either as a stand alone function, or as a lambda function. This function is then wrapped into a ROOT functor type, the parameters are set, together with their starting values and step size. I set the parameters to be the x and y coordinates, with the starting point in the middle of the scintillator. By calling the `Minimize()` method, the minimization starts, and the function is called with varied parameters, which are changed according to the algorithm of the minimization. I also set a condition that the particle must be inside the detector volume

The result of the reconstruction can be seen in Figure 4.10. In the graph it can be seen that the reconstruction works very well for most of the points, except very few points in extreme positions on the detector.

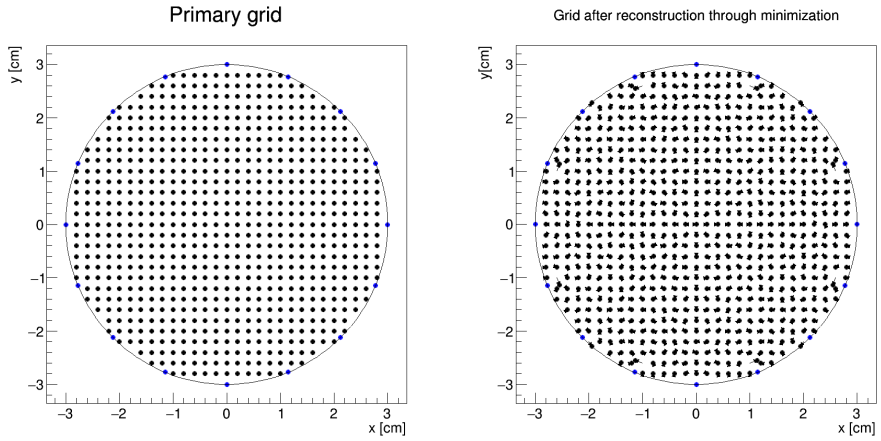


Figure 4.10: A graph of the simulated grid of primary particle points on the left and its reconstruction through minimizing the χ^2 of the detector response model on the right.

To check how valid the reconstruction is, a histogram of the distance of the reconstructed point from its primary point was made, with a plot of the χ^2 values for the inner part of the detector. This can be seen in Figure 4.11. How good the reconstruction is can also be seen by plotting occurrence of residuals of the reconstructed points

compared to the original points. This was done and can be seen in Figure 4.12, which shows that the residuals are well centered around zero, with the few points that diverge being less than a millimeter from the original coordinates. This was after cutting on the edges of the detector, where the reconstruction capabilities are worse, and is less important due to the beam profiles assumed to be smaller than the detector size at the higher energies.

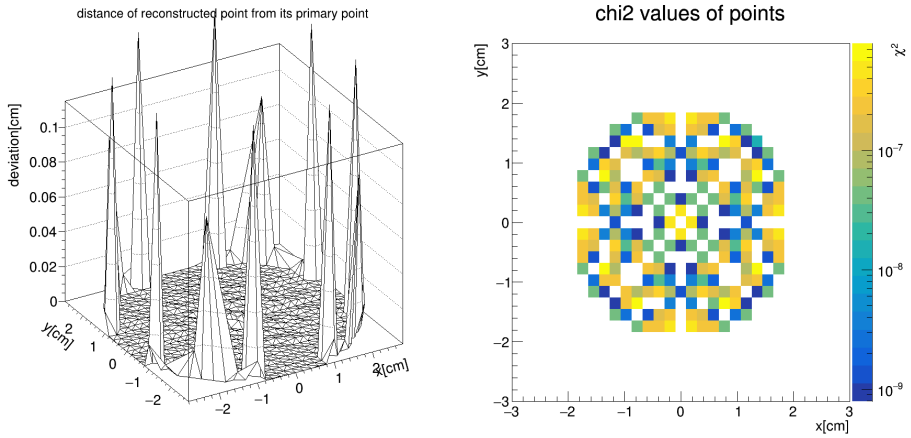


Figure 4.11: A histogram of distance of reconstructed points from their respective particle points, and the chi squared values of points in the inner part of the detector – inside a circle of 2 cm radius.

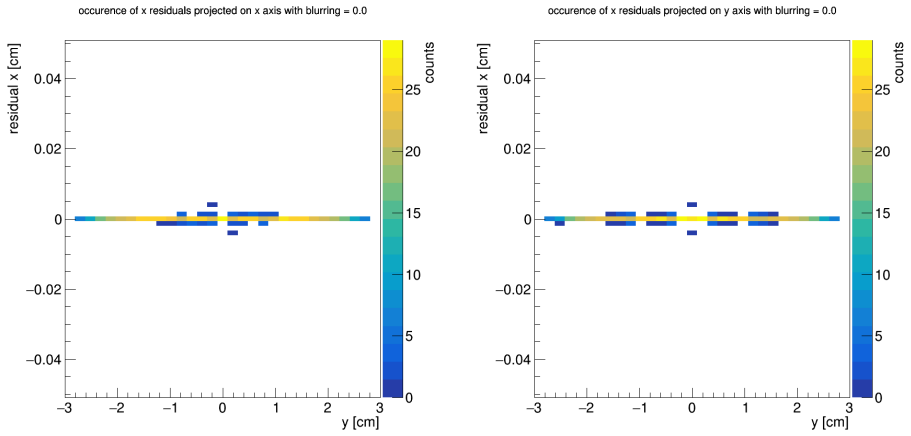


Figure 4.12: A histogram of occurrences of residuals, as projected on x axis on the left, and projected to the y axis on the right, with cut applied on extreme positions of the scintillator.

What I tried next was to see how the minimization method works compared to the weighted charge sum method. This is shown in Figure 4.13. While the inner part of the scintillator is reconstructed well in both cases, the minimization method was better in determining the outer positions in the detector. Next step was to see how the reconstruction works when the signal is modified for the presence of noise.

I modified the signal by adding a noise term that corresponds to the Gaussian distribution, resulting in total charge in a detector being

$$Q'_i = Q_i + \sigma\delta \ , \qquad \delta \sim \mathcal{N}(0,1) \ , \tag{4.10}$$

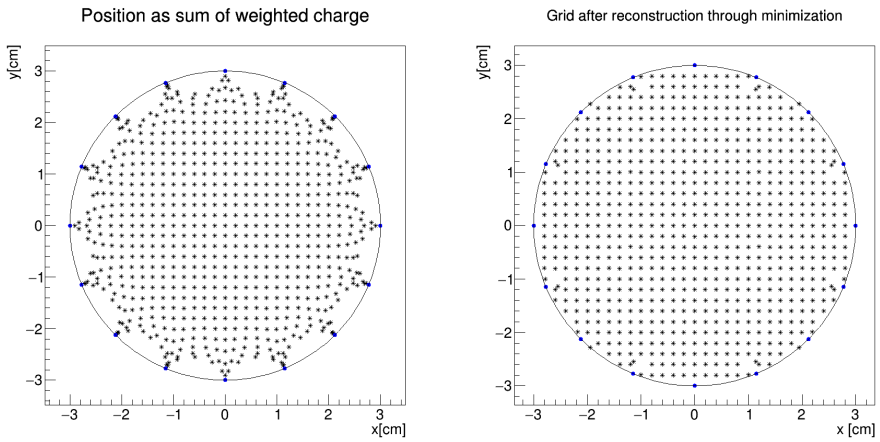


Figure 4.13: Comparison of position reconstruction of primary particles using weighted charge method on the left and χ^2 minimization method on the right.

where δ is the number generated from the Gaussian distribution, and the noise amplitude σ was a parameter that was varied to see how the response will change with increasing noise.

I first simulated a smearing with $\sigma = 0.001$, which resulted in an almost identical reconstruction. The reconstruction graphs in Figure 4.14 show that the graph of both weighted charge and minimization reconstruction methods still have comparable results. While the reconstructed points show virtually identical positions as the reconstruction with no signal modification, when looking at the residual occurrences in Figure 4.15, it is quite clear that the reconstruction is slightly worse than with no smearing, which is expected.

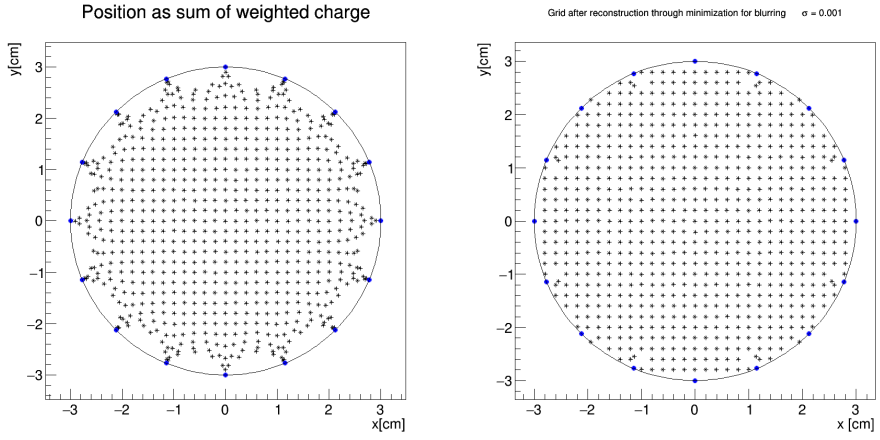


Figure 4.14: A histogram of position reconstruction comparing weighted charge method on the left with minimization algorithm on the right, with a signal smearing with $\sigma = 0.001$.

A more pronounced effect can be seen when increasing the smearing by an order of magnitude to $\sigma = 0.01$. In this case, the reconstruction is significantly worse, but the weighted charge method seems to have worse results than the minimization method. The reconstructed positions from both methods with this smearing can be seen in Figure 4.16, with a more significant residual occurrence of the minimization algorithm in Figure 4.17, but the results are still less than 1 mm from the original position.

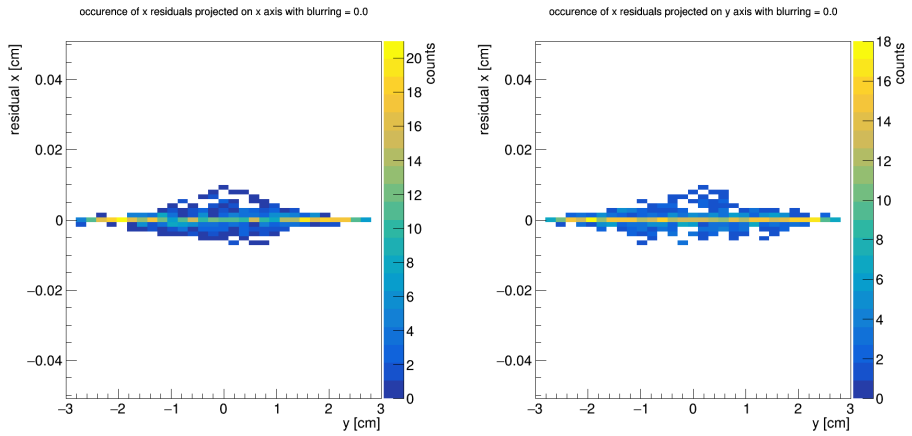


Figure 4.15: A histogram of occurrences of residuals, projected to the x axis on the left, and to the y axis on the right with a smearing value of $\sigma = 0.001$.

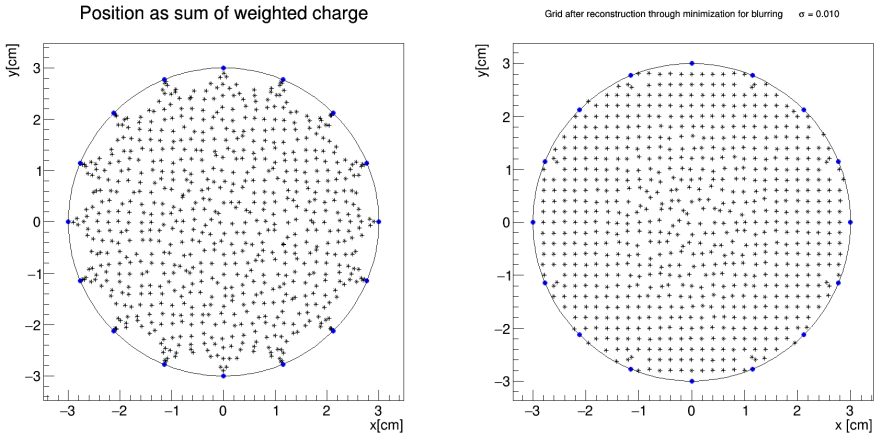


Figure 4.16: A histogram of position reconstruction comparing weighted charge method on the left with minimization algorithm on the right, with a signal smearing with $\sigma = 0.01$.

With this smearing, the signal fluctuates by up to 50 % of the original signal value, especially for the smaller signal values. The differences in the smeared signals and the original signals can be seen in Figure 4.18. Such a signal difference might be seen in real detectors.

Lastly, I ran the simulation with a large value of $\sigma = 0.1$, which resulted in a much worse reconstruction, as can be seen in Figure 4.19. This is expected, since the difference from the original simulated signal is large, as can be seen in Figure 4.20. For these reasons the residuals were also very large, as shown in Figure 4.21, so the reconstruction for significant noise becomes problematic, which is expected. Still, the minimization results were much better than results acquired using the weighted charge method.

Finally, I repeated the method while calculating the exponential part as written in Equation (4.8), with the attenuation length of the used scintillator $\lambda = 120$ cm. I have not noticed any differences in the final reconstruction

To conclude this test, it can be said that the minimization method is overall better than the weighted charge method. While the weighted charge is fine as an initial approximation, the minimization algorithm shows better results with higher smearing

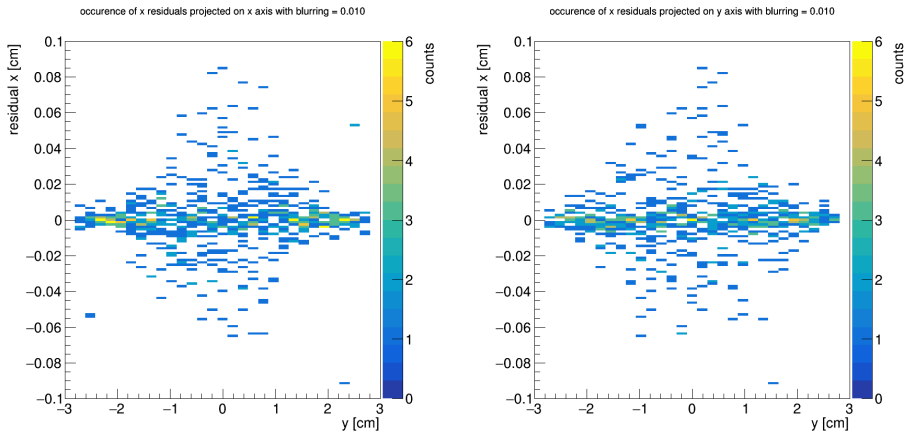


Figure 4.17: A histogram of occurrences of residuals, projected to the x axis on the left, and to the y axis on the right with a smearing value of $\sigma = 0.01$.

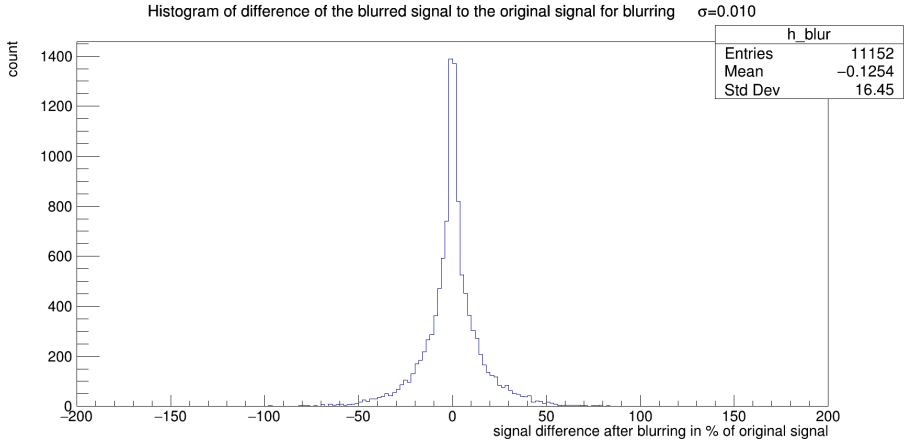


Figure 4.18: The difference in signal after smearing in percentage values of the original signal for $\sigma = 0.01$.

and therefore might be more viable in real scenarios where detectors can exhibit high signal fluctuations. The weighted charge method can also underestimate the particle position due to linearity of the weighted charge model. Additionally, the detectors have to be very well calibrated so that the reconstructed positions are not biased towards one of the detectors, and the method seems to work well only up to a certain noise level.

In the end, this model of the detector was not used in the final experiment setup as the time sensitivity and other properties of this detector design were considered to be insufficient for the experiment purposes. As such the method to reconstruct the position was not applied to data.

4.1.3 Squared tile detector design

Next was the design made of a 7 x 7 cm^2 scintillator tile with a total of 4 PMTs attached. This design was used in the T1 and T0 detectors, as shown in the WCTE detector setup in Figure 2.1. This detector is using the same scintillator material as the previous TOF design.

As the detector is very similar to the previous design, i was able to use the same

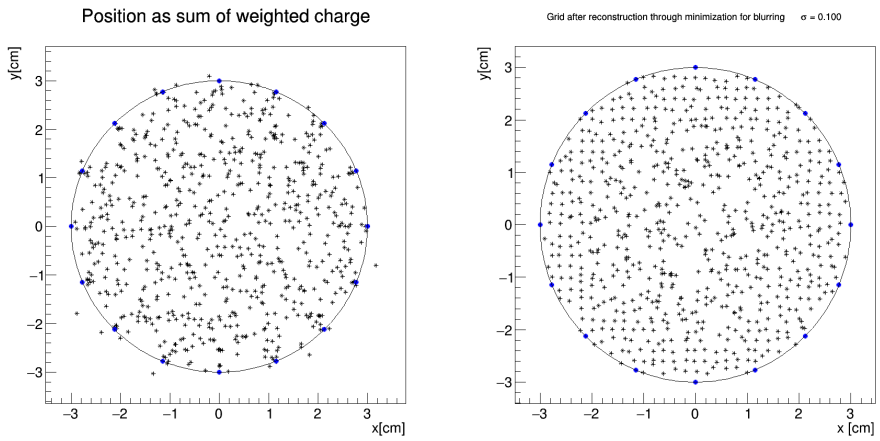


Figure 4.19: A histogram of position reconstruction comparing weighted charge method on the left with minimization algorithm on the right, with a signal smearing with $\sigma = 0.1$.

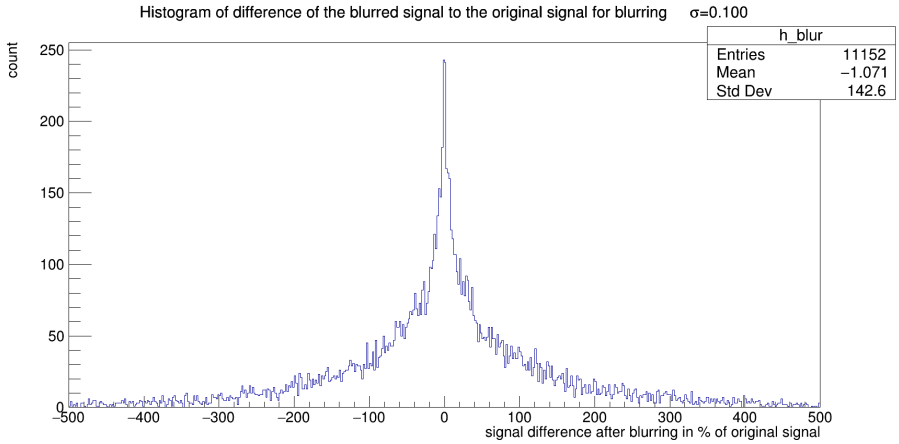


Figure 4.20: The difference in signal after smearing in percentage values of the original signal for $\sigma = 0.1$.

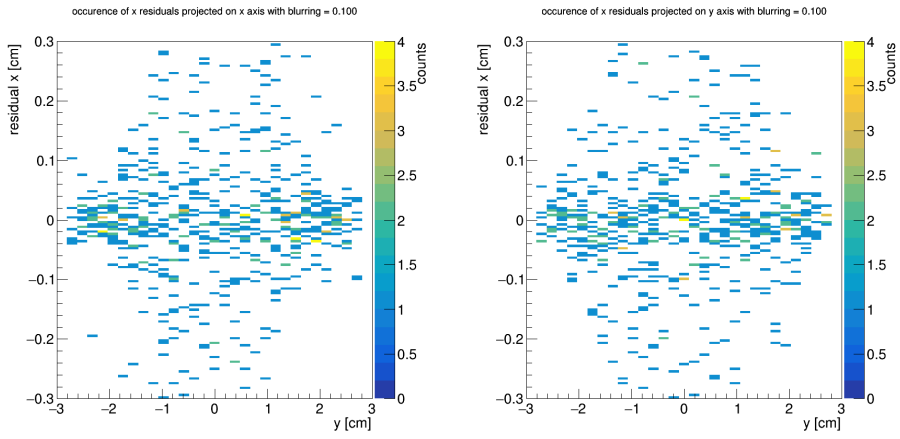


Figure 4.21: A histogram of occurrences of residuals, projected to the x axis on the left, and to the y axis on the right after smearing the signal with the value of $\sigma = 0.1$.

methods to test the simulated response and the following reconstruction. Similarly to

the round time-of-flight detector simulation, I simulated different particle positions by creating a grid of particles and generated the signal in the individual detectors using the Equation (4.8). The response in the individual detectors can be therefore expected to be very similar to responses shown in Figure 4.9. Then I used the minimization algorithm Minuit2 to minimize the χ^2 as defined Equation (4.9), where the signal values Q_i^{meas} were the simulated values and $Q_i^{\text{theoretical}}$ was the model used to generate the responses, to reconstruct the primary positions. This resulted in Figure 4.22, where it can be seen that the algorithm fails for areas that are near the PMTs, but shows good reconstruction in the rest of the detector volume. This was compared to the weighed charge reconstruction, which is shown in Figure 4.23. As can be expected, since the detector does not have any top nor bottom side PMTs, the vertical position from weighed charge is compressed, which might limit the position measurement capabilities of the weighed charge method.

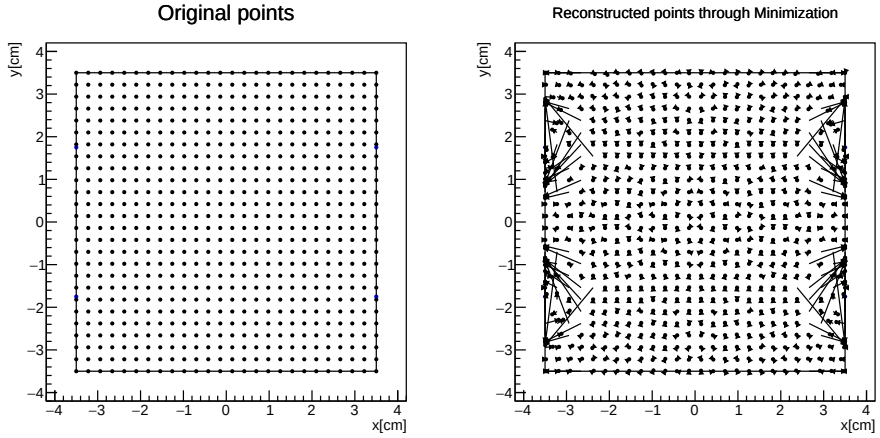


Figure 4.22: Grid of simulated primary points on the left, reconstructed particle positions through the χ^2 minimization using Minuit2 on the right, with the arrows showing how the reconstruction moved the particles from their original positions.

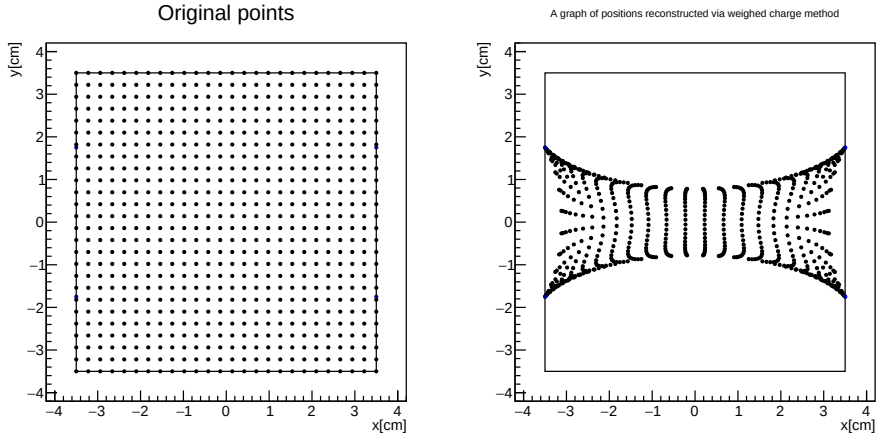


Figure 4.23: Grid of simulated primary points on the left, reconstructed particle positions through multiplying the PMT position vectors by the charge of the PMTs and divided by the total charge on the right.

As the minimization showed good results, I tried to apply it to data from the 2025 run, choosing a run at 270 MeV/c beam momentum. When I applied the reconstruc-

tion in its base state, it resulted in all of the reconstructed events being near one of the detectors This was due to the absolute values of the charges gained from the theoretical model being on a lower order of magnitude then the real signal values. The reconstruction therefore found the lowest χ^2 value in the position, where the theoretical signal matched at least one of the measured charges, which was the position right next to a photodetector. To correct this effect, I scaled the theoretical charge by an amplitude A, so that the theoretical values would be on the same order of magnitude as the measured values. The theoretical signal is then calculated by

$$Q_i = A \, \frac{1}{r^2} \, \exp\left(-\frac{r}{\lambda}\right) \, . \tag{4.11}$$

By choosing a different amplitude, the reconstruction capabilities of the minimization algorithm change considerably. As the model has asymptotic behavior near the detectors, the theoretical charge value close to the detectors approaches infinity, which real detectors will never detect, as they saturate at a certain point. This decreases the precision of the used model, and decreases the reconstruction accuracy of the minimization method.

To get realistic amplitude value, I tried to fit the points to the modified model, but the obtained results showed no stable fit value of the amplitude. I also considered, that since the detectors are identical, all the points should use the same amplitude value, and it should not vary event-by-event. An approximate value of the amplitude was therefore set ad hoc to $A = 15000$, since higher amplitude values caused all points to be reconstructed in the middle of the detector, and with lower values the points shift towards the detectors, creating secondary maxima, which is not expected, as the beam profile should be Gaussian and centered approximately in the middle of the detector. With this amplitude value, a good result was reconstructed and is shown in Figure 4.24. In the same Figure, there is also a comparison with the weighted charge reconstruction method, which shows results that correspond to the simulation, being more squeezed in the vertical axis.

While the result of the reconstruction was worse than expected, it seems that the model used corresponds better to reality than the weighed charge reconstruction. A better result might be acquired by modifying the model to account for the photomultiplier saturation effect, but then it would have to be configured to reflect the detector used and therefore would require measuring the detector at the operational voltage and current beforehand.

Another method I tried involved comparing the relative fractions of the total charge. I changed the minimization to compare what percentage of the total charge was collected by the photodetector. The theoretical values were recalculated similarly. This enables the reconstruction without tuning the amplitude, though it still suffers from not taking into account detector saturation. The result is cleaner than the previous method, and is shown in Figure 4.25. Better results might only be achieved by correcting the used model.

4.1.4 Segmented time of flight detector design

The last design that was simulated was the main TOF detector that was used in 2025 and was set inside the water tank entry pipe. It is made out of 8 scintillator blocks separated by light reflecting tape so that there is no cross-talk between the scintillators and each block can therefore be read out separately. On each end of the blocks there is an attached SiPM, so each block is read out by 2 photomultipliers.

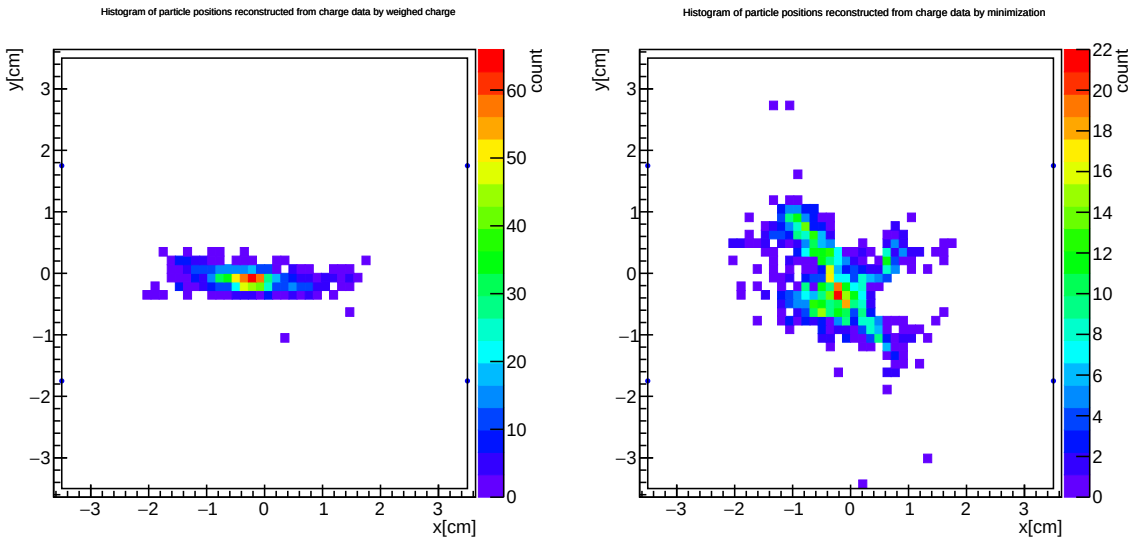


Figure 4.24: A histogram of reconstruction of particle position in the T1 detector using data from a run with beam momentum set to 270 MeV/c. The left histogram shows the weighed charge method to reconstruct the position from data, the right histogram shows the positions reconstructed by a minimizing χ^2 using minimization algorithm Minuit2.

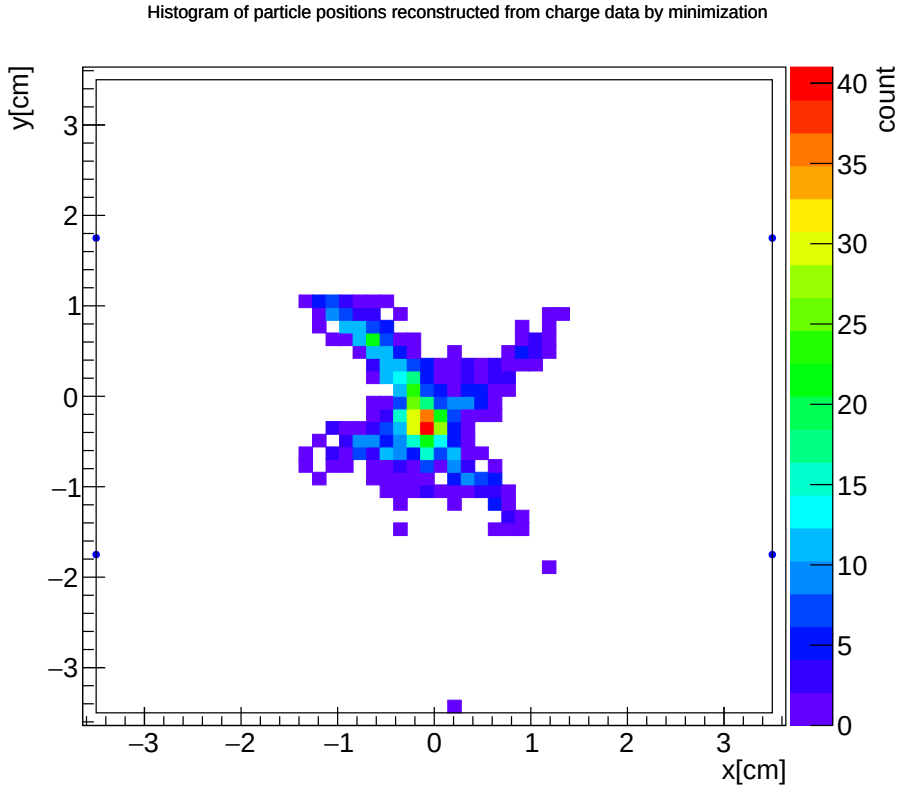


Figure 4.25: A histogram of reconstruction of particle position in T1 detector using data from a run with beam momentum set to 270 MeV/c. The histogram shows the positions reconstructed by χ^2 minimization, using the fractions of the total charge as opposed to the absolute charge value.

To generate the response I used the Equation (4.8) as in the previous simulations to generate the signal in the SiPMs. As this detector has only 2 photomultipliers, the 2D reconstruction of the vertical position is not viable, and as such all reconstruction is only considered in one dimension. Repeating the procedure the same way as in the T0 and T1 detector simulation resulted in reconstructed positions as shown in Figure 4.26. Here it can be seen that using the Minuit2 minimization algorithm, the resulting reconstructed positions tend to clump together in the center or on the sides, with the area between them empty, even though the hits are generated uniformly.

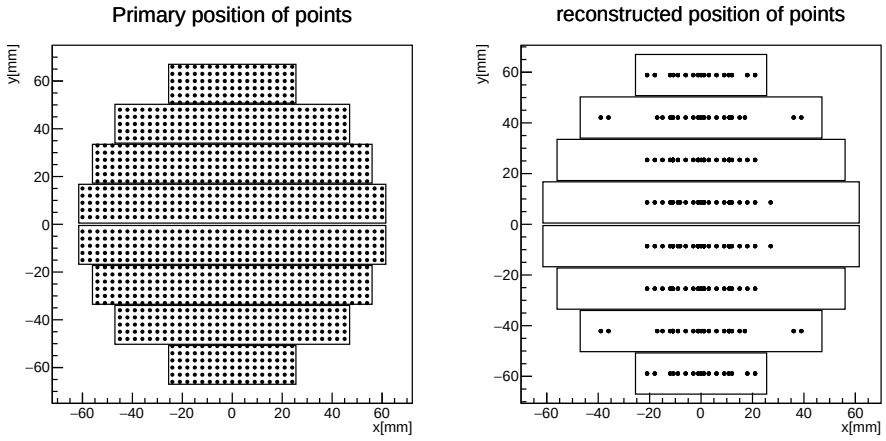


Figure 4.26: A graph showing the primary positions of the simulated particles on the left and the reconstruction of their coordinates in the segmented TOF detector using the Minuit2 minimizer on the right.

As Minuit2 did not provide a satisfactory result, I decided to create my own minimization algorithm. In this algorithm, I checked the χ^2 value for a starting point, which I set to be the position gotten from the weighted charge using Equation (4.2). Then, I moved the position by a fixed step value toward the detector with the higher charge and repeat the χ^2 calculation. If the value in that position was higher than previously, I reversed the direction in which the position would be moved and decrease the step size. All of this was in a while loop, which continued until the χ^2 value was smaller than a given tolerance level, or until a certain number of iterations was reached. Using this custom numerical minimization gave much better results, resulting in reconstruction shown in Figure 4.27

I also compared the results to the weighted charge method, which resulted in the reconstructed points mostly being concentrated in the middle of the scintillator strip. This is shown in Figure 4.28. Due to not showing good results, I focused on applying the custom minimizer to the data.

I applied both methods to the data taken by the experiment in 2025 and compared the results. The run the reconstruction was applied to had the beam momentum set to 270 MeV/c. Using the approach developed when analyzing the data from the T1 detector, I compared the fractions of the total charges instead of the absolute values. The comparison is shown in Figure 4.29. Both methods did not end up showing an expected beam profile, since the run energy is low enough that due to particles multiple scattering on air and other detectors the beam profile should cover the whole detector. It can also be seen that some SiPMs have a higher gain than others, causing the response to be very biased to the SiPM with the higher gain.

Unexpectedly, the minimization method had a narrower profile width for all scintil-

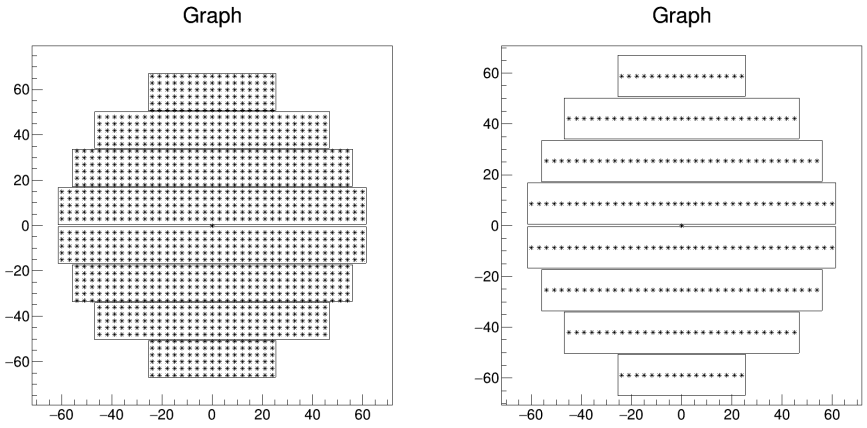


Figure 4.27: A reconstruction of particle positions using the custom χ^2 minimizer.

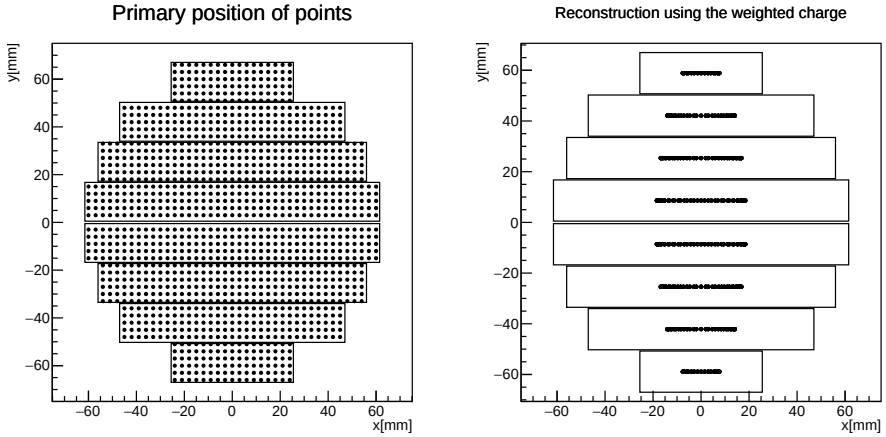


Figure 4.28: A reconstruction of the grid of points in the segmented TOF detector using the weighted charge method from Equation (4.2).

lators than the weighted charge method. The reason for this might be that the model used in the χ^2 minimization does not take into account the reflection of photons on the reflective foil, in which the scintillators are wrapped in. This would cause the $1/r^2$ term in Equation (4.8) to be suppressed. As a test, after correcting this term to the $1/|\boldsymbol{r}|^{0.5}$ dependence, to take into account that part of the photons will be absorbed instead of reflecting into the detector. Some dependence on the distance of the particle from the detector should still be present, since there is a higher chance for the photon to be absorbed by the foil. After this correction, the minimization method showed more realistic results than the weighed charge method. The resulting histogram is shown in Figure 4.30, where the beam profile is wider and therefore closer to reality, but still heavily influenced by the different gain in some photosensors.

By investigating further, a more precise result might be achieved. If the beam profile is known and well centered, the detectors with the biased position could be corrected by centering the mean charge difference between the opposite detectors. While usable, this model still has several shortcomings that might reduce its precisions.

In conclusion, the weighted charge method provides a good first estimate of the particle position, though it typically tends to underestimate the actual profile width. A profile that better matches real measurements can be acquired by minimizing the χ^2

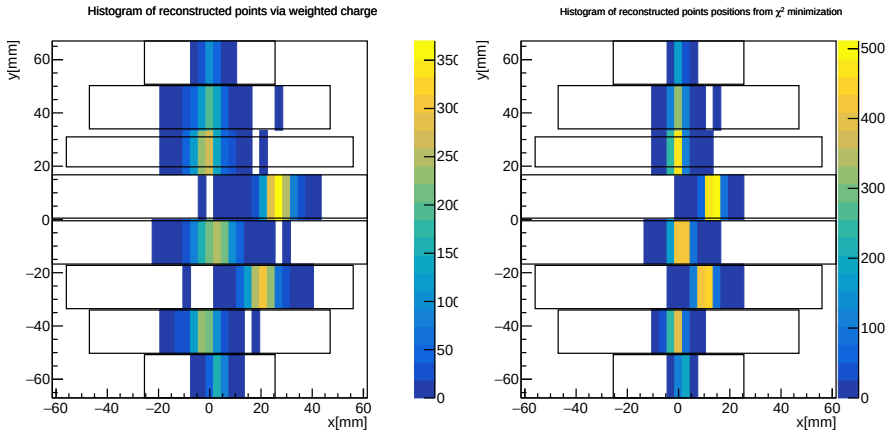


Figure 4.29: Histograms showing the particle position reconstruction from real data by weighing the detector positions by the charge measured on the left, and by minimizing the model on the right. The data was taken in run 1375 which had a beam momentum of 270 MeV/c.

of a proper model. By further suppressing the radial term, a satisfactory model might be achieved, which might be used in position reconstruction.

To increase the model precision, a number of facts needs to be considered. The model needs to take into account the saturation of the detector, as above a certain charge, the photomultiplier signal will not increase, which was not included in the model. Another increase in the model precision can be done by modifying it with distinct values for different particles, as each particle type might produce a different number of photons by ionization and therefore increase the detector response. The model also cannot take into account impurities and imperfections in the scintillators themselves, which might be corrected by the calibration of the PMTs. Further improvements might be reached by factoring in the effective detector area, and not using a point like detector.

In the case of the scintillator strips, which were wrapped in a reflective tape, photon reflection also should be taken into account. This is a non-trivial task, as with each reflection a photon can be absorbed, and different photon flight angles have a different number of reflections. While suppressing the radial factor $1/r^2$ to a lower power can lead to reasonable results as a proxy solution, a more complex simulation based on Geant4 or other simulation applications might achieve better results.

In the end, this method of particle position reconstruction was put aside in favor of using the time data from the detectors to get the approximate particle positions, as the SiPMs have a sub-nanosecond resolution which was considered sufficient for getting a good approximation of the primary position when taking into account the dimensions of the scintillator blocks used. The analysis of the time data in the TOF detector is more closely described in Section 5.1.

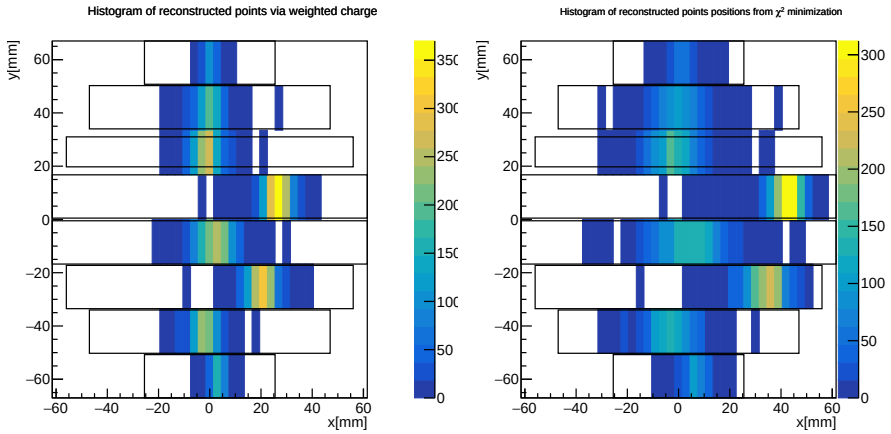


Figure 4.30: Comparison of the particle position reconstruction through weighing the detector positions by the measured charge on the left with reconstruction by minimizing the χ^2 of the corrected model with suppressed radial term on the right. The data was taken in run 1375 which had a beam momentum of 270 MeV/c

4.2 Simulation of cosmic rays inside the main detector using the official WCSim simulation package

Cosmic rays are high energy particles from outer space that enter our atmosphere. They create a shower of secondary particles, which can be then detected either above the atmosphere in satellites, on Earth's surface, or even below the surface in underground detectors [53]. As the primary particle energies can be large, a many secondary particles are created by interactions with the air. These particles range from more massive particles like neutrons and protons, down to almost massless neutrinos. Measurement of the flux of different particle types as a function of atmospheric depth can be seen in Figure 4.31. As can be seen in the graph, the most populous particles that manage to reach ground level are muons. For that reason, when simulating different particles at the sea level, the overwhelming majority of these will be muons.

The second main contribution to the experiment was improving the official WCSim package by adding the option to simulate cosmic rays. There was already a cosmic simulation in the package that was used for the Super Kamiokande experiment, but this simulation was using cosmic muon energies and fluxes corresponding to the underground placement of the Super Kamiokande experiment.

Since the WCTE experiment is not situated underground, the first part of the task was to create a proper data file with which cosmic muons at the sea level could be simulated. This would be then used for the WCTE experiment to approximate the cosmic background, or to study the viability of using low energy cosmic muons for detector calibration.

4.2.1 About the WCSim simulation package, cosmic ray simulation (and data structure)

Water Cherenkov simulation package WCSim [54] is the official software for water Cherenkov detector simulations. The app is based on Geant4 [55] and ROOT packages,

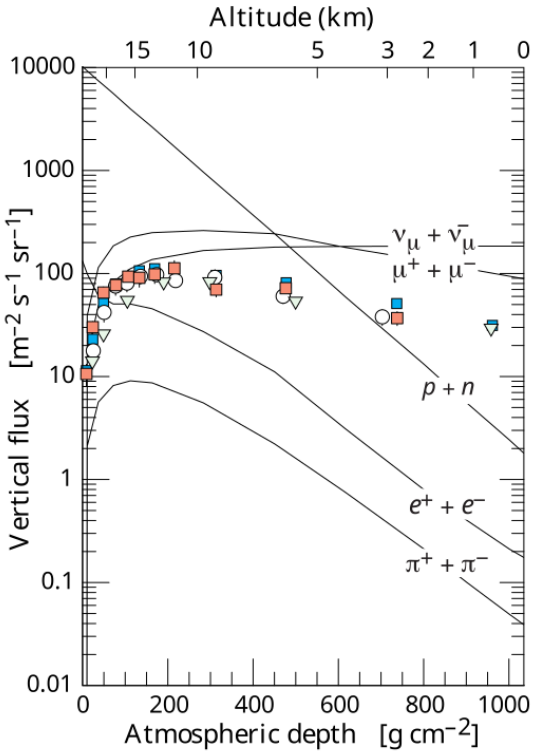


Figure 4.31: Fluxes of different particles in cosmic showers caused by cosmic rays at different atmospheric depth. Lines are showing theoretical prediction for different particles, points show measurements of cosmic muns with higher than 1 GeV energies. Taken from [53].

and as such is written in C++. It is a flexible framework that automatically places PMTs according to the configuration file sourced when running the application. This allows for multiple detector configurations. The default configuration is the Super Kamiokande detector, but there are also configuration files for Hyper Kamiokande, IWCD and WCTE detectors.

To build the application, one needs to have ROOT 6.26.04 or similar version, and Geant4 version 4.10.3.3 installed for it to run properly. It also uses the HepMC3 [56] version 3.2.6, which is a tool for saving and manipulating events in Monte Carlo simulations, for proper functionality. After installing the prerequisites, the program is built using CMake according to the instructions listed on the GitHub page of the software. As the application is based on Geant4, running the application is similar. It is usually ran in batch mode, using defined macros that can be changed to simulate different particles and particle sources. After simulation, the data is automatically saved into a ROOT file that can be then used for analysis.

The program simulates particles according to the instructions inside the source file named `WCSimPrimaryGeneratorAction.cc`, where the application defines possible simulation modes. The cosmic ray simulation part of this file is shown in Listing 4.1. In this code snippet, it can be seen that in order to create a primary particle position and direction, it creates a histogram of particle fluxes and energies. It then uses these histograms to randomly sample the positions and a direction according to the data in the histogram, and also sets a corresponding energy to the direction the particle comes from.

```
    else if (useCosmics) {

    if (hFluxCosmics == nullptr)
      Create_cosmics_histogram();
// get muon direction
    double phiMuon, cosThetaMuon;
    energy = 0;
    while((int)(energy) == 0){
      hFluxCosmics->GetRandom2(phiMuon,cosThetaMuon);
      int phiMuonBin = hFluxCosmics->GetXaxis()->FindFixBin(phiMuon);
      int cosThetaMuonBin = hFluxCosmics->GetYaxis()->FindFixBin(
   cosThetaMuon);
      energy = hEmeanCosmics->GetBinContent(phiMuonBin,cosThetaMuonBin
   )*GeV;
    }

    G4ThreeVector dir(0,0,0);
    dir.setRThetaPhi(-1,acos(cosThetaMuon),phiMuon);
```

Listing 4.1: Code snippet of WCSim particle generation source code for cosmic rays.

In order to use the cosmic generator, I have to include two lines listed in Listing 4.2. The first line in this macro gives the program the command to use the cosmic generator, and the second line guides it to the data file it should use to create the appropriate particle generation histogram.

```
/mygen/generator cosmics
/mygen/cosmicsfile data/WCTE_cosmics.dat
```

Listing 4.2: Code snippet of WCSim startup macro.

After the listed set up, to run the simulation the correct Geant4, ROOT and WCSim versions have to be sourced. The simulation can be launched in the terminal by typing the command in Listing 4.3, where the first macro sourced has the commands for the

particle generation, and the second macro sets the parameters of the detectors inside the simulation.

```
WCSim macros/start_macro.mac macros/tuning_parameters.mac
```

Listing 4.3: Command to start WCSim simulation.

For proper analysis of the simulated data, it is important to understand the data structure, in which the data is saved. The data is saved into ROOT trees. There are in total three trees in the data file, the first is `WCSimRootOpt` tree, in which options of the simulation are saved, and as such is not too important for data analysis. The second tree `WCSimRootGeom` is much more important, since the detector geometry is saved there inside the `wcsimrootgeom` branch. The branch itself has methods that output different detector parameters. There are many methods, but the most useful ones are the following:

- `GetWCCylRadius()` – lists the radius of the detector;
- `GetWCCylLength()` – outputs the detector height;
- `GetWCNumPMT()` – lists out the total number of PMTs used in the simulation;
- `GetPMT(i)` – this loads an individual PMT by its ID number, and more info about this PMT can be obtained by using methods:
  - `GetTubeNo()` – outputs the PMT ID number;
  - `GetCylLoc()` – shows, where on the detector the PMT is, outputs 0 for the PMTs situated on the top cap, 1 for the walls of the detector and 2 for the detector bottom cap;
  - `GetPosition(i)` – gives x, y and z coordinates of the PMT with arguments 0, 1 and 2 respectively.

The data itself is stored in the `WCSimRootEvent` tree. This tree has branches:

- `wcsimrootevent` – main data saved from the detectors inside the barrel, of main interest to us;
- `wcsimrootevent_OD` – data from the outer detector - not useful for WCTE simulation, since it has no outer detector.

Inside the `wcsimrootevent`, all particle events are saved. There is always at least one entry in this tree, and the number of entries should correspond to the number of particles that were simulated. Every secondary particle produced is saved as its own separate track in the data, where the primary particle is always the first trigger. Some important methods to read out the data are as follows:

- `GetTrigger(i)` – returns an object `WCSimTrigger`, where subevents of the simulation particle are stored, the main event is always the first subevent, necessary to always load it, as all other data is saved under it and can be accessed using methods:
  - `GetNTracks()` – returns number of tracks inside the subevent;

- `GetTracks()` – returns a pointer to array of tracks, you can then access individual tracks by applying method `At(i)`, where i is the track number. In this object all track information is saved, including track start and end positions, energies when crossing boundaries which can be used to calculate particle energies lost in the detector, particle directions and so on (a very useful tool for visualization);
- `GetNCherenkovHits()` – returns the number of Cherenkov hits in PMTs;
- `GetCherenkovHits()` – returns a pointer to an array holding true hit information, including hit PMT ID in the detectors. Individual hits are accessed by using method `At(i)`;
- `GetCherenkovHitTime()` – returns a pointer to an array of time information for all Cherenkov true hits, also including all Cherenkov photons start and end position, and its creation processes;
- `GetCherenkovDigiHits()` – returns a pointer to an array of digitized hits, i.e. true hits and simulation of electronics dark noise, including the information about digitized charge, time, and which PMT was hit.

These are all objects useful for a basic analysis. There are of course more objects and methods, but those are for more specialized studies beyond the scope of this cosmic ray simulation.

4.2.2 Sea level cosmic muon models

As described in the previous subsection, to have a cosmic ray simulation, a data file with muon energies and fluxes has to be provided to the application. As the WCTE experiment is not located underground, the surrounding geology does not influence the muon energies and fluxes, so the appropriate data can be approximated from sea level cosmic muon fluxes.

To create a usable data file, I had to research different cosmic ray models, and determine which one is best suited for our purpose. First thing to consider was the total muon flux. According to several articles [53, 57, 58] it is widely considered that the overall muon flux is proportional to [53]

$$\Phi_\mu \propto \cos^2\theta \ , \tag{4.12}$$

where θ is the polar angle of the incoming muon measured from the zenith. There has been no evidence suggesting, that the muon flux is significantly dependent on azimuthal angle [59], so I consider no dependency on it. Using this flux with an appropriate cosmic muon model, it is possible to get a good approximation of average muon energy in dependence on angle. It is important to choose a single right model, as several different exist.

The first model is called the Gaisser model as described in his book [60]. This model is based on kaon and pion two body decays, and approximates muon flux as

$$\frac{\mathrm{d}N_\mu}{\mathrm{d}E_\mu} \approx \frac{0.14E_\mu^{-2.7}}{\mathrm{cm}^2\ \mathrm{s\ sr\ GeV}} \left\{ \frac{1}{1+\frac{1.1E_\mu\cos\theta}{115\ \mathrm{GeV}}} + \frac{0.054}{1+\frac{1.1E_\mu\cos\theta}{850\ \mathrm{GeV}}} \right\} \ . \tag{4.13}$$

While a good approximation formula, it is only valid for muon energies $E_\mu > \frac{100}{\cos\theta}$ and incident angles $\theta < 70°$, since it neglects the Earth curvature. As such, it vastly overestimates low energy muon flux, and as such is not appropriate for this simulation.

Next model is a Gaisser-Tang model. This model is a modification of the Gaisser model by Tang [61] and increases the precision of the model for low muon energies, and also takes into account higher angles. To do that, it modifies the original Formula (4.13) into the following form:

$$\frac{\mathrm{d}N_\mu}{\mathrm{d}E_\mu} \approx A \frac{0.14 E_\mu^{-2.7}}{\mathrm{cm}^2 \text{ s sr GeV}} \left\{ \frac{1}{1 + \frac{1.1 \widetilde{E}_\mu \cos\theta^*}{115 \text{ GeV}}} + \frac{0.054}{1 + \frac{1.1 \widetilde{E}_\mu \cos\theta^*}{850 \text{ GeV}}} + r_c \right\} . \tag{4.14}$$

In this modified equation, Tang makes several adjustments to the original approximation, so that it better corresponds to the experimental data, and as such is more phenomenological. It does that by first adding the constant

$$r_c = 10^{-4} , \tag{4.15}$$

and it also corrects the muon energy to

$$\widetilde{E}_\mu = E_\mu + \Delta , \tag{4.16}$$

where E_μ is the Earth surface muon energy, $\widetilde{E}_\mu$ is the energy of the muon in the top of the atmosphere and Δ is the correction to the energy loss of the muon in the atmosphere; Δ can be calculated as

$$\Delta = 2.06 \times 10^{-3} \left(\frac{950}{\cos\theta^*} - 90 \right) \text{ GeV} . \tag{4.17}$$

The constant A is the scale factor, and is equal to

$$A = 1.1 \left(\frac{90\sqrt{\cos\theta + 0.001}}{1030} \right)^{4.5/(E_\mu \cos\theta^*)} . \tag{4.18}$$

The most important part of the Tang model is parametrizing the $\cos\theta^*$ as

$$\cos\theta^* = \sqrt{\frac{x^2 + p_1^2 + p_2 x^{p_3} + p_4 x^{p_5}}{1 + p_1^2 + p_2 + p_4}} , \tag{4.19}$$

where x is $\cos\theta$, $p_1 = 0.102573$, $p_2 = -0.068287$, $p_3 = 0.958633$, $p_4 = 0.0407253$ and $p_5 = 0.817285$ are fit parameters. Due to all these changes, the model corresponds quite well to experimental measurements even for low energies.

Next cosmic muon model was proposed by Bugaev [62]. This is a purely phenomenological model that aims to fit a curve to collected data for vertical cosmic muon flux. Bugaev managed to deduce that the relation between the vertical muon flux and energy can be described by the following fitting model

$$\Phi_\mu(p, \theta = 0) = C \; p^{-(\gamma_0 + \gamma_1 \log p + \gamma_2 \log^2 p + \gamma_3 \log^3 p)} , \tag{4.20}$$

where p is the muon momentum, and γ_0,γ_1,γ_2,γ_3 and C are the fit parameters.

As the Bugaev model is purely for vertical muon flux, it is not viable for general muon flux approximation. To fix this, Reyna [63] changed this model to take account for flux changes in dependence on the zenith angle. He found, that if a dependence on cosine is added to the Bugaev model, the result matches experimental data very well. That resulted in the following model

$$I(p_\mu, \theta) = \cos^3(\theta) I_v(\zeta) . \tag{4.21}$$

In this model, $\zeta = p_\mu \cos(\theta)$, which means that the vertical flux from Equation (4.20) is in the following form:

$$I_v(p_\mu \cos\theta) = c_1 p^{-(c_2 + c_3 \log(p_\mu \cos\theta) + c_4 \log^2(p_\mu \cos\theta) + c_5 \log^3(p_\mu \cos\theta))} \ . \tag{4.22}$$

By fitting the angle dependent flux to data, Reyna determined fitting constants to be $c_1 = 0.00253$, $c_2 = 0.2455$, $c_3 = 1.288$, $c_4 = -0.2555$ and $c_5 = 0.0209$. As it was fitted to available data, this model is valid for muon momenta 1 GeV $< p_\mu <$ 2000/ cos θ GeV

The last model that can be considered is the Smith-Dullerd-Chatzidakis model. This phenomenological model originally developed by Smith and Dullerd for muon tomography has been later modified by Chatzidakis [64] to serve as a Monte Carlo generator. This model assumes that all ground level cosmic muons come from pion decays in the atmosphere and disregards the kaon contribution. From that, the following muon intensity I_μ at sea level is produced

$$I_\mu(E_\pi,\theta) = \frac{A E_\pi^{-\gamma} P_\mu \lambda_\pi b j_\pi}{E_\pi \cos\theta + b j_\pi} \ , \tag{4.23}$$

where E_π is the energy of the pion, that produces the muon, A and γ are fitting constants, P_μ is the probability that the muon reaches the ground level, λ_π is the pion absorption mean free path, b is a correction factor and $j_\pi = (m_\pi y_0 c)/(\tau_0 \rho_0)$ is a constant containing atmospheric depth, atmospheric density, pion mass, pion mean lifetime and the speed of light. To use this model, the muon energy has to be approximated as a fraction of pion energy, and as the model contains many constants, it is hard to use easily. It has been fitted to experimental data, which resulted in getting values for fitting constants $A = 0.02382$ and $\gamma = 2.645$, and as such is useful for generating muon energies from 1 to 100 GeV.

The previously mentioned models have been compared in a paper by Ning et. al. [58] The comparison of the models can be seen in Figure 4.32 that compares the models in terms of goodness of fit to the experimental data, where the best model is the Chatzidakis model, followed closely by the Reyna model. Due to being easy to implement and not being much worse in quality, I decided to use the Reyna model to generate the cosmic muons.

4.2.3 Sea level cosmic muon fluxes and energies

In order to implement the cosmic muon model into the WCSim package, due to the method of generation described in Subsection 4.2.1, I had to first generate the flux dependent on the zenith and azimuthal angles. Using equation (4.12), I generated muon flux dependence on θ in arbitrary units. As mentioned in previous subsections, to generate the muon, the azimuthal incoming angle needs to also be considered, and since there is no surrounding geology, the dependence on polar angle can be assumed to be uniform. Together, this results in a histogram as seen in Figure 4.33.

After that, I used equations (4.21) and (4.22) to numerically calculate the energy spectrum for different angles. I checked how the energy spectrum changes with different angles, the comparison can be seen in Figure 4.34.

By changing the scale to non-logarithmic, I tried to find the energy, where the flux is the largest. This can be seen in Figure 4.35, where the maximum flux for vertical muons is around 1 GeV for vertical flux, while for higher angles it shifts towards the higher energies.

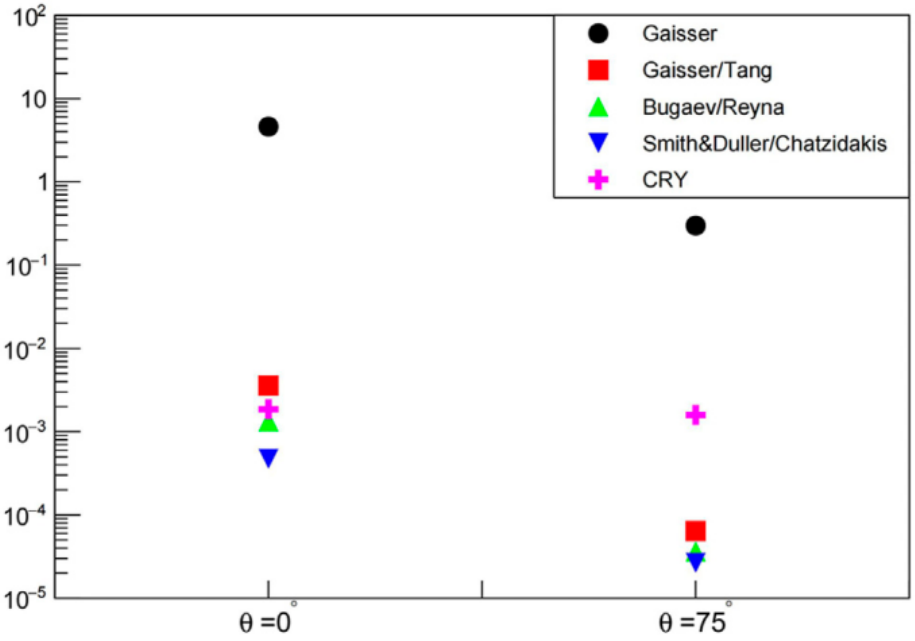


Figure 4.32: Cosmic muon model comparison in terms of the goodness of fit χ^2 of the different models to experimental data for two zenith angles, taken from [58].

Since the WCSim cosmic simulation simulates cosmic muons using the average energy, I had to calculate the different mean energies for each angle that will be used. Mean energy can be retrieved by using

$$E_{\text{mean}} = \frac{\int_0^\infty E\ f(E)\ \mathrm{d}E}{\int_0^\infty f(E)\ \mathrm{d}E}\ , \tag{4.24}$$

where $f(E)$ is the Reyna model energy distribution. By doing that, I got the mean energy for vertical muons

$$E_{\text{mean}}(\theta = 0^\circ) = 4.87\ \text{GeV}\ . \tag{4.25}$$

I repeated that for all angles, and created a histogram of mean energies shown in Figure 4.36. From this histogram I created a data file, that would serve as an input for the WCSim application.

4.2.4 Analysis of the cosmic muon simulated data from WCSim

I used the created data file to simulate a set of 1000 cosmic muons. This set has been used to check the viability of the cosmic muon simulation in WCSim.

The first thing I plotted using the data was an event display of a single event to visualize the simulation. By modifying a code a collaboration member made, I got the event display as shown in Figure 4.37. In this figure, I plot the charge collected on individual PMTs based on PMT position in the tank. That can be then used to see the Cherenkov rings of different particles. The red star is the entry point of the particle, white star is the exit point. As can be seen, there are more PMT hits centered on the exit point of the cosmic muon, with PMTs outside the Cherenkov cone having only occasional hits, probably from reflected light or dark noise.

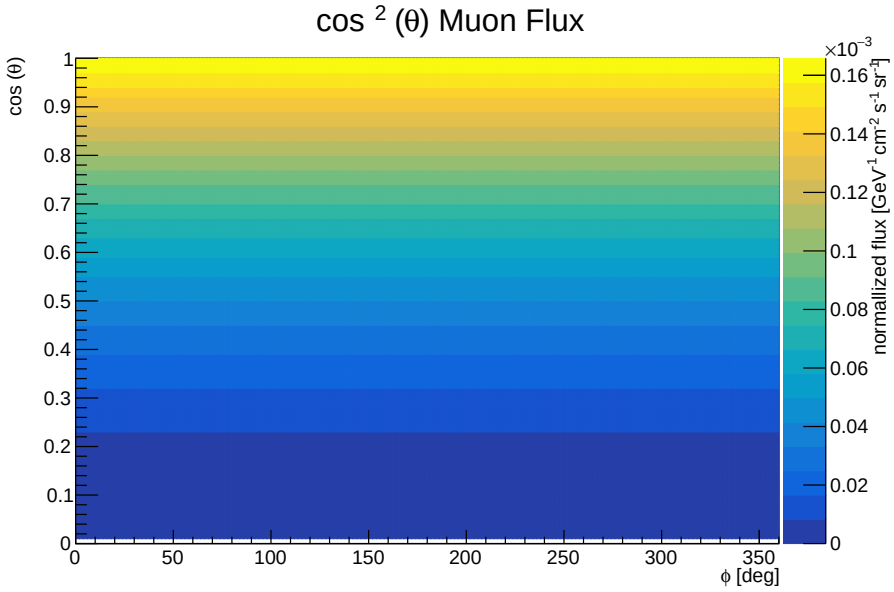


Figure 4.33: Cosmic muon flux dependence on angle as implemented by the $\cos^2(\theta)$ dependence for zenith angle and uniform distribution for the azimuthal angle.

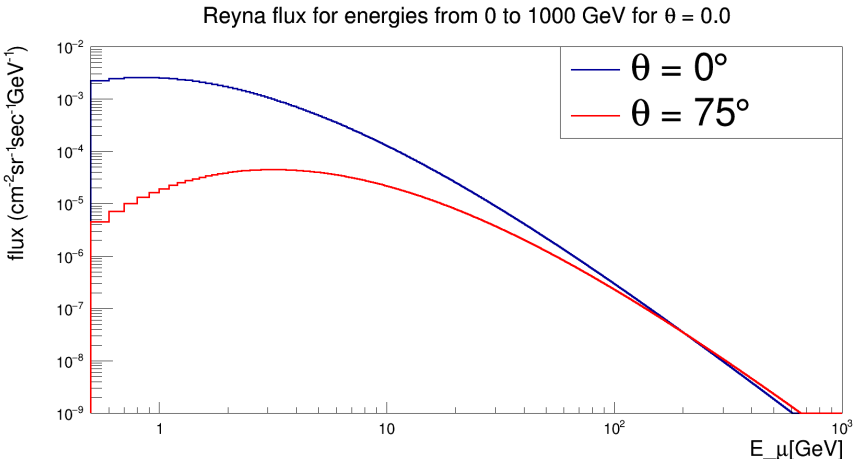


Figure 4.34: Comparison of cosmic muon fluxes from the Reyna model for $\theta = 0$ and $\theta = 75°$.

When plotting the event display of all 1000 events together, charges in individual PMTs are as shown in Figure 4.38. This confirms that most muons come from the right direction, i.e. from the top, as the Cherenkov light is mostly hitting the bottom cap and the lower half of the barrel. It can also be noticed that when the PMTs are rotated away from the vertical direction or the center of the bottom cap, less charge is collected, which indicates they have a smaller efficiency of light detection due to the light reflecting off because of the higher incident angle of the photons to the PMT optical gel surface. This results in colder spots on the outside ring of the bottom cap detectors, and at the bottom of the barrel walls.

To further validate the model, I plotted the incident angle of the muons. This can be seen in Figure 4.39, where it was surprising to see no hits in $\theta = 0°$, since the input file is defined, so that the most probable muons are vertical ones, as shown in Figure 4.33. To check for that, I looked at a histogram of muon hits versus the zenith angles. This is shown in Figure 4.40, where most hits entered the detector at an angle

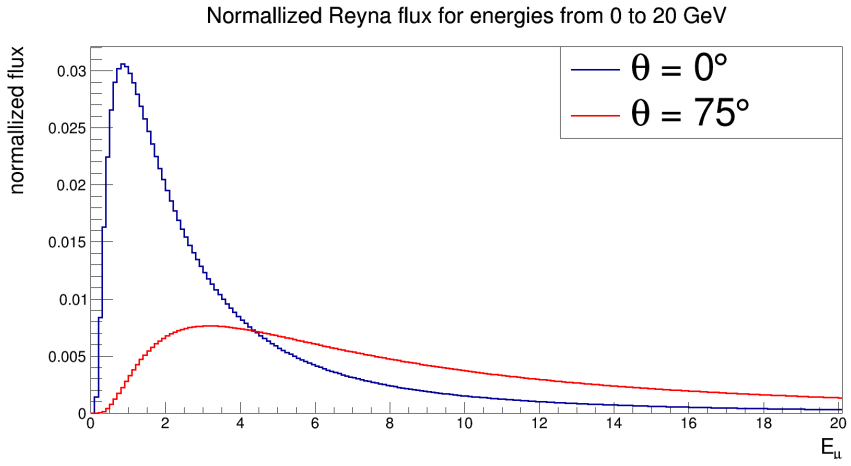


Figure 4.35: Zoomed in maximum flux for angles $\theta = 0°$ (blue) and $\theta = 75°$ (red), with the histograms normallized to compare maximum values.

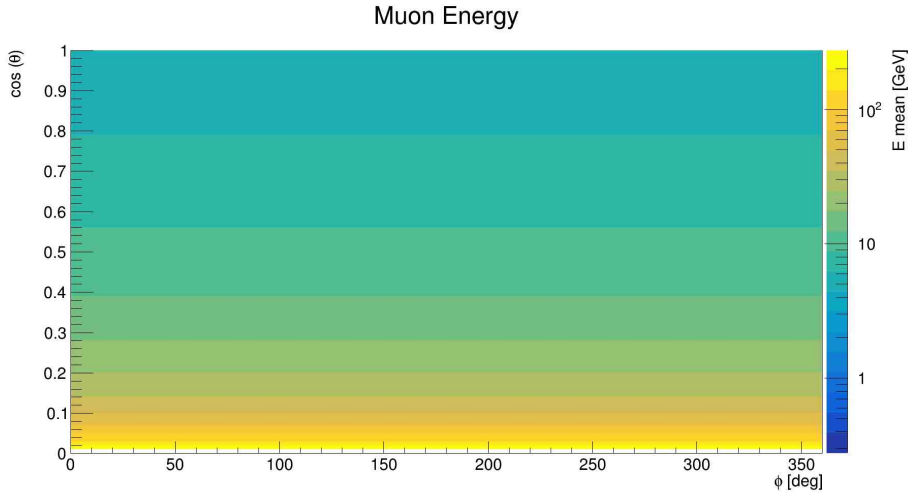


Figure 4.36: Mean energy histogram for different θ and ϕ.

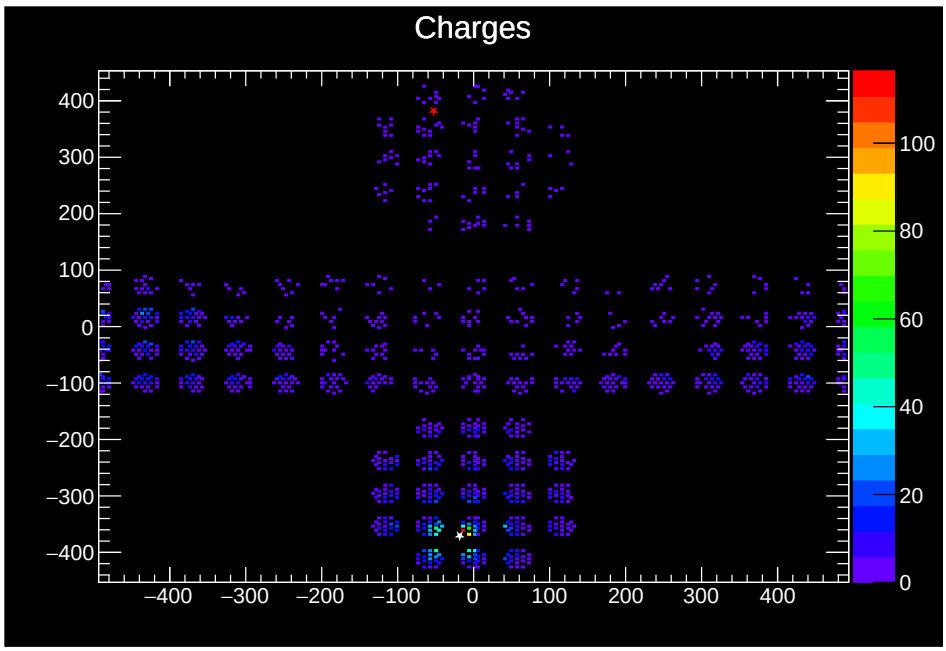


Figure 4.37: Event display of a single simulated cosmic muon entering the water tank in WCSim.

$\theta \approx 0.6$ rad. After checking with literature, I found out, that this is due to the so-called solid angle effect, where the flux of the muons hitting the detector is scaled by $\sin(\theta)$. The dependence of flux is then proportional to

$$I_\mu \propto \sin\theta \cos^2\theta \ , \tag{4.26}$$

which corresponds to the histogram in Figure 4.40.

After this was clear, I took a look at entry and exit points in the detector. Since in the simulation the muons are created outside of the detector and have a set energy and direction, they can also enter the detector from different sides. The entry and exit points of the muons are shown in Figure 4.41, where it can be seen that while most muons enter through the top cap, there is also a considerable number of events that enter through the wall of the detector. The same is true for exit points. This was done by propagating the initial vertex in the direction of the momentum, and saved the moments where it crossed the detector boundary.

Next step was to look at muon energies when they enter and exit the detector. As mentioned, the muon is generated outside of the detector, and needs to reach the detector first. During this, it can lose some energy, or even stop if the energy is low enough. It is also important to note, that only the energies of the particle at the moment of their creation are saved, and next they are saved only when they cross a certain boundary in the detector-either the boundary between the inner detector and dead space, an mPMT or the tyvek between the detector and outer space. When checking the boundary crossings, it was noticed, that some muons enter through one boundary type and exit through another. This means I could not filter the entry/exit energies through the boundary type. For that reason, to get the entry and exit energies, I considered only those boundary crossings between which the muon traveled for at least 1 ns. Due to this filtering, muons which stopped inside the detector or which only went through a small part of it are excluded. Thanks to that, I got histograms shown in Figure 4.42. By comparing the entry and exit energies, I also managed to get

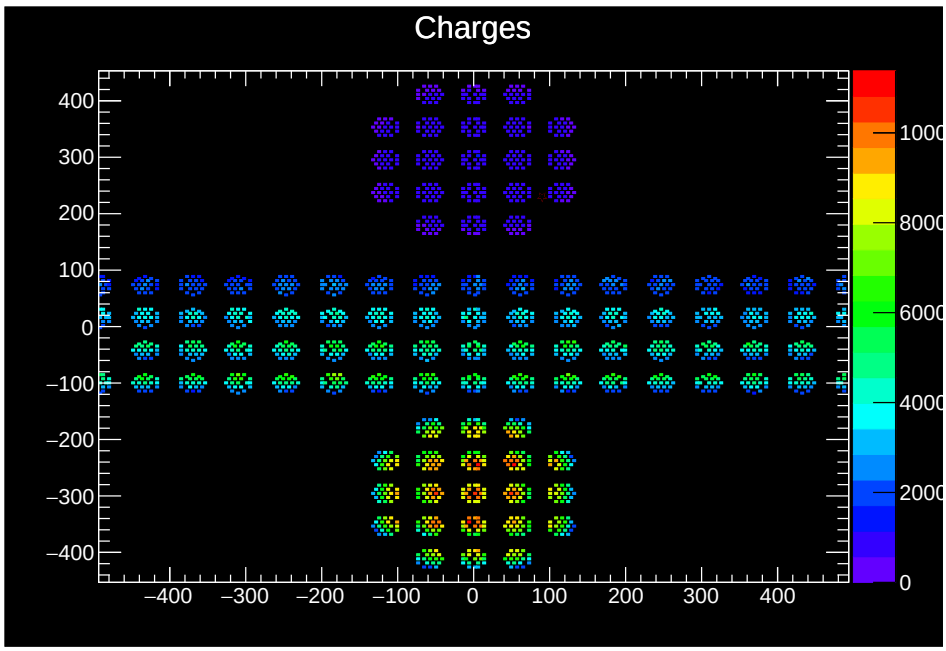


Figure 4.38: Event display of all 1000 simulated cosmic muon events.

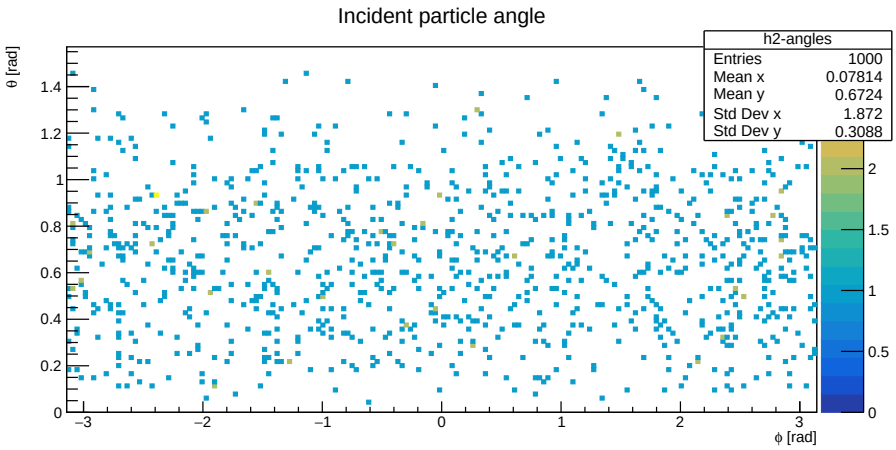


Figure 4.39: Incident angle θ and ϕ of incoming cosmic muons in WCSim.

the muon energy lost in the detector. That is shown in Figure 4.43. From the last histogram, It is clear that the muons usually lose around 0.5 GeV while going through the water Cherenkov detector. That, together with the fact, that in the sea level cosmic muon models, the mode of the energy distribution is usually around 1 GeV for vertical directions, motivated me to try another simulation with lower primary energies by modifying the entry data file.

To see how the cosmic muon simulation behaves for lower muon energies, I modified the generative data file to generate muons of lower energies – five times smaller than the original energies – and reran the simulation. Then I compared the output histograms, trying to look for muon decay that might be seen in the water Cherenkov detector. In principle, finding the μ^- decay events is possible, because the simulation also saves the creation processes of all particles that are created in the simulation. The decay events can then by chosen by applying cuts on the creation process of the particle, and when combined with the track end points of the simulated muons, one can further narrow that down to only such events that decayed inside the detector volume. From

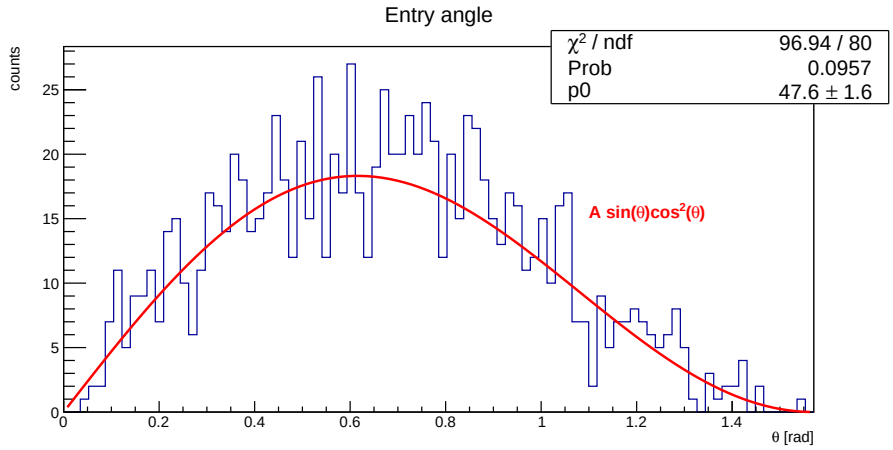


Figure 4.40: Polar angle θ of incident cosmic muons in WCSim, fitted by Equation (4.26).

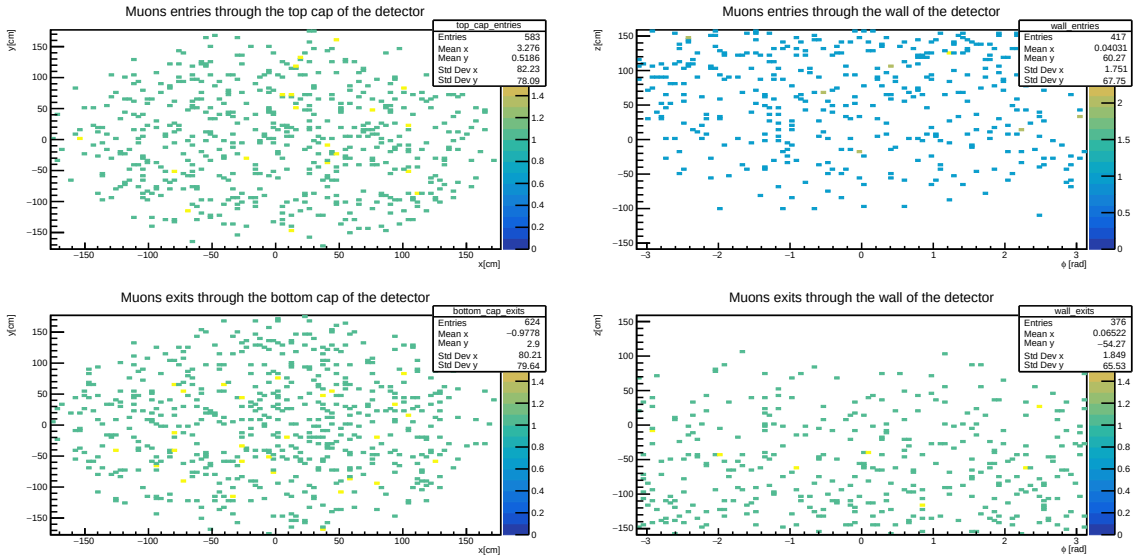


Figure 4.41: Entry and exit points of simulated cosmic muons in the WCSim simulation.

one thousand events, only three decayed inside the detector volume, and only one of these produced a visible Cherenkov track, which can be seen in Figure 4.44.

By adding up the decay products energies, the muon decays happened with the muon energy around 0.5 GeV. I tried to decrease the energy of the generated muons slightly more to around 400 MeV, but at these energies the muons usually did not even reach the detector, and if there were any decays outside the detector, they were not saved.

To further validate the simulation, I checked whether there is a correlation between a muon primary energy and the total charge detected by the PMTs, by plotting the total measured charge in the detector as a function of the primary muon energy. This histogram is in Figure 4.45. There seems to be a slight correlation between higher muon energy and the total charge measured by the detector, though this can be explained by the higher zenith angle of the higher energy muons. I also compared this with the data that was simulated at lower energies, which showed very similar values and increase with energy, and is shown in Figure 4.46.

To conclude my work on simulations in WCSim, a model was created for cosmic

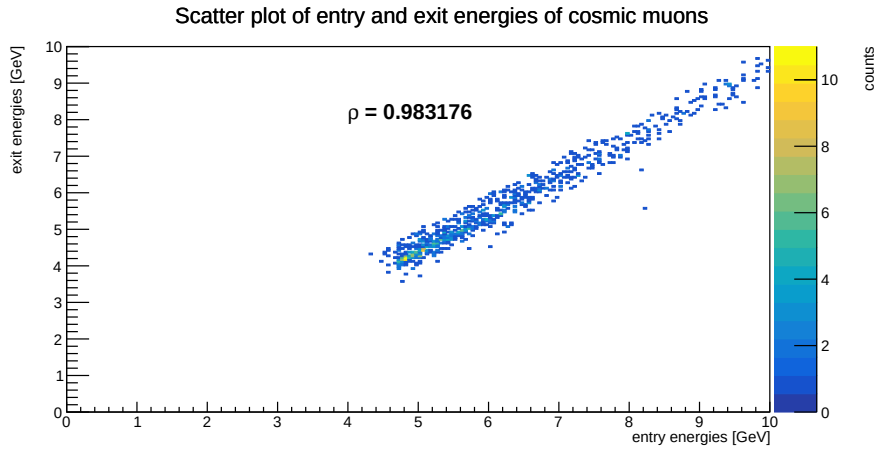


Figure 4.42: Scatter plot of simulated muon entry energies and exit energies after traveling through the detector in the WCSim simulation.

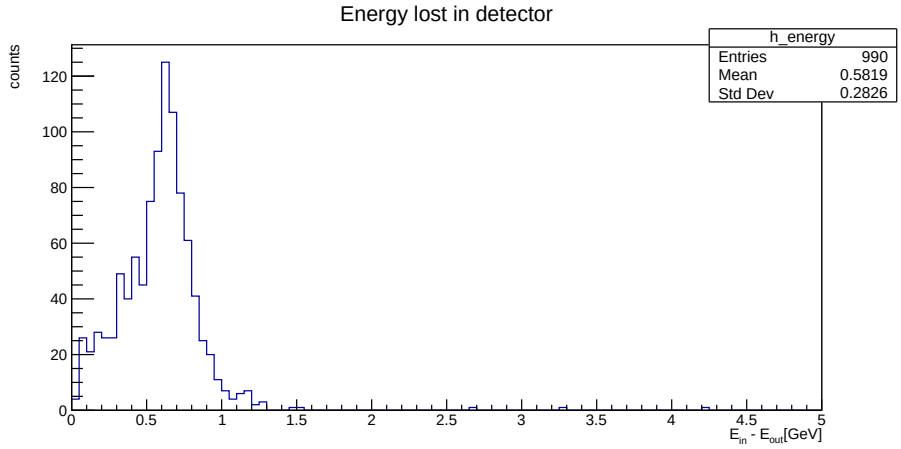


Figure 4.43: Energy lost by the simulated cosmic muons in the detector in the WCSim simulation.

muon simulations in water Cherenkov surface detectors. This model was presented at collaboration meetings. It has been committed to the main repository on Git, and is now usable by other collaboration members. The simulation package is not suitable for simulating low energy muons, since they stop in the volume outside the main detector due to the simulated world being filled with water. A few muon decays were observed, but due to limitations in computing power, only a small number of these events could be simulated. Further analysis might enable a distinction of these events from others, which might contribute to the calibration of the detectors. A disadvantage of the simulation is, that it only uses negative muons as part of the cosmic showers, even though positive muons are also included in reality. This can be changed in the source code, but requires a recompilation of the project. The complete code that was used for the analysis of the simulated data can be accessed at [65].

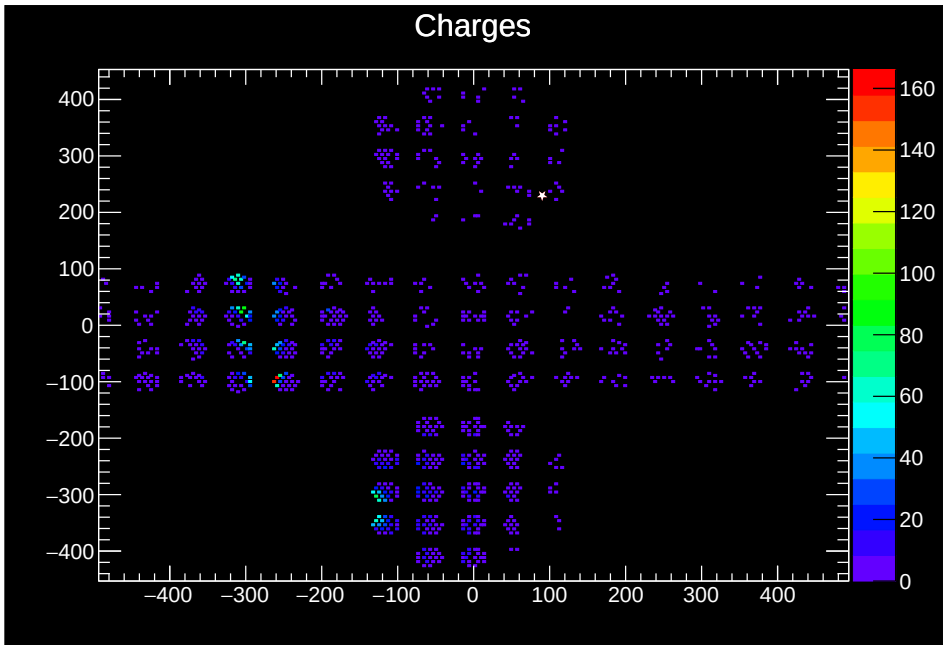


Figure 4.44: Event display of a single simulated low energy cosmic muon, which decayed inside the main detector volume.

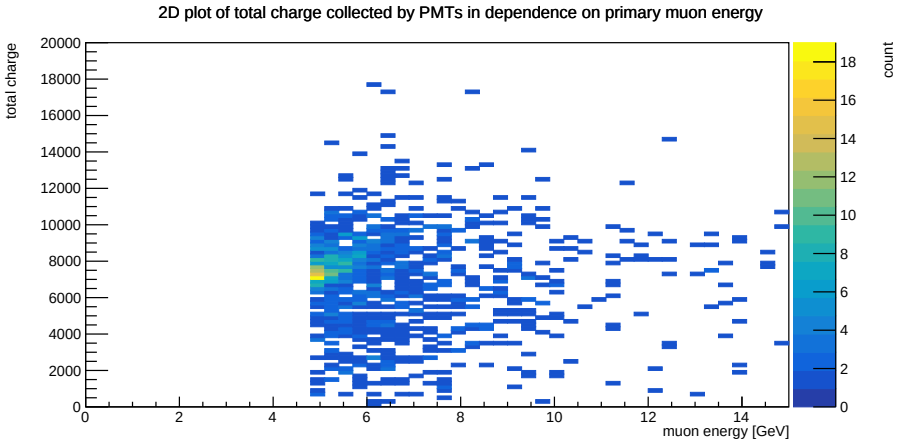


Figure 4.45: A histogram showing the charge collected by the PMTs for cosmic muon events simulated by WCSim, for muon with energies higher than 4.8 GeV.

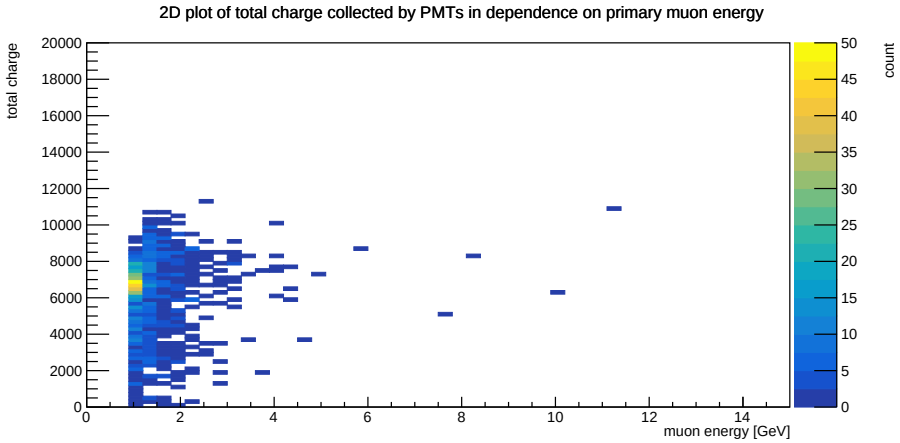


Figure 4.46: A histogram showing the charge collected by the PMTs for cosmic muon events simulated by WCSim, for muon with energies higher than 0.8 GeV.

Chapter 5

Analysis of the WCTE experiment 2025 data

Besides working on simulations described in the previous chapter, I also took part in analyzing the WCTE data taken in the 2025 run. As I was already familiar with the TOF detector through the position reconstruction simulation and cosmic muon testing, I also volunteered to analyze the TOF detector data and tried to reconstruct the particle positions using the timing data taken. This approximate particle position reconstruction on the event-by-event basis would then be useful to calibrate the detector responses in the WCTE tank to different particles. The complete code that was used for the TOF detector analysis can be accessed at [49].

5.1 Particle position reconstruction using the time data from 2025 run

The TOF detector has two detectors for each scintillator strip. The first cut that had to be done in order to start the analysis was to apply a cut on the data to only choose events, that had a pair of opposite detectors hit, and work further with these events. The number of pairs hit per event can be seen in Figure 5.1, where it is also visible, that some events event had two, and up to three hits, that might be either caused by pile-up or by a delta electron produced by ionization.

At the same time, many events had no pairs hit in the detector, which means that either the signal did not propagate to both sides of the scintillator strip, that the particle hit the dead space in between the scintillator strips, or that the particle scattered on the other detectors and air, diverging too far out of the beamline to hit the detector itself. In this run with beam momentum on 200 MeV/c, the event ratio of no hits to 1 hit is

$$\frac{N_1}{N_0} = \frac{1048}{5493} \approx 1.91 \ , \tag{5.1}$$

which means that almost one in two events is rejected.

Due to the previously mentioned causes, it can be inferred that the number of events where no pairs will be hit will decrease with the beam energy, which was confirmed when looking at the same histogram for higher energy, which can be seen for beam momentum 550 MeV/c in Figure 5.2, with the ration of no hits to 1 hit decreasing to

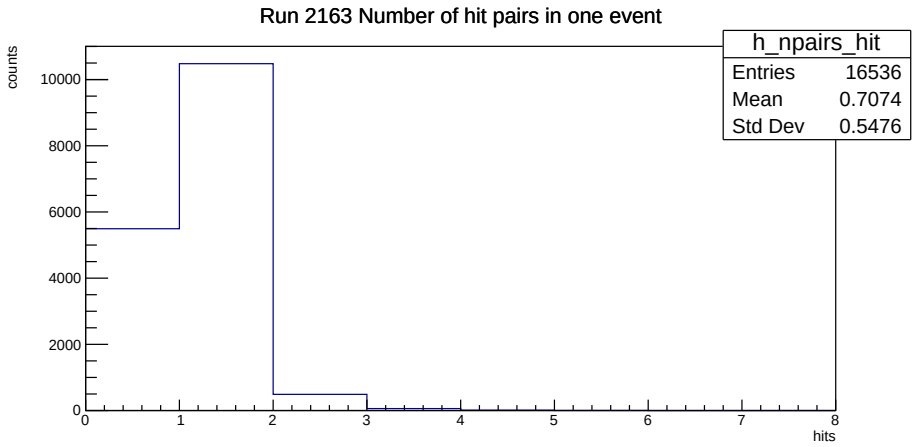


Figure 5.1: A histogram of the number of pairs hit in an event for a run with beam momentum of 200 MeV/c.

$$\frac{N_1}{N_0} = \frac{452799}{161467} \approx 2.80 \ . \tag{5.2}$$

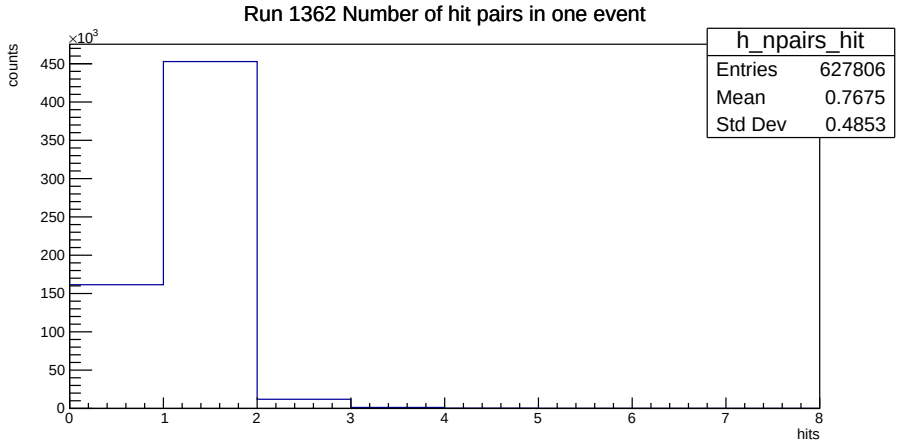


Figure 5.2: A histogram of the number of pairs hit in an event for a run with beam momentum of 550 MeV/c.

The first thing that had to be done to check the detector response was to get the timing resolution of the opposite detectors. This was done by taking the time data for detectors connected to the same scintillator and subtracting their times in each event. By plotting these subtracted values I obtained the histogram in Figure 5.3. What is important to notice in this histogram is that the time resolution for shorter scintillators is generally better than for longer scintillators. This will be used in later analysis.

I also plotted the time of flight between the T0 detector and the TOF detector. An example of this plot can be seen in Figure 5.4, where in the same histogram I always compare detectors that are on the same scintillator. Other than seeing clear areas corresponding to electron, muons and pions (and therefore can serve for particle identification for lower energies), I tried looking for an anticorrelation in each scintillator, i.e. if a particle enters a scintillator strip closer to a SiPM on one side, it would always mean a shorter time than the photosensor on the other side of the scintillator and vice versa. This anticorrelation would mean that the detector resolution is excellent, which

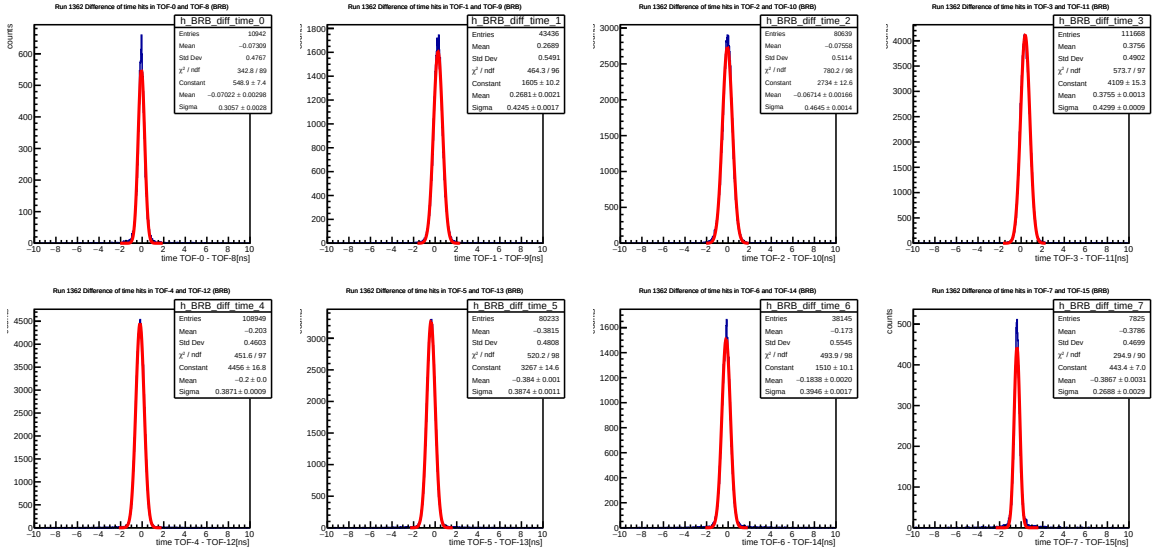


Figure 5.3: Difference in time data of opposite SiPMs on a single scintillator, together with a gaussian fitting for a run with beam momentum of 550 MeV/c. Of note is the standard deviation of different scintillators, with longer scintillators having generally a wider distribution.

would enable clear position reconstruction, since this would mean that the detector resolution is high enough that majority of the total uncertainty is composed of the position variation. Unfortunately, this cannot be seen in this histogram, so the position reconstruction is more complicated.

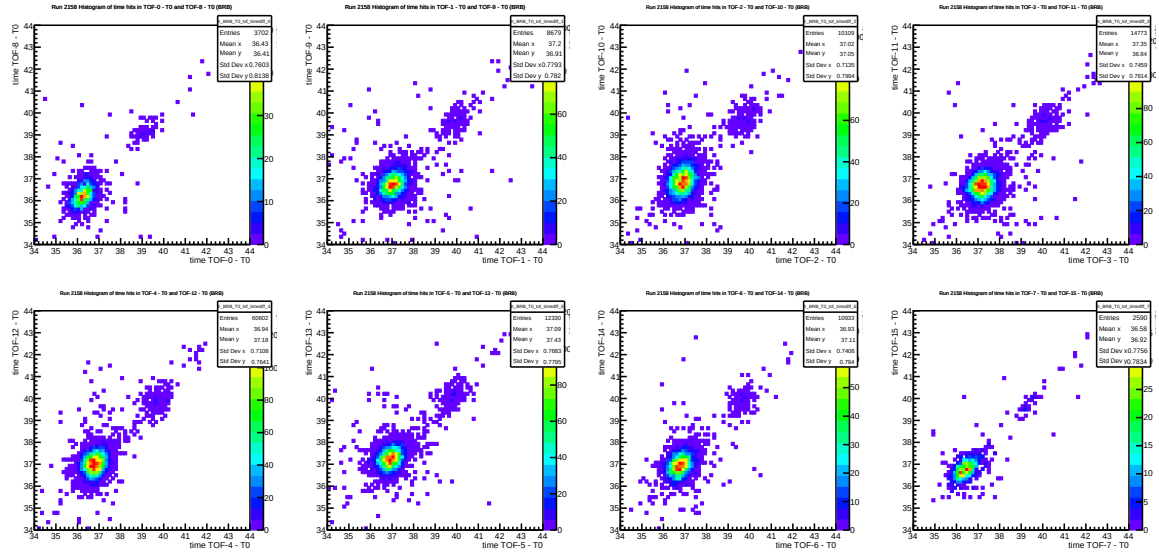


Figure 5.4: 2D histogram of time of flight between the T0 detector and the opposite SiPMs per each scintillator for a run with beam momentum of 200 MeV/c.

Ideally, the particle positions would be obtained by multiplying the speed, with which light propagates through the scintillator, with time data in each detector, and subtracting these values, i.e.

$$x_{\text{pos}} = \frac{c}{n}t_1 - \frac{c}{n}t_2 = \frac{c}{n}(t_1 - t_2) = v_{\text{dir}}\Delta t \ . \tag{5.3}$$

This would only be true for light going straight from particle position to the detector, and the detectors themselves would have to have much smaller time resolution than the scintillator size. More realistically, the light reflecting from the reflective foil, in which they are wrapped, needs to be taken into account, and the detector resolution also needs to be considered. This will result in light propagating through the scintillator with speed

$$v_{\text{eff}} \leq v_{\text{dir}} \ . \tag{5.4}$$

The detector resolution distorts the position reconstruction, combining with the resolution smearing caused by different particle positions and making up the total resolution. This can be written (from uncertainty propagation, assuming that both uncertainties are independent) as

$$\sigma_{\text{tot}} = \sqrt{\sigma^2_{\text{SiPM}} + \sigma^2_{\text{pos}}} \ , \tag{5.5}$$

where $\sigma_{\text{SiPM}} = \sqrt{\sigma^2_{\text{SiPM-L}} + \sigma^2_{\text{SiPM-R}}}$ is the combined time uncertainty in the opposite silicon photomultipliers, and σ_{pos} is the uncertainty caused by the particle hitting different parts of the scintillator and the resulting light propagation. It can be assumed that the opposite SiPMs have the same resolution, which simplifies the calculation and results in

$$\sigma_{\text{SiPM-R}} = \sigma_{\text{SiPM-L}} = \frac{\sigma_{\text{SiPM}}}{\sqrt{2}} \ . \tag{5.6}$$

From the second part of the total resolution, it should be possible to extract the position data. Considering that the beam profile is wide enough, which should be true for lower beam energies due to multiple scattering, in can be assumed that the resulting position distribution is uniform. For such distribution, the resolution is equal to

$$\sigma_{\text{pos}} = \frac{b-a}{\sqrt{12}} \ . \tag{5.7}$$

Taking into account that the time difference in extreme particle positions is

$$\Delta\tau = t_1 - t_2 \ , \tag{5.8}$$

$$\Delta\tau' = t_2 - t_1 = -\Delta\tau \ , \tag{5.9}$$

these extreme values can be plugged into (5.7), which results in

$$\sigma^2_{\text{pos}} = \frac{(\Delta\tau)^2}{3} \ . \tag{5.10}$$

In this equation, $\Delta\tau$ is just the time it takes for the scintillation light to propagate through the full scintillator length. It can be assumed then that the time difference will be equal to

$$\Delta\tau = \frac{d}{v_{\text{eff}}} \ , \tag{5.11}$$

where d is the scintillator length and v_{eff} is the effective light speed that takes into account light reflecting from the scintillator walls.

The result of combining equations (5.5), (5.10) and (5.11) is

$$\frac{d^2}{3v^2_{\text{eff}}} = \sigma^2_{\text{tot}} - \sigma^2_{\text{SiPM}} \ . \tag{5.12}$$

This is very useful, since there are several scintillators with different lengths d_i, and consequently v_{eff} can be acquired by fitting a Gaussian to various data. This fit can be seen in Figure 5.3.

By comparing different scintillators, the effective speed can be obtained as

$$v_{\text{eff}} = \sqrt{\frac{L_1^2 - L_2^2}{3\sigma_{\text{tot1}}^2 - 3\sigma_{\text{tot2}}^2}} \ . \tag{5.13}$$

Using Equation (5.13) I tried to calculate the effective speed by comparing different scintillator sizes. Unfortunately, while some calculated values were viable, ranging from 15 cm/s to 18 cm/s, many values were also unphysically high, either higher than the speed of light in this scintillator, or even higher than speed of light itself, or being an imaginary value. The reason for this can be seen in Figure 5.3, where the fit results of σ_{tot} for different scintillators is shown. As can be seen, the standard deviation value varies wildly between scintillators, not being the same even for the scintillator of the same length, their width often being much smaller than the difference between the deviations themselves. That must mean that there is some variable that increases the resolution for some SiPMs. As a single effective velocity calculation is not usable, it was decided to use a modified method to get the effective velocity.

By using Equation (5.12), a predicted sigma $\sigma_{\text{tot}}^{\text{pred}}$ can be calculated, if the σ_{SiPM} and effective speed are known. To acquire the most probable v_{eff} and σ_{SiPM} values, numerical methods can be used similarly to as written in chapter 4.1.1, utilizing

$$\chi^2 = \sum \left(\frac{\sigma_{\text{pred}}^i - \sigma_{\text{meas}}^i}{\Sigma_{\sigma_{\text{tot}_i}}} \right)^2 \ , \tag{5.14}$$

where σ_{meas} is the total sigma value from fitting to data, and

$$\sigma_{\text{pred}} = \sqrt{\left(\frac{d_i}{\sqrt{3} v_{\text{eff}}} \right)^2 + \sigma_{\text{SiPM}}^2} \tag{5.15}$$

is the predicted value. Using v_{eff} and σ_{SiPM} as variables, I used the Minuit2 [66] minimization package in ROOT to minimize the χ^2, getting the following values

$$v_{\text{eff}} = (264.2 \pm 3.0) \text{ mm/ns} \ , \tag{5.16}$$

$$\sigma_{\text{SiPM}} = (0.319 \pm 0.002) \text{ ns} \ , \tag{5.17}$$

which are still values that are too high. The fit also had a very low fit quality of

$$\chi^2/\text{ndf} = 849.7 \ , \tag{5.18}$$

where ndf is the number of degrees of freedom, and as such the results cannot be considered physically valid.

To correct for imperfections in the different scintillators, that increase the deviation, a coefficient λ_i is introduced into the equation (5.12), that multiplies a fixed $\sigma_{\text{SiPM}} = 0.267$ and as such encompasses other variables that may cause the deviations, like scintillator imperfections, optical gel connection to the SiPMs, differences in the SiPMs and so on. Using this might output more precise values for physics parameters. The problem arises in the fitting, since now there are nine variables - v_{eff} and λ_{0-7}, and

when fitting 8 different scintillators from one run, the number of degrees of freedom ends up being [67]

$$\text{ndf} = N_{\text{data}} - N_{\text{var}} = 8 - 9 = -1 \ , \tag{5.19}$$

which results in overfitting, and thus an invalid fit. To account for this, I extracted the measurements from several different runs, and applied the minimization algorithm to more data points.

I analyzed the data from 15 different runs with beam momenta ranging from 180 MeV/c to 550 MeV/c. After fitting and extracting the time difference widths from the time differences, I reran the minimization algorithm on the larger data sample. The fit converged and resulted in values shown in Table 5.1. The quality of the fit had a value of $\chi^2/\text{ndf.} = 93.35$, which is large, and as such the model does not correspond well to the data. The uncertainties from the fit are in the order of 25 % for the speed, and up to 100 % for the resolution scaling nuisance parameters λ_i. To see if the prediction fits the data I plotted a histogram comparing the predicted value and the data. This can be seen in Figure 5.5. Here, it can be seen that some values diverge from the prediction by much more than their uncertainties, which might be inflating the χ^2. After investigating, these runs seemed to be the higher energy runs. For this reason I ran another analysis, focusing on low momentum runs with beam momenta lesser than 240 MeV/c.

v_{eff} $[\text{cm} \cdot \text{ns}^{-1}]$	(185 ± 38)
λ_0	(1.4 ± 0.1)
λ_1	(1.9 ± 0.5)
λ_2	(1.8 ± 0.7)
λ_3	(1.0 ± 0.8)
λ_4	(0.5 ± 0.8)
λ_5	(0.8 ± 0.7)
λ_6	(1.4 ± 0.5)
λ_7	(0.9 ± 0.1)

Table 5.1: Parameter values from the fit of the width of the SiPM time differences σ_{tot} model to the data from runs with beam momenta from 180 MeV/c to 550 MeV/c.

To check how the σ_{tot} of the data changes with the energy, I plotted the data values from runs with increasing energies. This can be seen in Figure 5.6, where it can be seen, that with higher energies the σ_{tot} values drop considerably, since the beam profile is much narrower at higher energies. This can be seen in the uncertainty of the hits in the shortest scintillators as well, since they get very few hits, and therefore the greatest uncertainty

For the low momentum runs, the result, while still not perfect, had a better fit quality of $\chi^2/\text{ndf} = 7.54$, but the fit uncertainties were much higher, where I got the values shown in Table 5.2. By extrapolating via uncertainty propagation, the total uncertainty of the predicted model was

$$\sigma_{\sigma}^{\text{pred}} = \frac{1}{\sigma_{\text{pred}}} \sqrt{\frac{\sigma_{\text{fixed}}^4}{4} \cdot \sigma_{\lambda_i}^2 + \frac{d_i^4}{9 v_{\text{eff}}^6} \cdot \sigma_{v_{\text{eff}}}^2} \ , \tag{5.20}$$

where $\sigma_{\text{fixed}} = 0.267$ ns is the fixed σ_{SiPM} value, d_i is the length of the scintillator, $\sigma_{v_{\text{eff}}}$ and σ_{λ_i} are the uncertainties from the minimization for effective speed and lambda parameters and $\sigma_{\text{pred}} = \sqrt{\frac{d_i^2}{3 v_{\text{eff}}^2} + \lambda_i \cdot \sigma_{\text{fixed}}^2}$ is the predicted value for the total resolution.

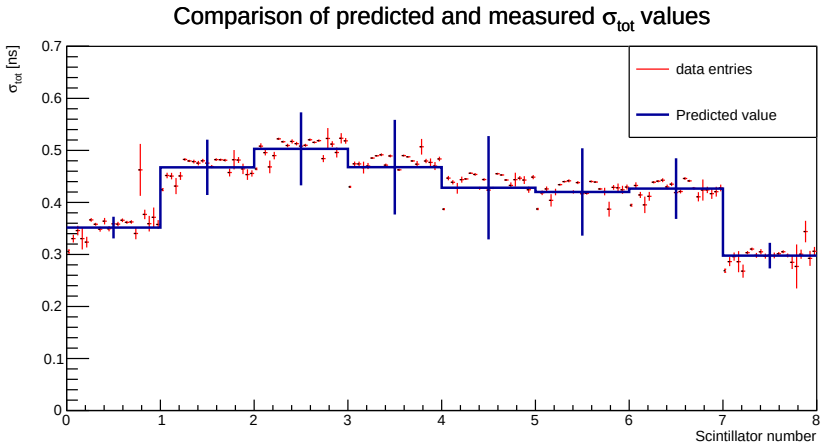


Figure 5.5: Histogram of the width of the opposite SiPM time differences σ_{tot} predicted values compared to the data points from runs at energies ranging from 180 MeV/c to 550 MeV/c.

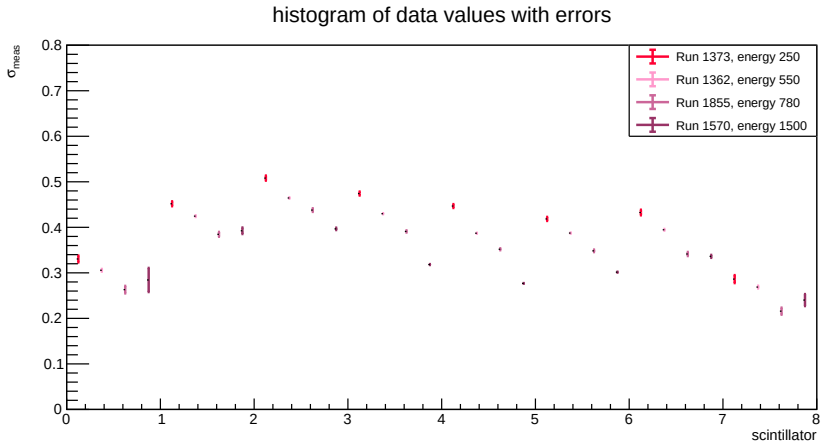


Figure 5.6: The data points of opposite SiPM time difference widths σ_{tot} for runs with rising energies of 250 MeV/c, 550 MeV/c, 780 MeV/c and 1500 MeV/c. The histogram shows a clear decrease in the width of time difference distribution in opposite SiPMs with rising energy due to a narrower beam profile at higher energies.

v_{eff} $[\text{cm} \cdot \text{ns}^{-1}]$	(184.6 ± 68.3)
λ_0	(1.5 ± 0.3)
λ_1	(2.0 ± 0.9)
λ_2	(2.0 ± 1.3)
λ_3	(1.1 ± 1.5)
λ_4	(0.6 ± 1.5)
λ_5	(0.8 ± 1.3)
λ_6	(1.4 ± 0.9)
λ_7	(0.9 ± 0.3)

Table 5.2: Parameter values from the fit of the σ_{tot} model to the data from runs with beam momenta lower than 240 MeV/c.

To check how the prediction fits the data, I created a histogram shown in Figure 5.7.

Here it can be seen that the prediction corresponds to the data quite well, with just a few points deviating.

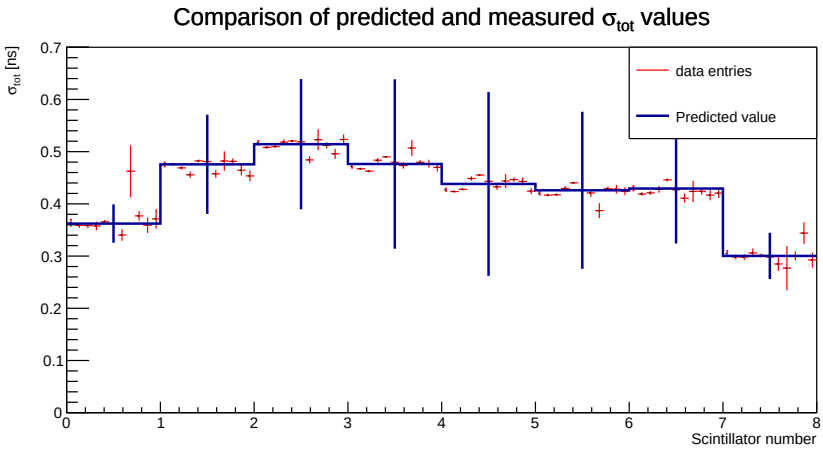


Figure 5.7: Histogram of the σ_{tot} predicted values compared to the data points in runs with energy lower than 250 MeV/c.

I then used these fitted values of v_{eff} to look at the beam profile from the data. The particle position can be derived from the sketch shown in Figure 5.8. When the δ_{detL} and δ_{detR}, which are the time shifts due to the SiPM time detection uncertainty, are considered zero, by subtracting the times in the left and right detectors one get

$$\frac{2z}{v_{\text{eff}}} = t_R - t_L \Rightarrow z = \frac{v_{\text{eff}}\Delta t}{2} \ . \tag{5.21}$$

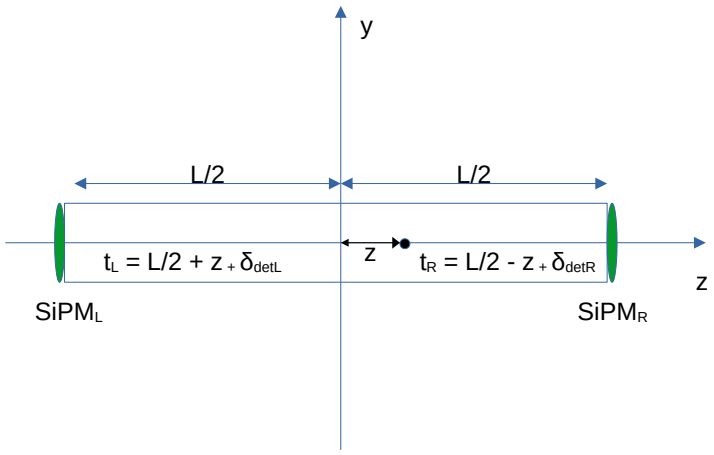


Figure 5.8: Sketch of particle position reconstruction using measured times inside the scintillator strip.

When looking at the data, a bias can be seen as shown in Figure 5.9. The mean time difference is shifted for some scintillators which can be caused either by different cable lengths or by some delay in the electronics readout. The other possibility is that the beam profile is shifted towards one end of the scintillator, thus one detector would be detecting hits earlier.

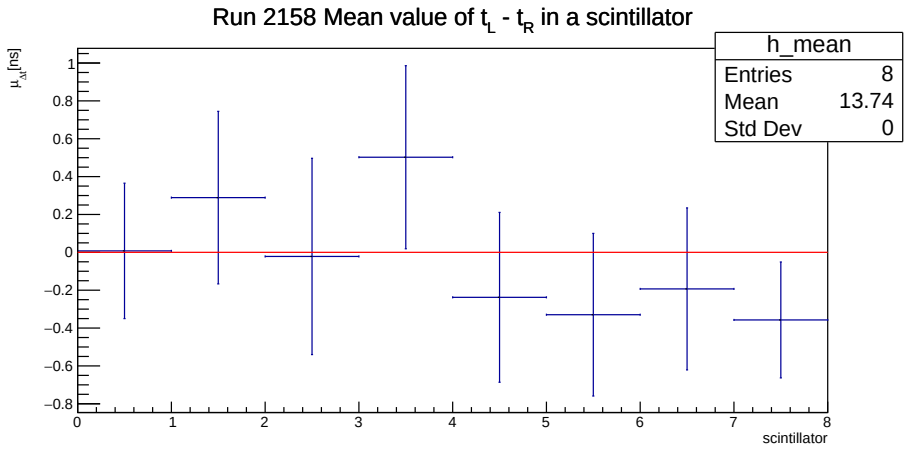


Figure 5.9: Mean values from the opposite SiPM time difference gaussian fit for a run with beam momentum of 200 MeV/c. The uncertainties correspond to the width of the opposite SiPM time difference obtained from the Gaussian fit.

As the beam was tuned during the commissioning so that it was centered on the detector, and the multiple scattering effect for low energies is significant, therefor no structures in the beam profile should be visible, I considered that the bias in the mean value is due to the first two reasons and modified the Equation (5.21) to account for the bias, which results in position coordinate

$$z = \frac{v_{\text{eff}} \cdot (\Delta t - t_{\text{mean}})}{2} \,, \tag{5.22}$$

where t_{mean} is the mean value from the Gaussian fit. After applying this formula to approximate the particle positions, I obtained the histogram in Figure 5.10, which shows the preliminary reconstructed beam profile. While the results are acquired using an effective speed v_{eff} with high uncertainty, they look physical and correspond to how the profile might look like. Some events were reconstructed outside the scintillator strips, which might be caused by the SiPM uncertainty. With further analysis, we hope to get even more precise position reconstruction.

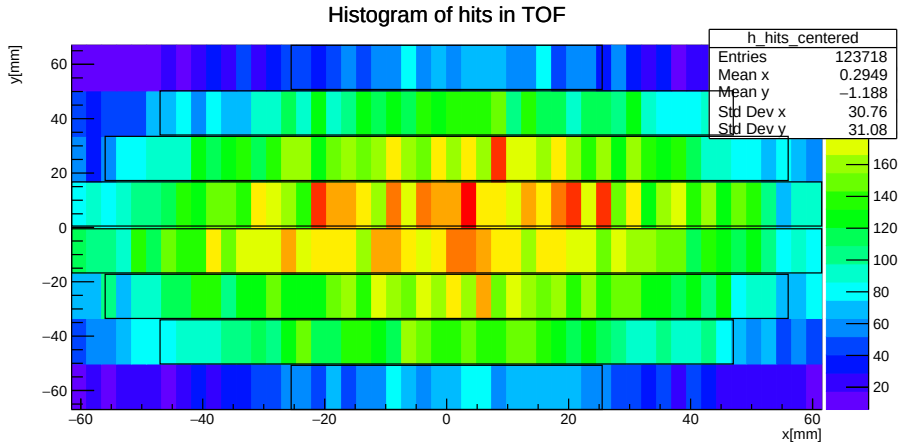


Figure 5.10: Reconstructed particle positions using the TOF times in run 2158 with a beam momentum of 200 MeV/c.

To further see if different particle types have different responses in the detector, and therefore increase the precision of the reconstruction by applying cuts on different

particles, I created a 2D histogram of times of flight between the T0 trigger detector and the TOF detector on the charge in two groups of ACTs. The first ACT group consisted of ACT boxes set to function as the electron veto, and therefore had a low refraction index. The second group had a higher refraction index in order to separate muons and pions. The aerogel index of the run is set to a value, where muons are above the Cherenkov light production and pions are below it. Only muuons will therefore leave a signal above the pedestal in the second ACT group.

I took the time in the T0 as the average time from all the 4 PMTs, and from the TOF detector as the average time from a pair hit. For the first group of ACT detectors this histogram is shown in Figure 5.11. As only electrons leave a signal above the pedestal in this combination of detectors, a cut can be applied on the charge inside the ACTs that electrons are all particles which leave a charge of more than a certain value. This value is different for different beam momentum values. For beam energies of around 200 MeV, I applied a cut that all particles above the total measured charge in the first ACT group $Q_{\mathrm{ACTg1}} > 1000$ units, are electrons. To apply a cut on muons, the second ACT group versus the time of flight has to be compared. This is shown in Figure 5.12, where there is clear separation between the muon and pion signal. To decrease the electron contamination, the histogram can be created after the ACT group 1 cut, resulting in a cleaner muon and pion sample as shown in Figure 5.13.

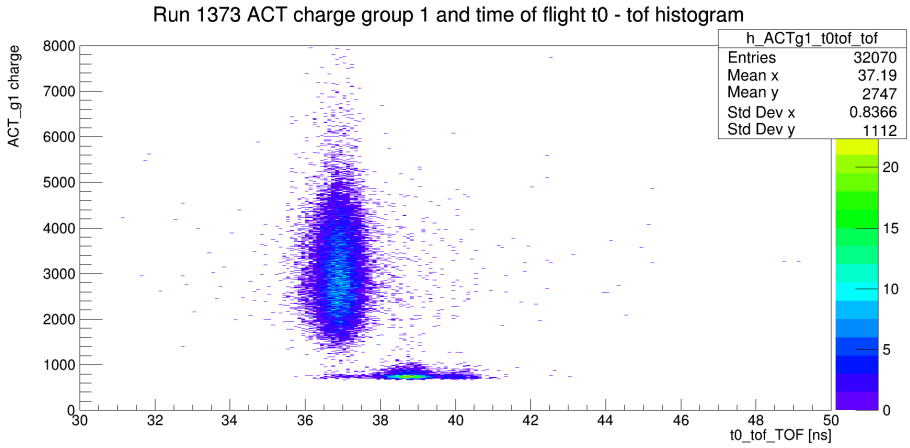


Figure 5.11: A 2D histogram of the charge in ACT group 1 versus the time of flight from T0 to TOF detector in a run with beam momentum of 250 MeV/c. Histogram shows a clear separation of electrons and the rest of the particles.

As shown in Figure 5.13, the pion sample is very small, especially for lower energies, as pions decay in the 50 meter long beam line. For energies lower than 220 MeV/c, no pions were measured in the TOF detector, as they decay before reaching it. To check the different particle responses, I had to look at slightly higher energies with more than 250 MeV/c beam momentum.

Even with these higher energies, the sample was not large enough to apply a Gaussian fit to the opposite SiPM time difference. A large enough sample was found in a run at 550 MeV/c. At this energy, the ACT histograms have a shape shown in Figures 5.14 and 5.15. By zooming on the ACT group two, a cut can be made at charge value $Q_{\mathrm{ACTg2}} > 1050$ to separate muons and pions. When plotting the resulting time difference distributions of the different particles, pions, muons and electrons, each have different σ values of the Gaussian fit. Pions had the lowest values, followed by the

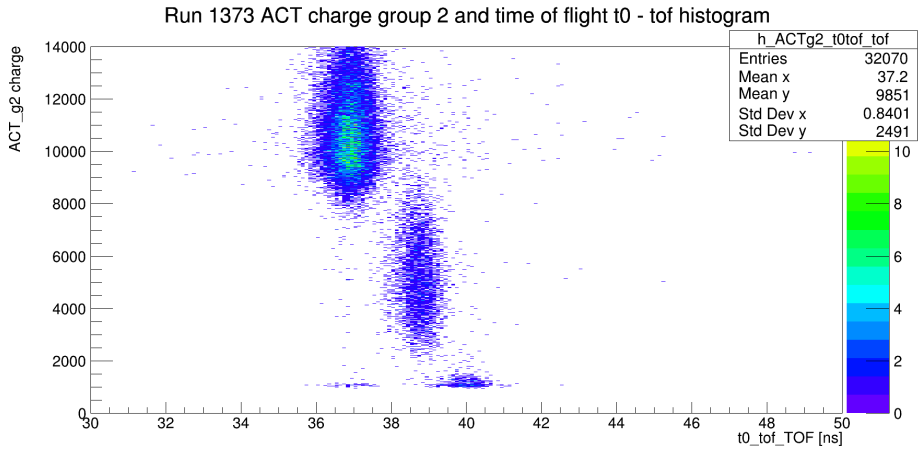


Figure 5.12: A histogram of the charge in ACT group 2 versus the time of flight from the T0 detector to the TOF detector in a run with a beam momentum of 250 MeV/c. Histogram shows a muon and pion separation.

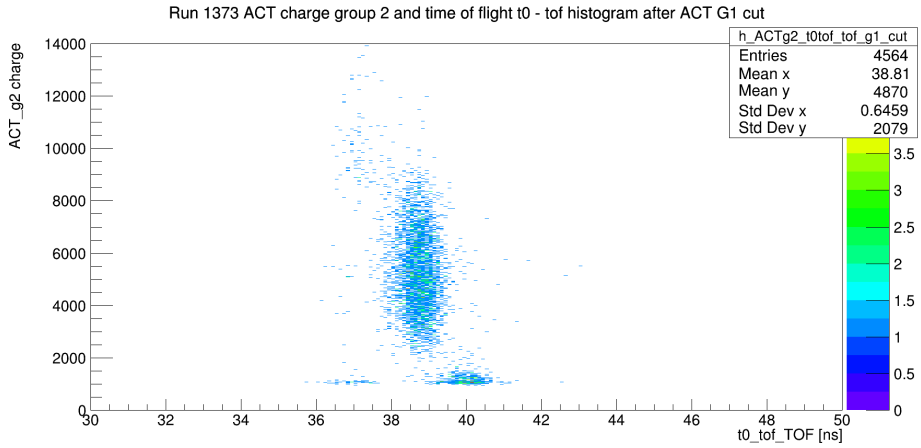


Figure 5.13: Histogram 5.12 with a cut on electrons applied, done for the same run at the beam momentum 250 MeV/c.

muon sample and finally the electrons which had the highest σ value. Comparisons for all scintillators can be seen in Figure 5.16.

A theory was suggested by collaboration members, that a higher signal in the detector can increase the resolution of the detector, so particles with higher ionization losses $|\mathrm{d}E/\mathrm{d}x|_{\text{ionization}}$ like muons and pions might have a better resolution and therefore enable better reconstruction. I plotted a histogram of the time difference in opposite detectors on the total charge measured by the detectors, which resulted in histograms shown in Figures 5.17, 5.18 and 5.19 where it can be seen that pions and muons have different charge deposits which result in higher charges being measured than in electrons. It is still not known what the structures in these histograms are, and the hope is that understanding this will lead to increasing the reconstruction precision.

The position reconstruction using the time data shows promising results so far. The main remaining issue is the relatively high uncertainty of the reconstructed position, largely due to the uncertainty in the model fit to the data. This might be reduced by using particle identification and fitting different particle samples separately. The current results have been presented at collaboration meetings. Through further op-

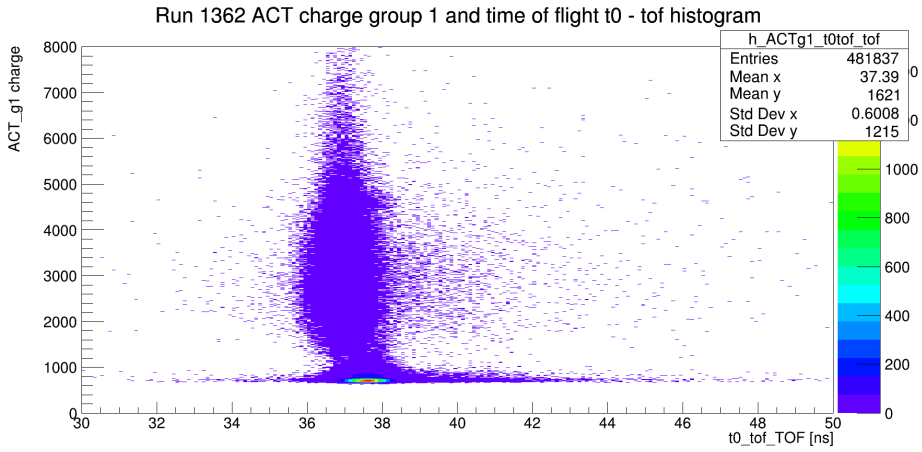


Figure 5.14: A histogram showing the ACT group 1 charge on the time of flight of the particles.

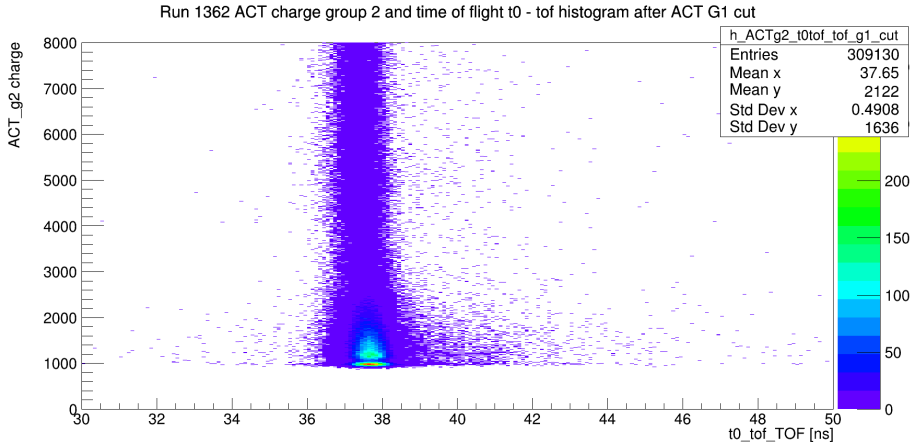


Figure 5.15: A histogram showing the ACT group 2 charge on the time of flight of the particles, after cutting on the ACT group 1 charge.

timization, the resolution may be improved to the extent that the uncertainty of the reconstructed position will not exceed a few centimeters, and consequently allowing the reconstruction to be used as input into calibrating the mPMTs inside the main detector by knowing the interaction vertex in the tank.

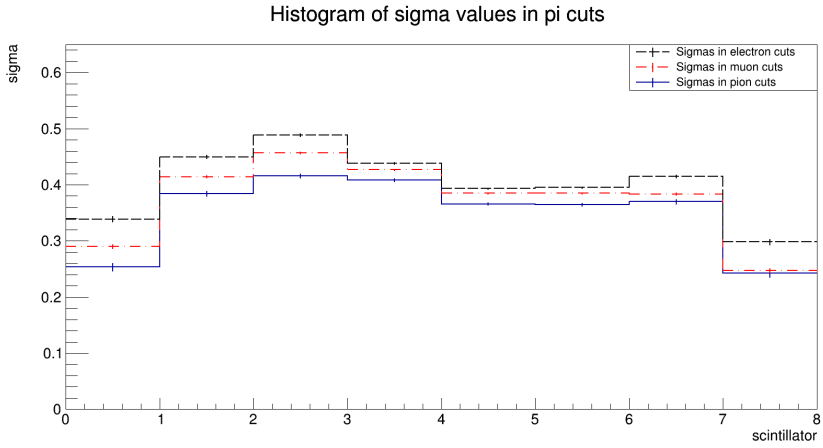


Figure 5.16: Comparison of σ_{meas} values of different scintillator in response to an electron sample, a muon sample and a pion sample in the run with the beam momentum value of 550 MeV/c.

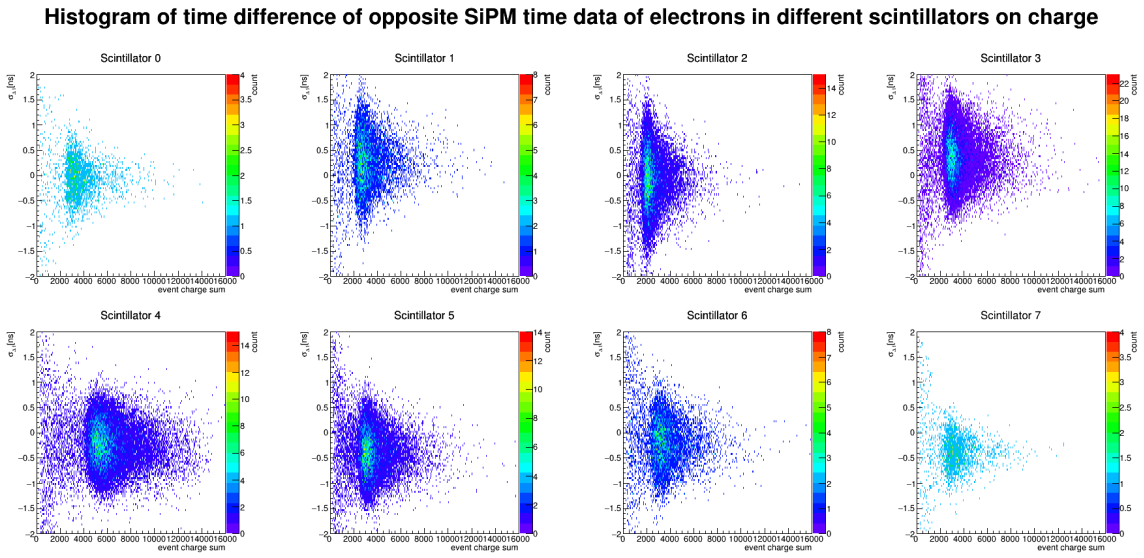


Figure 5.17: A histogram of time difference on opposite SiPMs on the total charge measured for the electron sample.

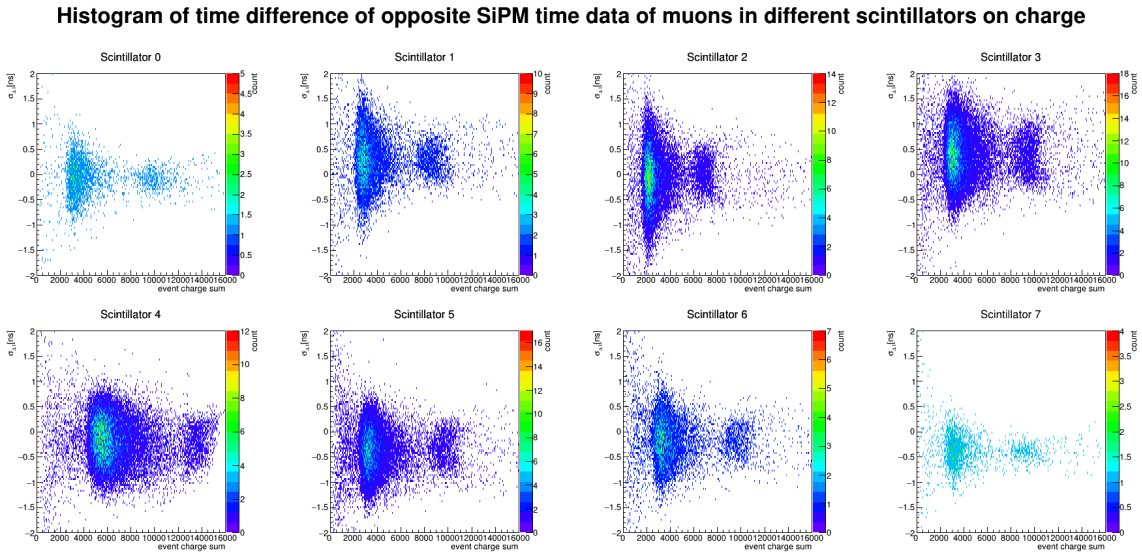


Figure 5.18: A histogram of time difference on opposite SiPMs on the total charge measured for the muon sample.

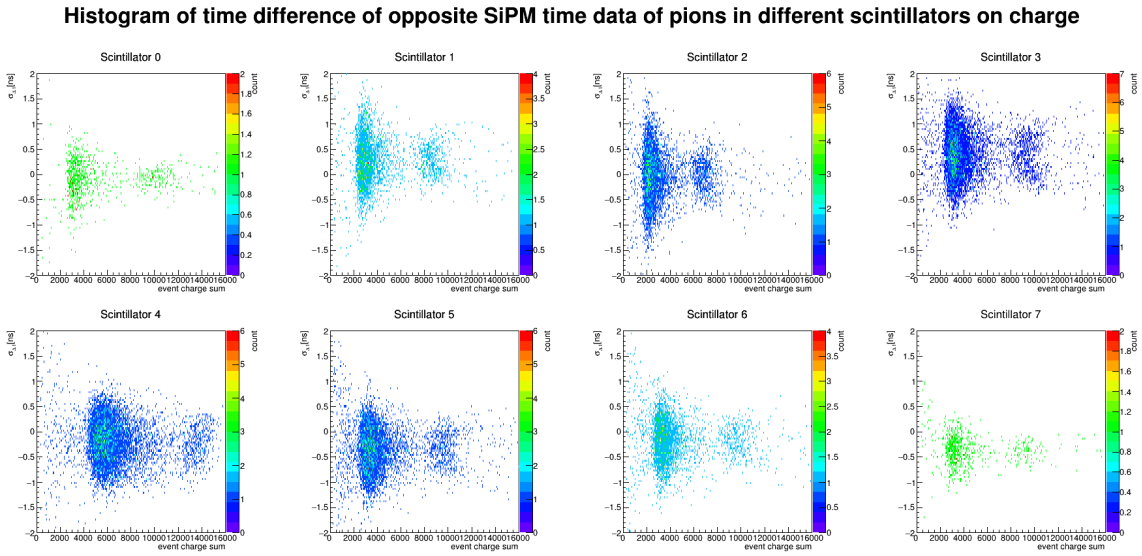


Figure 5.19: A histogram of time difference on opposite SiPMs on the total charge measured for the pion sample.

Conclusion

In this thesis, several practical, computational and analytical contributions to a prototype water Cherenkov detector were described. The detector assembly work in years 2024 and 2025 directly helped to meet the experiment schedule and provided valuable experience concerning detector construction and testing.

A simulation study was done of several different time-of-flight detector prototypes, mainly concerning a model of charge generated by the individual photomultipliers, and the feasibility study of using the measured charges to reconstruct primary particle positions. While one of the detector prototypes ended up not being used, the experience gained through its simulation contributed to meaningful advancement in the particle identification setup modeling. Through applying a model of the charge response to numerical methods, a possible way of increasing detector reconstruction capabilities was obtained. While not directly successful, a few improvements to the used models were theorized that might enable to use them to contribute to particle position measurements.

Other than exploring a toy model of the TOF detector, a survey of cosmic muon models and sea level cosmic muon fluxes was done. Through applying the knowledge of cosmic muon models, a data file necessary for reliably simulating the cosmic muon response in the WCTE detector was created and contributed to the collaboration. This will enable further studies of cosmic rays in surface-level water Cherenkov detectors. In addition to that, an investigation was done on low momentum cosmic muons and muon decays in the simulation, where even though decay events were found, due to their low statistics no deep analysis could be done, and will remain as a further topic of future studies.

Lastly, an analysis of the TOF detector data from the 2025 WCTE run was done, focusing on using the time data from the detector to reconstruct position of particles entering the main detector, which might lead to contributions in calibrating the mPMT modules. Through a series of approximations, a model was created that shows a promise to reconstruct the approximate particle positions. While not complete, further analysis is planned that should increase the precision of the model and enable more credible results.

Together, these contributions support the physics goals of the WCTE experiment, and provide a foundation for further work on the IWCD and Hyper-K experiments.

References

[1] Y. Suzuki, "The Super-Kamiokande experiment", The European Physical Journal C **79**, 1 (2019).

[2] A. Bellerive et al., "The Sudbury Neutrino Observatory", Nuclear Physics B **908**, 30 (2016).

[3] K. Abe et al., "Hyper-Kamiokande design report", arXiv preprint arXiv:1805.04163 (2018).

[4] A. A. Abud et al., "DUNE Phase II: scientific opportunities, detector concepts, technological solutions", Journal of Instrumentation **19**, P12005 (2024).

[5] S. F. King, "Neutrino mass models", Reports on Progress in Physics **67**, 107 (2003).

[6] S. Navas et al. (Particle Data Group), "Review of particle physics", Phys. Rev. D **110**, 030001 (2024).

[7] F. Capozzi et al., "Current unknowns in the three-neutrino framework", Progress in Particle and Nuclear Physics **102**, 48 (2018).

[8] D. J. Griffiths, *Introduction to elementary particles*, Physics textbook (Wiley, New York, NY, 2008).

[9] F. Wilczek, "Origins of mass", Open Physics **10**, 1021 (2012).

[10] P. A. M. Dirac and R. H. Fowler, "A theory of electrons and protons", Proceedings of the Royal Society of London. Series A, Containing Papers of a Mathematical and Physical Character **126**, 360 (1930).

[11] C. D. Anderson, "The Positive Electron", Phys. Rev. **43**, 491 (1933).

[12] S. Carlip, "Quantum gravity: a progress report", Reports on Progress in Physics **64**, 885 (2001).

[13] E. M. Le Boulicaut, "The Standard Model - ATLAS Physics Cheat Sheet", General Photo, 2023.

[14] S. Schael et al. (ALEPH, DELPHI, L3, OPAL, SLD, LEP Electroweak Working Group, SLD Electroweak Group, SLD Heavy Flavour Group), "Precision electroweak measurements on the Z resonance", Phys. Rept. **427**, 257 (2006).

[15] DELPHI collaboration and P. Abreu, "Cross-sections and leptonic forward-backward asymmetries from the Z running of LEP", The European Physical Journal C-Particles and Fields **16**, 371 (2000).

[16] Aleph Collaboration and R. Barate, "Measurement of the Z resonance parameters at LEP", The European Physical Journal C-Particles and Fields **14**, 1 (2000).

[17] L3 Collaboration and M. Acciarri, "Measurements of cross sections and forward-backward asymmetries at the Z resonance and determination of electroweak parameters", The European Physical Journal C-Particles and Fields **16**, 1 (2000).

[18] OPAL collaboration and G. Abbiendi, "Precise determination of the Z resonance parameters at LEP:"Zedometry"", The European Physical Journal C-Particles and Fields **19**, 587 (2001).

[19] S. M. Bilenky, "Neutrinoless double beta-decay", Physics of Particles and Nuclei **41**, 690 (2010).

[20] C. Giganti, S. Lavignac, and M. Zito, "Neutrino oscillations: The rise of the PMNS paradigm", Progress in Particle and Nuclear Physics **98**, 1 (2018).

[21] K. Abe et al., "Constraint on the matter–antimatter symmetry-violating phase in neutrino oscillations", Nature **580**, 339 (2020).

[22] A. Upadhyay and M. Batra, "Phenomenology of Neutrino Mixing in Vacuum and Matter", ISRN high energy physics, `10.1155/2013/206516` (2013).

[23] K. Abe et al., "The T2K experiment", Nuclear Instruments and Methods in Physics Research Section A: Accelerators, Spectrometers, Detectors and Associated Equipment **659**, 106 (2011).

[24] L. Camilleri, "Neutrino detectors", in *Particle physics reference library: volume 2: detectors for particles and radiation*, edited by C. W. Fabjan and H. Schopper (Springer International Publishing, Cham, 2020), pp. 337–382.

[25] A. Oralbaev, M. Skorokhvatov, and O. Titov, "The inverse beta decay: a study of cross section", Journal of Physics: Conference Series **675**, 012003 (2016).

[26] J. A. Formaggio and G. P. Zeller, "From eV to EeV: Neutrino cross sections across energy scales", Reviews of Modern Physics **84**, 1307 (2012).

[27] Y.-F. Li, M. Vagins, and M. Wurm, "Prospects for the Detection of the Diffuse Supernova Neutrino Background with the Experiments SK-Gd and JUNO", Universe **8**, `10.3390/universe8030181` (2022).

[28] D. Casper, "The nuance neutrino physics simulation, and the future", Nuclear Physics B - Proceedings Supplements **112**, 161 (2002).

[29] J. T. Sobczyk et al., "Quasi-elastic Neutrino Scattering—an Overview", in Aip conference proceedings (2011), pp. 59–64.

[30] L. Alvarez-Ruso, Y. Hayato, and J. Nieves, "Progress and open questions in the physics of neutrino cross sections at intermediate energies", New Journal of Physics **16**, 075015 (2014).

[31] U. Mosel, "Neutrino Interactions with Nucleons and Nuclei: Importance for Long-Baseline Experiments", Annual Review of Nuclear and Particle Science **66**, 171 (2016).

[32] E. A. Paschos and D. Schalla, "Coherent pion production by neutrinos", Physical Review D **80**, `10.1103/physrevd.80.033005` (2009).

[33] A. Aguilar-Arevalo et al., "Measurement of the neutrino neutral-current elastic differential cross section on mineral oil at $E_\nu \sim 1$ GeV", Physical Review D—Particles, Fields, Gravitation, and Cosmology **82**, 092005 (2010).

[34] MicroBooNE collaboration et al., *First Measurement of Charged Current Muon Neutrino-Induced K^+ Production on Argon using the MicroBooNE Detector*, 2025.

[35] J. M. Conrad, M. H. Shaevitz, and T. Bolton, "Precision measurements with high-energy neutrino beams", Reviews of Modern Physics **70**, 1341 (1998).

[36] WCTE Collaboration, *Water Cherenkov Test Experiment Status Report (2024)*, tech. rep. (CERN, Geneva, 2024).

[37] WCTE Collaboration, *Water Cherenkov Test Experiment (WCTE) Annual Report, 2024-2025*, tech. rep. (CERN, Geneva, 2025).

[38] D. C. Rodriguez, "Status and Prospects of the Water Cherenkov Test Experiment (WCTE)", PoS **ICHEP2024**, 173 (2024).

[39] K. Yamauchi et al., "Evaluation of event reconstruction with small-scale water Cherenkov detectors", Journal of Physics: Conference Series **2156**, 012199 (2021).

[40] M. Gola et al., "Assembly, testing, and installation of mPMT photosensor for the Water Cherenkov Test Experiment", arXiv preprint arXiv:2504.07216 (2025).

[41] J. Kisiel, "Photodetection and electronic system for the Hyper-Kamiokande Water Cherenkov detectors", Nuclear Instruments and Methods in Physics Research Section A: Accelerators, Spectrometers, Detectors and Associated Equipment **1055**, 168482 (2023).

[42] N. Prouse, P. de Perio, and W. Fedorko, "Machine Learning Techniques to Enhance Event Reconstruction in Water Cherenkov Detectors", Physical Sciences Forum **8**, `10.3390/psf2023008063` (2023).

[43] T. Mondal et al., "Likelihood and Deep Learning Analysis of the electron neutrino event sample at Intermediate Water Cherenkov Detector (IWCD) of the Hyper-Kamiokande experiment", in Proceedings of 42nd international conference on high energy physics — pos(ichep2024), ICHEP2024 (Dec. 2024), p. 232.

[44] WCTE Collaboration, *Water Cherenkov Test Experiment Status Report (2022)*, tech. rep. (CERN, Geneva, 2022).

[45] M. Tabata, "Transparent silica aerogel blocks for high-energy physics research", in *Springer handbook of aerogels* (Springer International Publishing, 2023), pp. 1333–1352.

[46] X. Li, *WCTE experience*, Presentation at the Hyper-Kamiokande Internal Meeting, Internal collaboration presentation, Internal document, not publicly available, 2025.

[47] J. Nieves et al., "2p2h excitations, MEC, nucleon correlations and other sources of QE-like events", in Proceedings of the 10th international workshop on neutrino-nucleus interactions in few-gev region (nuint15) (2016), p. 010002.

[48] C. Jollet and A. Meregaglia, "9Li and 8He decays in GEANT4", Nuclear Instruments and Methods in Physics Research Section A: Accelerators, Spectrometers, Detectors and Associated Equipment **949**, 162904 (2020).

[49] F. Hrubý, *Toy model simulation for primary particle position reconstruction using detector charges and analysis code for data measured by WCTE*, code repository, (2025) `https://github.com/hrubyfr/WCTE_rootstuff/tree/main/BeamMonitor`.

[50] R. Brun, F. Rademakers, P. Canal, et al., *ROOT [software]*, version v6.28/10, Nov. 2023.

[51] R. Brun and F. Rademakers, "ROOT — An object oriented data analysis framework", Nuclear Instruments and Methods in Physics Research Section A: Accelerators, Spectrometers, Detectors and Associated Equipment **389**, New Computing Techniques in Physics Research V, 81 (1997).

[52] Eljen Technology, *EJ-228, EJ230 Fast Timing Plastic Scintillator*, (Aug. 2023) `https://eljentechnology.com/products/plastic-scintillators/ej-228-ej-230` (visited on 08/05/2025).

[53] R. L. Workman et al. (Particle Data Group), "Review of Particle Physics", PTEP **2022**, 083C01 (2022).

[54] T. Dealtry et al., *WCSim: Water Cherenkov Detector Simulation*, version v1.12.21, (2025) `https://github.com/WCSim/WCSim` (visited on 05/08/2025).

[55] S. Agostinelli, J. Allison, K. Amako, et al., "Geant4—a simulation toolkit", Nuclear Instruments and Methods in Physics Research Section A: Accelerators, Spectrometers, Detectors and Associated Equipment **506**, 250 (2003).

[56] A. Buckley et al., "The HepMC3 event record library for Monte Carlo event generators", Computer Physics Communications **260**, 107310 (2021).

[57] S. Cecchini and M. Spurio, "Atmospheric muons: experimental aspects", Geoscientific Instrumentation, Methods and Data Systems **1**, 185 (2012).

[58] N. Su et al., "A Comparison of Muon Flux Models at Sea Level for Muon Imaging and Low Background Experiments", Frontiers in Energy Research **Volume 9 - 2021**, `10.3389/fenrg.2021.750159` (2021).

[59] J. Bae and S. Chatzidakis, "A new semi-empirical model for cosmic ray muon flux estimation", Progress of Theoretical and Experimental Physics **2022**, 043F01 (2022).

[60] T. K. Gaisser, R. Engel, and E. Resconi, *Cosmic Rays and Particle Physics*, 2nd ed. (Cambridge University Press, 2016).

[61] A. Tang et al., "Muon simulations for Super-Kamiokande, KamLAND, and CHOOZ", Phys. Rev. D **74**, 053007 (2006).

[62] E. V. Bugaev et al., "Atmospheric muon flux at sea level, underground, and underwater", Physical Review D **58**, `10.1103/physrevd.58.054001` (1998).

[63] D. Reyna, *A Simple Parameterization of the Cosmic-Ray Muon Momentum Spectra at the Surface as a Function of Zenith Angle*, 2006.

[64] S. Chatzidakis, S. Chrysikopoulou, and L. Tsoukalas, "Developing a cosmic ray muon sampling capability for muon tomography and monitoring applications", Nuclear Instruments and Methods in Physics Research Section A: Accelerators, Spectrometers, Detectors and Associated Equipment **804**, 33 (2015).

[65] F. Hrubý, *Analysis code for the WCSim simulation of cosmic muons*, code repository, (2025) `https://github.com/hrubyfr/WCTE_Cosmic`.

[66] F. James, M. Winkler, et al., "Minuit user's guide", CERN, Geneva **23**, 408 (2004).

[67] J. Ocariz, *Probability and Statistics for Particle Physicists*, 2014.